Terms and Conditions of Use of Digitised Theses from Trinity College Library Dublin

Copyright statement

All material supplied by Trinity College Library is protected by copyright (under the Copyright and Related Rights Act, 2000 as amended) and other relevant Intellectual Property Rights. By accessing and using a Digitised Thesis from Trinity College Library you acknowledge that all Intellectual Property Rights in any Works supplied are the sole and exclusive property of the copyright and/or other IPR holder. Specific copyright holders may not be explicitly identified. Use of materials from other sources within a thesis should not be construed as a claim over them.

A non-exclusive, non-transferable licence is hereby granted to those using or reproducing, in whole or in part, the material for valid purposes, providing the copyright owners are acknowledged using the normal conventions. Where specific permission to use material is required, this is identified and such permission must be sought from the copyright holder or agency cited.

Liability statement

By using a Digitised Thesis, I accept that Trinity College Dublin bears no legal responsibility for the accuracy, legality or comprehensiveness of materials contained within the thesis, and that Trinity College Dublin accepts no liability for indirect, consequential, or incidental, damages or losses arising from use of the thesis for whatever reason. Information located in a thesis may be subject to specific use constraints, details of which may not be explicitly described. It is the responsibility of potential and actual users to be aware of such constraints and to abide by them. By making use of material from a digitised thesis, you accept these copyright and disclaimer provisions. Where it is brought to the attention of Trinity College Library that there may be a breach of copyright or other restraint, it is the policy to withdraw or take down access to a thesis while the issue is being resolved.

Access Agreement

By using a Digitised Thesis from Trinity College Library you are bound by the following Terms & Conditions. Please read them carefully.

I have read and I understand the following statement: All material supplied via a Digitised Thesis from Trinity College Library is protected by copyright and other intellectual property rights, and duplication or sale of all or part of any of a thesis is not permitted, except that material may be duplicated by you for your research use or for educational purposes in electronic or print form providing the copyright owners are acknowledged using the normal conventions. You must obtain permission for any other use. Electronic or print copies may not be offered, whether for sale or otherwise to anyone. This copy has been supplied on the understanding that it is copyright material and that no quotation from the thesis may be published without proper acknowledgement.

A Microscopic and Spectroscopic Characterisation of Nanotube/Conjugated Polymer Interactions
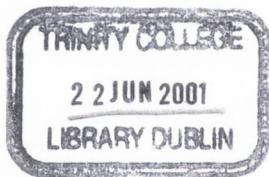
By

Brendan Mc Carthy

A thesis submitted for the degree of
Doctor of Philosophy
in the
University of Dublin

Department of Physics
Trinity College Dublin

November 2000

Declaration

I declare that the work in this thesis has not been previously submitted as an exercise for a degree to this or any other university.

The work described herein is entirely my own, except for the assistance mentioned in the acknowledgements and the collaborative work mentioned in the list of publications.

I agree that Trinity College Library may lend or copy this thesis on request.

Brendan Mc Carthy
November 2000

Acknowledgements

Firstly, I would like to thank my supervisor for the past 3 years, Professor Blau, for all the support, scientific, moral and financial, over the course of this thesis. I have the opportunity to visit many facilities and attend many conferences, for which I am grateful.

I would also like to thank all the other people, who have helped during this thesis. These are (in order of decreasing hair length, lest there be accusations of bias); Johnny, Aldot, Hugh of DIT, and Marc. Thanks to Donna, for papers, proofreading and everything else. Thanks to David John, old Neil, new Neil, and Colin of the EMU. Also the Clemson people, Dave, Rich and Daniel, thanks for everything. I'll send the key tomorrow, I promise... Thanks to the chemists, Steffi and Anna. All the other people in the group, nanotube related and not; in random and possibly incomplete order, as Bernd names them, take it up with him if you're omitted; Margaret, Bernd, Brian, Adam, Colin, Stephen, Jean, Caitriona, Sean, Martin, Patrick, Sandy, Rob, Take, Valerie, Michael, Manuel, Diarmuid, Marie. Thanks to the technicians, Tom, John, James and Mick, for all technical and bureaucratic assistance. Thanks to Dave for printing services, and all the other lads, and everybody else I've ever known or been introduced to. That should cover it, I think. And Finally, thanks to my parents and family for everything.

Table of Contents

Table of Figures

Abstract

A composite material of a conjugated polymer and carbon nanotubes has been developed. The conjugated polymer is poly(p-phenylenevinylene-co-2,5-dioctyloxy-m-phenylenevinylene) (PmPV), a polymer significant for its applications in organic electronics. A range of nanotubes are used, both multi-walled and single-walled. Multi-walled nanotubes are produced in TCD by the arc discharge method, and by catalytic decomposition of acetylene in Namur, Belgium.

This composite is interesting, as there is sufficient interaction between the polymer and nanotubes to keep the nanotubes in solution, a feature that has not been observed in composites developed elsewhere. To gain a greater understanding of this binding mechanism, these composites are characterised by a range of microscopies and spectroscopies. Microscopic characterisation is carried out by Transmission Electron Microscopy (TEM), and Scanning Tunneling Microscopy (STM). Spectroscopic characterisation is by optical techniques, absorption and fluorescence spectroscopy, and by Raman spectroscopy.

Transmission Electron Microscopy shows that there is a strong binding between the PmPV and nanotubes. Nucleation of dendritic growths of PmPV is observed from defect sites on the nanotube lattice. The PmPV is observed to coat the nanotubes in both an ordered form, and an unordered form. Examination of SWNT composites suggests that the ordering is due to a mapping of the PmPV onto the lattice of the nanotube.

Spectroscopic characterisation is employed to examine the effects this has on the PmPV. Introduction of SWNT into these materials is observed to significantly affect the spectroscopy. Consistent with the TEM and STM observations, the PmPV is observed to exhibit greater electron localisation, and dramatically reduced interchain effects.

Scanning Tunneling Microscopy is used to examine pure PmPV, and PmPV-SWNT composites. The pure PmPV is observed to form ordered films on a graphite substrate. It is also seen, as with TEM, to form an ordered coating on the SWNT. This is due to mapping onto the lattice structure of the SWNT.

Chapter 1

Introduction

1.1 Scientific Background

Over the past few decades, the field of electronics, encompassing a vast range of applications from LEDs to supercomputers, has made amazing progress, gradually affecting all areas of our lives. This progress has all been based on advances in the field of inorganic electronics, predominantly silicon-based, but also recently developed materials such as Gallium Arsenide. Organic materials, and polymers especially, have been relegated to passive applications, such as food packaging, window frames and computer cases, all fields where the lack of chemical and electronic activity are advantageous. This is the common perception of polymers, or plastics, where their advantages of low cost, resilience and inertness has lead them to become ubiquitous in everyday life.

Over recent years, however, this perception has been revised within the scientific community, with the field of organic electronics expanding rapidly. In certain

applications, organic devices are beginning to replace inorganic devices, and they are expected to supersede them in many areas as advances continue to be made. One of the first breakthroughs in the field of organic electronics came in 1974, with the development of the first semiconducting polymer, polyacetylene[1]. This gave the first indications that organic systems could rival established inorganic systems for electronic applications. As with inorganic semiconductors, metallic levels of conductivity could be achieved by doping. For polyacetylene, this requires oxidation with a chemical such as iodine[2]. The electronic activity of these systems is due to the conjugated sp^2-hybridised backbone, giving rise to an overlapping and delocalised system of π-electrons. As with inorganic semiconductors, these delocalised electrons exist in a band structure along the polymer backbone, with fully occupied and fully unoccupied bands.

These initial advances, whilst demonstrating the potential of organic systems, still had many severe obstacles hindering any potential applications. They were highly unstable, and difficult to process. Since this discovery much research has been directed towards overcoming these obstacles with much success. The motivations for this research are the potential advantages of polymer-based electronics; cheap processing, small thickness, large area applications and flexibility[3].

In the last decade, this field has exploded, with many developments encroaching on the domain once only occupied by inorganic semiconductors. In 1990, the first organic LED was developed[4]. Since then, many other polymeric devices have been developed, such as photodiodes[5], photovoltaic cells[6], field effect transistors[7] and optically pumped lasers[8]. Recently, commercial products based on polymeric LED devices have begun to be marketed by such companies as Phillips, Uniax Corporation,

13

and Cambridge Display Technologies. The importance of these developments were acknowledged in October 2000 by the awarding of the Nobel Prize in Chemistry to the pioneers in this field, A.J. Heeger, A.G. Mac Diarmuid and H. Shirakawa.

Another pioneering breakthrough in the field of organic materials came in 1986, with the discovery by H.E. Kroto, R.F. Curl, and R.E. Smalley of a third allotrope of carbon, the C_{60} molecule, or Buckminster Fullerene[9]. For this discovery, they were awarded the Nobel Prize in Chemistry in 1996. Before this discovery, it had been thought that ordered carbon only existed in the form of diamond or graphite. Subsequently, further discoveries found that C_{60} was one of a family of carbon molecules. Further interest in Fullerene science was generated by the discovery by S. Iijima of long cylindrical forms of fullerenes called carbon nanotubes. The initially discovered forms consisted of multiple concentric cylinders, Multi-Walled Carbon Nanotubes[10] (MWNT), later discoveries also proved the existence of Single-Walled Carbon Nanotubes[11] (SWNT). Nanotubes essentially consist of graphite sheets scrolled into cylindrical form. Defects in the lattice structure cause closure at the tips.

Shortly after their discovery, theoretical investigations of nanotubes predicted unique properties, and became the subject of much interest and research. Nanotubes were predicted to be semiconducting or metallic, depending on the chiral vector, which quantifies how the graphene sheet is scrolled[12]. This has been confirmed experimentally[13, 14]. They have also been shown to be stronger than steel[15]. Many applications have been proposed to take advantage of these singular properties[16]. These include quantum wires[17], tips for scanning probe microscopy[18], and molecular diodes[19].

However, despite the high expectations and progress in these fields of carbon nanotubes, and conjugated polymers, there are several problems hindering their development. Conjugated polymers do have problems with stability and strength, and consequently commercial products have to incorporate extensive protection in their packaging to shield them from damage and the environment. In addition, their conductivity is low due to low intrinsic carrier density and mobility. Pure carbon nanotubes are not available in large quantities, and inevitably come with large amounts of impurities. Furthermore, there is no way to control the distribution of nanotubes within a sample, which come in a wide range of chiralities and sizes. In addition, technological limitations mean that manipulating these is difficult, and impossible on a repeatable large scale. These limitations imply that any applications in the near future will only be able to harness the bulk properties of carbon nanotubes. These include as bulk reinforcement for materials[20], and as mechanical actuators[21].

Research in Trinity has focussed on a possible means of overcoming these limitations. It has been proposed that by binding these two materials, conjugated polymers, and carbon nanotubes into a composite material, several of these problems can be overcome, and the resultant composite properties are a complement of the two components[22]. The incorporation of nanotubes into a conjugated polymer matrix greatly enhances the electronic transport properties. Furthermore, it should also increase the mechanical strength of these materials and, by increasing the thermal conductivity, improve the stability of these materials. The problems of nanotube purity and processing are addressed due to a selective interaction between the conjugated polymer and the nanotube, allowing the nanotubes to be selectively filtered from an impure nanotube sample.

In this thesis, these composites will be characterised by a variety of microscopies and spectroscopies. This will lead to a greater understanding of the composites, and the binding process between the two components.

1.2 Thesis Outline

The two types of materials studied in this thesis are carbon nanotubes and conjugated polymers. In Chapter 2, the properties of these materials will be reviewed. This will include discussion of the structural and electronic properties of both types of material.

Chapter 3 discusses the experimental methods employed in this thesis. This divides into two main sections. The first, materials synthesis, describes the methods of production for the materials used in this study. This covers the synthesis of the conjugated polymer poly(p-phenylenevinylene-co-2,5-dioctyloxy-m-phenylene vinylene), PmPV. Following from this, the several methods used to produce nanotubes for this work will be reviewed. Then, the techniques for composite preparation are described. The second section reviews the various methods used to prepare samples for examination by microscopy and spectroscopy.

Chapter 4 reviews previous work of significance to this study. This includes investigations of PmPV performed within Trinity and elsewhere of relevance to this study. Previous examinations of the composite are reviewed, to explain the potential of these composites. Work currently in progress to develop applications is summarised.

Chapter 5 encompasses a detailed characterisation by transmission electron microscopy of composites based on both multi-walled and single-walled carbon nanotubes.

Chapter 6 examines these composites based on SWNT materials by a range of optical and vibrational spectroscopies.

Chapter 7 presents an examination of the pure PmPV, and SWNT-based composites by scanning tunneling microscopy.

Finally, Chapter 8 concludes this thesis, by reviewing the research presented here. The implications of this research are also addressed and areas for future work are considered.

References

[1] H. Shirakawa, T. Ito, S. Ikeda, *Polym. J.*, **4**, 460 (1973).

[2] C.K. Chiang, C.Z. Fincher, Y.W. Park, A.J. Heeger, E. Shirakawa, E.J. Lown, S.C. Gau, A.G. Mac Diarmuid, *Phys. Rev. Lett.*, **39C**, 1098 (1977).

[3] A. J. Epstein and Y. Yang (Eds.) *MRS Bull.*, **22**, 6 (1997).

[4] J.H. Burroughs, D.D.C. Bradley, A.R. Brown, R.N. Marks, K. Mackey, R.H. Friend, P.L. Burns, A.B. Holmes, *Nature*, **347**, 539 (1990).

[5] J.J.M. Halls, C.A. Walsh, N.C. Greenham, E.A. Marseglia, R.H. Friend, S.C. Moratti, A.B. Holmes, *Nature*, **376**, 498 (1995).

[6] J.J.M. Halls, D.R. Baigent, F. Cacialli, N.C. Greenham, R.H. Friend, S.C. Moratti, A.B. Holmes, *Thin Solid Films*, **276**, 13 (1996).

[7] J.H. Burroughs, C.H. Jones, R.H. Friend, *Nature*, **335**, 137 (1988).

[8] N. Tessler, G.J. Denton, R.H. Friend, *Nature*, **382**, 695 (1996).

[9] H.E. Kroto, J.R. Heath, S.C. O'Brien, R.F. Curl, R.E. Smalley, *Nature*, **318**, 162 (1985).

[10] S. Iijima, *Nature*, **354**, 56 (1991).

[11] S. Iijima, T. Ichihashi, *Nature*, **363**, 603 (1993).

[12] J.W. Mintmire, C.T. White, *Carbon*, **33,** 893 (1995).

[13] J.W.G. Wildoer, L.C. Venema, A.G. Rinzler, R.E. Smalley, C. Dekker, *Nature*, **391**, 59 (1998).

[14] T.W.Odom, J.L. Huang, P.Kim, C.M. Lieber, *Nature*, **391**, 62 (1998).

[15] M.M.J. Treacy, T.W. Ebbesen, J.M. Gibson, *Nature*, **381**, 678 (1996).

[16] M.Dresselhaus, G. Dresslhaus, R. Saito, *Physics World*, **9**, 18 (1996).

[17] S.J. Tans, M.H. Devoret, H.Dai, A.Thess, R.E. Smalley, L.J. Geerligs, C. Dekker, *Nature*, **386**, 474 (1997).

[18] H.Dai, J.H. Hafner, A.G. Rinzler, D.T. Colbert, R.E. Smalley, *Nature*, **384**, 147 (1996).

[19] S.J. Sander, J. Tans, A.R.M. Verschueren, C. Dekker, *Nature*, **393**, 49 (1998).

[20] P. M. Ajayan, L. S. Schadler, C. Giannaris, A. Rubio, *Adv. Mater.,* **12**, 750 (2000).

[21] R.H. Baughman, C.X. Cui, A.A. Zakhidov, Z. Iqbal, J.N. Barisci, G.M. Spinks, G.G. Wallace, A. Mazzoldi, D. De Rossi, A.G. Rinzler, O. Jaschinski, S. Roth, M. Kertesz, *Science*, **284**, 1340 (1999).

[22] S. Curran, P. M. Ajayan, W. Blau, D. L. Carroll, J. N. Coleman, A.B. Dalton, A.P. Davey, A. Drury, B. McCarthy, S. Maier, A. Strevens, *Adv. Mat.*, **10,** 1091 (1998).

Chapter 2

Materials and Experimental Background

2.1 Theory of Organic Materials

The term organic material is used to refer to all materials whose chemistry is determined by their carbon atoms. They encompass a vast range of materials, from methane to polymers, nanotubes, and most biological materials. The materials used in this work consist of a range of carbon nanotubes, and a specifically chosen conjugated polymer, PmPV. Here in this chapter the basic concepts of organic systems will be explained, and this will in turn be used to understand the physics of conjugated polymers and carbon nanotubes. Additionally, the basic physics behind the experimental techniques used in this work will be outlined.

2.1.1 Basic Concepts of Organic Materials

Carbon is unique in that it can form many different bond arrangements, both in carbon-carbon bonds, and in bonding to other materials. For example, simple hydrocarbons of two carbons can form several different arrangements, e.g. ethane

(C_2H_6), or ethylene (C_2H_4). The reason for this is due to the difference in the carbon-carbon bonds in these materials.

The electron configuration of a single carbon atom is $1s^2 2s^2 2p^2$. Hence, there are four valence electrons available for bonding. In carbon for the case of ethane, the 2s and 2p electron orbitals mix, creating four equivalent degenerate orbitals, arranged around the nucleus. These orbitals are sp^3 hybrid orbitals. Three of these combine with the 1s electron of the hydrogen atoms to form a filled orbital, a C-H bond. The fourth one combines with an sp^3 orbital from the other carbon atom to form a final filled orbital, a C-C bond. All the electrons in this molecule are then tightly bound in σ bonds. Due to the high bonding energy of these bonds, it takes a large amount of energy to excite these electrons, and these bonds are therefore relatively inert. Because of this, excitation of these bonds tends to be accompanied by chemical reaction of the molecule. This sp^3 bonding is the type of bonding that carbon forms in most common polymers used in industrial applications, e.g. PVC, as well as diamond, and explains the highly insulating and inert nature of these materials.

Ethylene (C_2H_4) has a much different bond structure, which is essential to understanding the nature of conjugated polymers and nanotubes. In ethylene, two s and one p electrons combine to form three sp^2 hybrid orbitals. These are arranged in a plane around the nucleus, separated by 120°. Two of these bond with hydrogen atoms, one with another carbon atom, leaving one electron on each atom in the unhybridised p_z orbital. The p_z orbitals are arranged in a dumbbell shape out of plane. The electrons in these orbitals overlap to form a final filled bonding molecular orbital, a π bond. These bonds are weaker and much more delocalised, and therefore require much less energy to excite them. In addition, excitations of these electrons leave the

molecular structure relatively unperturbed. The bonding structure of ethylene is depicted in Figure 2.1[1].
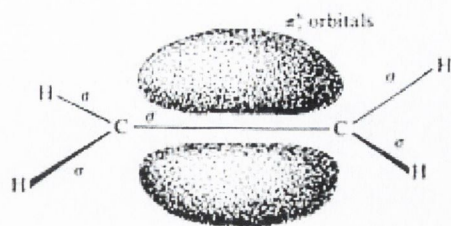
Figure 2.1 Bonding Structure of Ethylene.

What are important about these π bonds are the delocalisation, and their relatively low energy. As will be discussed in more detail when conjugated polymers are dealt with, for longer molecules, these electrons can delocalise over a significant part of a polymer, giving rise to an electronic band. This results in a semiconducting band structure for long sp^2 hybridised polymers.

2.1.2 Electronic Structure of Polymers

Non-Conjugated Polymers

Non-conjugated polymers are chains of carbon atoms connected by σ bonds, e.g. polyethylene. This differs from the example used previously of ethylene, as here each carbon atom bonds to the two adjacent carbon atoms, and two hydrogen atoms. Hence, each carbon atom shares one electron with each of four other atoms, and the electron orbitals are sp^3 hybridised. The electrons are tightly bound and highly localised between each carbon atom, and it requires a large amount of energy to excite them. This implies that these materials have a large bandgap, and can be considered electronically inactive insulators. This bonding structure is depicted in Figure 2.2.

Saturated polymer - polyethylene

$$+\begin{matrix} H & H \\ | & | \\ C-C \\ | & | \\ H & H \end{matrix}+_x$$

CB

VB

sigma bond with
localized electrons

insulator
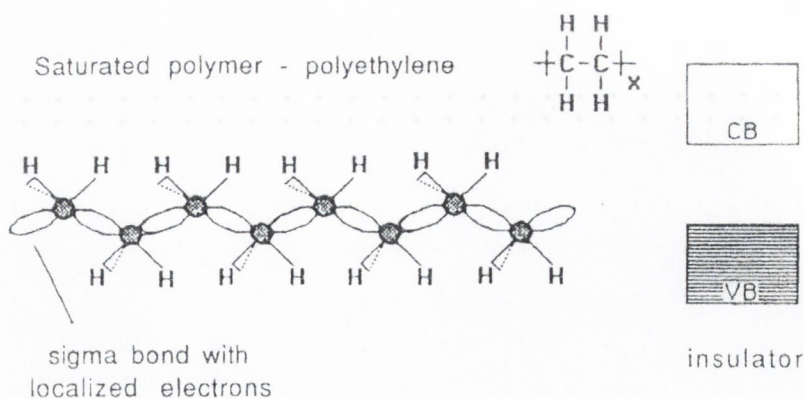
Figure 2.2 Band structure of a non-conjugated polymer, polyethylene.

Conjugated Polymers

Conjugated polymers are long chains of carbon atoms, held together by σ bonds. As with ethylene, this results in π bonds lying out of plane and parallel to this σ-bonded backbone of carbon atoms. These π-electrons tend to delocalise over a number of repeat units of the polymer. Depicted in Figure 2.3 is this delocalisation illustrated for poly(p-phenylenevinylene), PPV. The polymer used in these studies, PmPV, is a variant of this, having alternating *para* and *meta* linkages on each benzene ring. It can be seen how the p_x orbitals described previously overlap to form a delocalised electron cloud over the length of the polymer. These electrons are highly mobile and loosely bound to a particular atom, and are therefore free to move over the conjugation length of the polymer.

As each bond consists of two overlapping orbitals, which can each accommodate two electrons, it follows that each bond can accommodate four electrons, two in each energy level, of opposite spins.
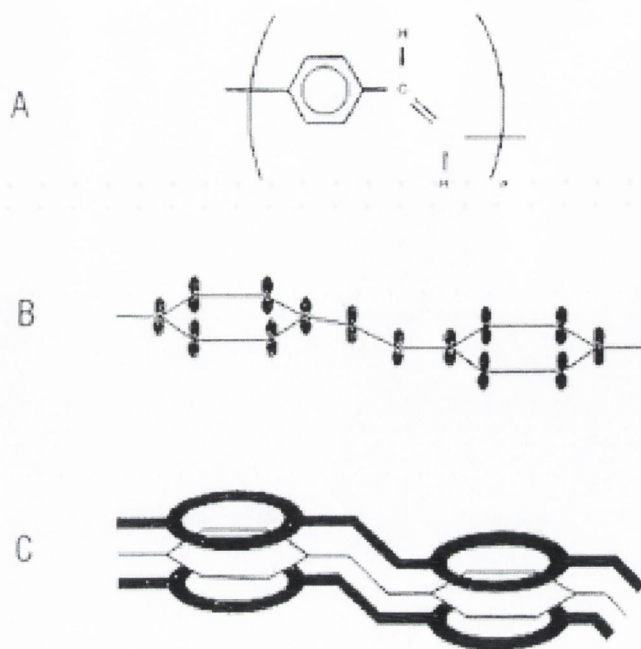
Figure 2.3 Schematic of delocalised π bonds in poly(p-phenylene-vinylene).
A) Chemical structure of PPV; B) The p_x orbitals of the carbon bonds lying
perpendicular to the plane of PPV; C) The π bonds formed by p_x orbitals overlap
to form a delocalised electron cloud over the polymer chain parallel to the plane
of PmPV

Each contains only two, as explained previously, and is therefore only half-filled. For polymers, with overlapping π bonds, the result is a half-filled band. This is similar to a metallic electron structure, where energy levels alter to form a tightly spaced band, due to the Pauli Exclusion Principle.

Figure 2.4 demonstrates this for the simplest conjugated polymer, polyacetylene, where, as each unit cell has only one electron, the result is a half-filled band, i.e. a one-dimensional metal. This is the ideal case, and following from this it was expected that the only obstacle to making a metallic polymer was synthesising a long enough polymer with enough π electrons to form a band system.

Unsaturated conjugated polymer - polyacetylene

$$\begin{array}{c} H \\ | \\ +C=C+ \\ | \\ H \end{array}_x$$
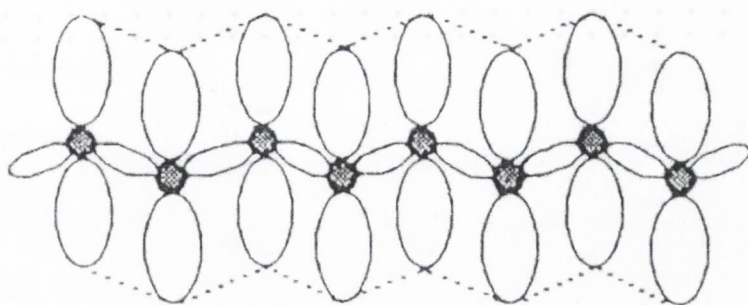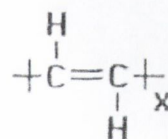
continuous
Π–system with delocalized
electrons

half-filled
band

Figure 2.4 Continuous π system, resulting in a half-filled band, illustrated for polyacetylene.

Polyacetylene was first synthesised by Natta *et al* in 1956[2]. This was found to be semiconducting, but this was initially ascribed to the poor quality of the polymer. In 1974 Ito and Shirakawa synthesised high quality free standing films of polyacetylene[3], but characterisation showed that these were still intrinsically semiconducting, with a bandgap of 1.4eV[4]. As with inorganic semiconductors, these could be 'doped' by exposing them to oxidizing agents such as iodine, increasing their conductivity by up to eleven orders of magnitude to metallic levels[5].

The understanding as stated above could not account for the intrinsically semiconducting nature of polyacetylene, and obviously there was a flaw in the theory.

The theory assumes that the electron wavefunctions are fully delocalised, and all carbon atoms are equally spaced. This is not the case, as the double bonds are slightly shorter than the single bonds, by approximately 0.04Å, as measured by X-ray

diffraction[6]. It had indeed been proposed by Peierls in 1955[7] that a one-dimensional metal as polyacetylene would be unstable, as there is an alternative configuration of lower energy with this alternation of bond length. In addition, the electron delocalisation in polymers has been shown to be over a maximum of 15-20 repeat units[8], so there is not the continuous half-filled band as expected. The reason for the bond alternation is that the increase in lattice energy due to this distortion is less than the decrease in electronic energy. For polyacetylene, this introduces a bandgap of approximately 1.5eV, where all occupied energy levels are shifted down by 0.7eV, and all unoccupied levels increase in energy by 0.7eV.

bond alternation limits the extent
of delocalization

large gap
semiconductor
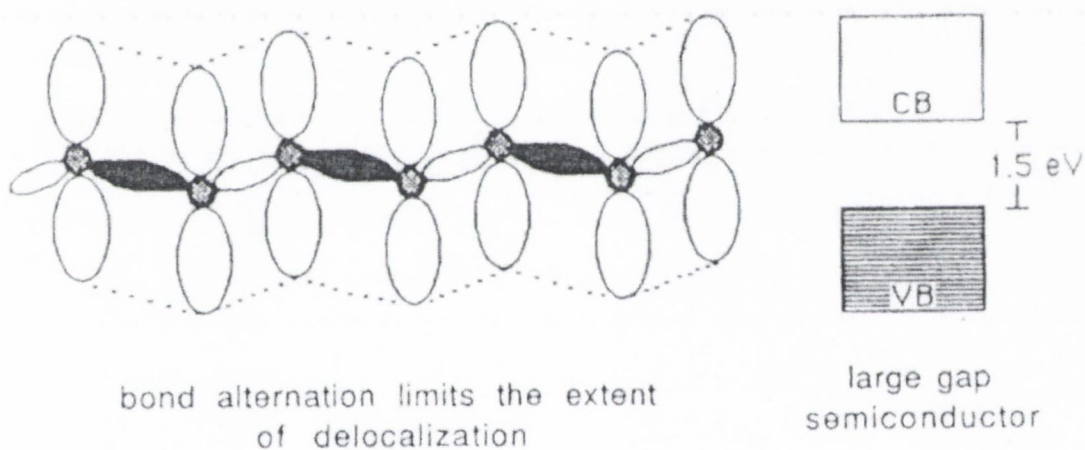
Figure 2.5 Peierl's Transition introduces bond alternation and a resultant splitting of the electronic band structure.

Bond alternation opens up an energy gap in the dispersion curve at $k=\pi/2a$ where a is the unit cell length before dimerisation as shown in Figure 2.6. The extra elastic energy is compensated by the reduction in energy of occupied states around $k=\pi/2a$.
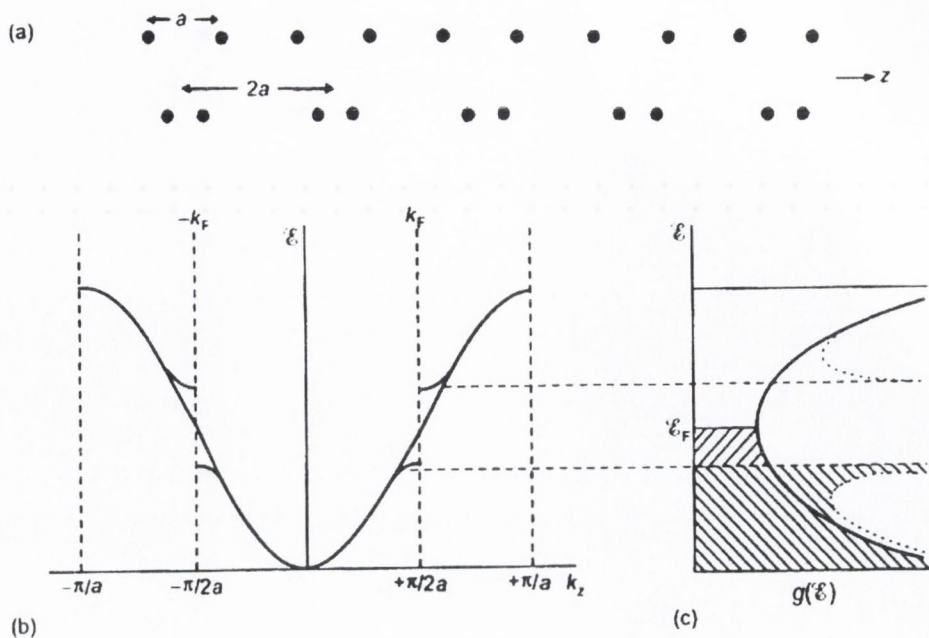
Figure 2.6 Effect of Peierl's distortion in polyacetylene on the dispersion curve.
(a) Illustration of bond length alternation.
(b) the effect on the band structure.

It is more energetically favourable for alternate single and double bonds to form compared to a band of fully delocalised π electrons (Figure 2.6 a). Without Peierl's distortion, the extended band structure is parabola like with a half filled conduction band. In the presence of the distortion, dimerisation causes dislocations in the band structure (Figure 2.6 b) at the Brillouin zone edge, opening up a bandgap (Figure 2.6 c).

Examining Figure 2.5, it can be seen that, as in inorganic semiconductors, the band structure divides into two; a fully occupied band, and a fully unoccupied band. These are analogous to the valence band and the conduction band in inorganic semiconductors, respectively. This band structure is usually described using the terms Highest Occupied Molecular Orbital (HOMO) for valence band and Lowest Unoccupied Molecular Orbital (LUMO) for conduction band. This terminology is used to describe optical and electronic transitions in polymers.

27

Photophysics of Conjugated Polymers

In an organic system, the ground and excited states have many vibrational and rotational degrees of freedom. When Born-Oppenheimer separability conditions are assumed valid, the total wavefunction of the molecule may be written as the product of separated wavefunctions and the energy can be written as:

$$E_t = E_e + E_v + E_r \qquad\qquad\qquad Equation\ 2.1$$

The subscripts e, v and r refer to electronic, vibrational and rotational components respectively[1]. The act of absorption of a photon involves the interaction of the electric field of the light with the static and dynamical components of the molecule. The absorption and emission of an organic molecule are represented in Figure 2.7. In this figure, the energies of the ground state and the excited states are shown as a function of the configuration coordinate of the system, which represents the positions of the atomic nuclei. Since electronic transitions take place on a much faster time scale than nuclear motion (less than 10^{-15}s compared to approximately 10^{-13} s), most electronic transitions are completed before the nuclei can alter their spatial relationships. Such a transition is denoted by a vertical line in Figure 2.7 and is known as a Franck-Condon transition. The Franck-Condon principle states that an electronic transition occurs so rapidly in comparison with the vibration frequencies, that no change occurs in inter-nuclear separation during the course of a transition. After excitation of the molecule to an upper vibronic state, the nuclear coordinates are not in their equilibrium configuration for the new electronic state and hence radiationless relaxation between the vibrational states occurs. Experimentally this occurs very quickly, on time scales of approximately 10^{-13} s. Generally, after relaxing to the lowest vibrational v' = 0 state, the electron can return to the ground state by

emitting its excess energy as a photon or by other radiationless channels of decay[9].
The emitted photon is characteristically of longer wavelength than that of the exciting
light. This is known as the Stoke's shift. The absorption and emission spectra also
demonstrate symmetry.
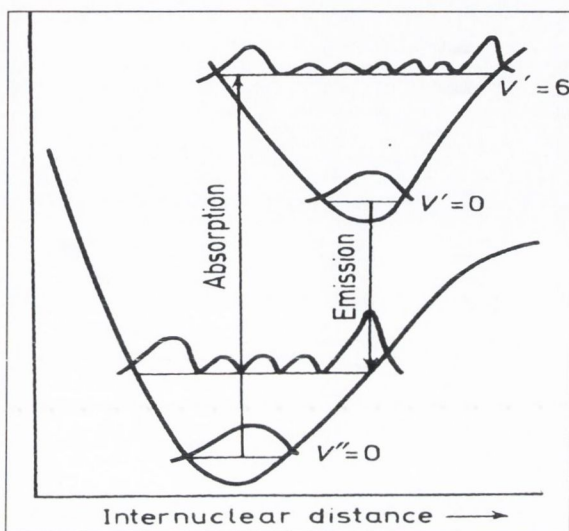
*Figure 2.7: Electronic transitions of greatest probability for absorption emission
from vibrational levels.*

Figure 2.8 shows an alternative diagram for a complex molecule such as naphthalene.
The diagram is a modification of a form devised by Jablonski, and called a Jablonski
diagram[10]. It does not attempt to represent the molecular shapes and sizes and the
vibrational levels for each state do not usually correspond to the actual v", v'
numberings and spacing. On the other hand, the energies of the vibrational ground
states of each electronic level are shown correctly if the experimental evidence is
available. Wavy lines on the diagram represent radiationless energy conversion: the
vertical wavy lines within a particular electronic state indicate degradation of
vibrational excitation (probably by an intermolecular process), while the horizontal
wavy lines indicate intramolecular energy exchange. Formal distinction is drawn
between electronic energy exchange permitted by the $\Delta S = 0$ rule and that forbidden
by it. The term internal conversion is applied to radiationless transitions between

states of the same spin multiplicity, while intersystem crossing refers to energy exchange between states belonging to different 'spin' systems.
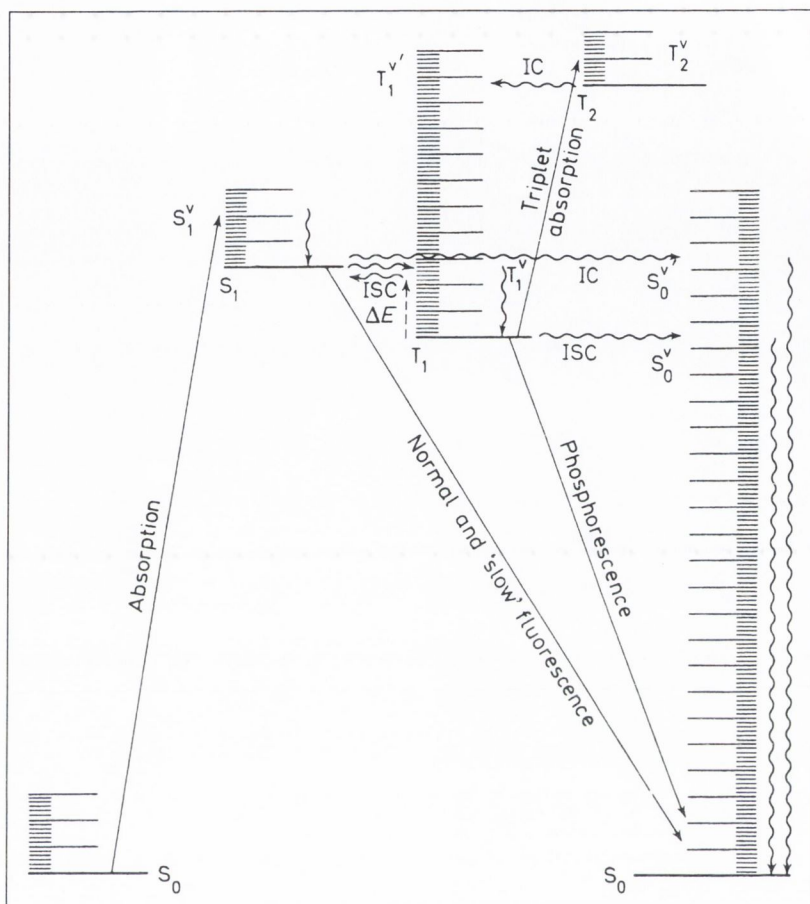
Figure 2.8: Jablonski diagram showing absorption and emission processes.

Deactivation through emission of radiation can happen in two ways. These two emission processes were originally distinguished in terms of whether or not there was an observable afterglow. In 1935, Jablonski interpreted phosphorescence as being emission from some long-lived metastable electronic state lying lower in energy than the state populated by absorption of radiation. This was in fact a triplet state of the species.

The long lifetime of the emission is a direct consequence of the 'forbidden' nature of a transition from an excited triplet to the ground state singlet. Hence, phosphorescence can be described as a radiative transition between states of different

multiplicity. Fluorescence is then understood to be a radiative transition between states of the same multiplicity.

Theoretical Modelling of Conjugated Polymers

In the late seventies, Su, Schreiffer and Heeger (SSH) proposed a tight-binding model method to model polyacetylene[11]. This involved calculations on a chain with cyclic boundary conditions, which neglected electron-electron interactions. The polymer chain is represented as a series of carbon atoms bound by σ bonds in the plane. These bonds were represented by an effective spring constant, K, between neighbouring atoms. Electron-phonon interactions are considered by introducing a nearest neighbour overlap integral into the system's Hamiltonian. This can be expanded linearly about the equilibrium separation of neighbouring atom, $t = t_0 + \alpha(u_n - u_{n+1})$, where u_n is the displacement of site n, and the σ electrons are parameterised through the force constant for the bonds, K. The model can be expressed by the SSH Hamiltonian shown:

$$H = -\sum_n [t_0 + \alpha(u_n - u_{n+1})](c_n^+ c_{n+1} + c_{n+1}^+ c_n)$$

$$+ \frac{1}{2M} \sum_n p_n^2 + \frac{K}{2} \sum_n (u_n - u_{n+1})^2.$$

Equation 2.2

where the c_n notation refers to the ladder operators of quantum mechanics. The first term gives the kinetic energy of the π electrons, the second term gives the kinetic energy of the lattice (p_n is the momentum of the atom at site n), and the third term gives the π bond strain energy. For polyacetylene, the predicted dimerisation effect on the induced band gap is much smaller than experimental evidence indicates. It is

31

probable that the enhanced bond dimerisation is due to the effects of the on-site Coulomb repulsion energy[12]. In the case of non-degenerate polymers, the introduction of aromatic or heteroaromatic units causes the $\pi-\pi*$ gap to be much larger than for polyacetylene[13].

For these polymers, it is more practical to begin with the molecular orbitals of the monomer, and calculate the electronic structure by introducing nearest neighbour interactions between monomer units. This broadens the conduction and valence bands, and reduces the gap between the highest occupied state and the lowest unoccupied state. This inter-molecular interaction broadens the bands and hence lower the energy gap.

The SSH model has been adapted extensively to accommodate discrepancies between the original predictions and the experimental results[14, 15]. There are still a number of flaws that must be addressed. In particular, the simple model predicts that the energy of photons emitted should be equal to the spacing between the two bipolaron levels. Experimentally it is found to occur at significantly higher energy than the bipolaron spacing as determined by photo-induced absorption. Some conjugated polymers, such as trans-polyacetylene exhibit no luminescence implying solely non-radiative decay. It has been suggested that this is due to the lowest energy excited state having the wrong parity to couple radiatively to the ground state, contrary to predictions of the SSH model.

2.1.3 Structure of Carbon Nanotubes

Before the discovery of fullerenes in 1985[16], ordered carbon was thought to exist in only two allotropes; diamond, an sp^3 hybridised form of carbon, and graphite, an sp^2 hybridised form. In 1985 however, Kroto, Curl, and Smalley discovered the first

member of a new family of carbon structures, in the form of a spherical cage. This was C_{60}, consisting of a mainly hexagonal lattice, with the incorporation of five pentagons giving sufficient positive curvature for it to close into a sphere.

diamond

C_{60}
"buckminsterfullerene"

graphite

(10,10) tube
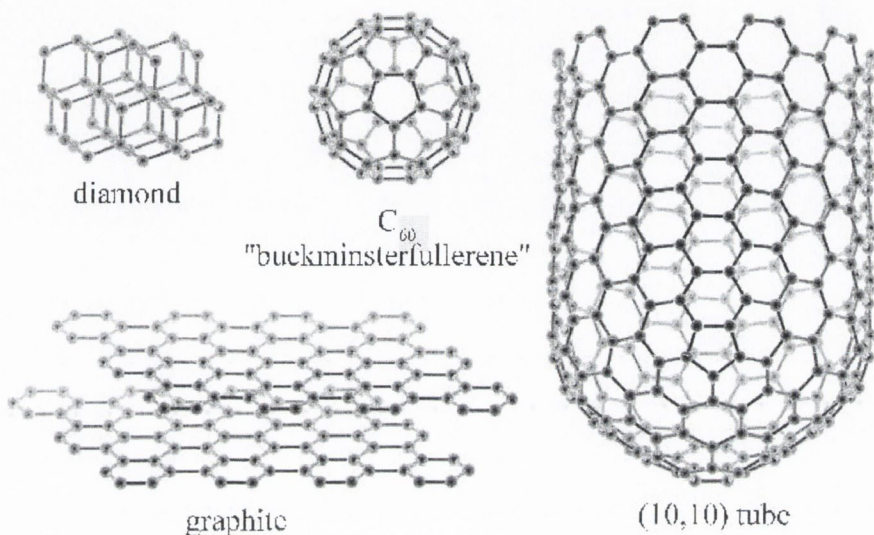
Figure 2.9 Allotropes of carbon; diamond, graphite, fullerenes and nanotubes.

This was named Buckminster Fullerene, in honour of the architect who had used this structure in many buildings. Following this discovery, many other members of the fullerenes family were discovered, differing in radii and in shapes. The most important discovery, and the one for which expectations has been highest, is the discovery of carbon nanotubes by Iijima of the NEC Research Laboratory in Japan in 1991[17]. These are predicted to have unique mechanical and electronic properties due to their high symmetry, their one-dimensional structure, and their exceptionally high aspect ratio.

Physical Structure of Carbon Nanotubes

A geometrically perfect carbon nanotube consists of two-dimensional hexagonal lattices of carbon atoms scrolled to form concentric cylinders. Those that consist of

one graphene cylinder are known as single walled nanotubes (SWNT), and those with more than one wall, multiwalled nanotubes (MWNT). All cylinders are capped at both ends by endcaps where, as in the case of C_{60}, pentagons are introduced to give curvature and close the cylinders. As is usually found experimentally, imperfect nanotubes can have defects along the tube body in the form of pentagons, heptagons, sp^3 hybridised carbon in the graphene lattice, causing kinks and bends in the structure. In addition, endcaps are not usually spherical. In multiwalled nanotubes, a constant spacing of 0.34 nm separates the walls, which is very close to the basal plane spacing in graphite (0.335 nm)[18]. MWNT have diameters of the order of 10s of nanometres, and lengths of the order of 100s of nanometres. SWNT have diameters of the order of nanometres.

There are many ways in which the graphene sheet can be scrolled to form a cylinder, depending on the angle that the lattice makes with the cylinder axis. This is characterised by the chiral vector which is defined by $\underline{C}$ = n$\underline{a}_1$+m$\underline{a}_2$ where $\underline{a}_1$ and $\underline{a}_2$ are unit vectors in the hexagonal lattice and m and n are integers. These are depicted in Figure 2.10. The (n, m) values of the chiral vector determines all the characteristics of an ideal nanotube, including diameter, chiral angle, and all electronic properties, notably the bandgap of the nanotube. The chiral angle is the angle between the lattice and the cylindrical axis of the nanotube. It can be derived by the following equation[19]:

$$\theta = Tan^{-1} (\sqrt{3}n/(2m+n)) \qquad\qquad Equation\ 2.3$$

where θ is the chiral angle of the nanotube. The diameter is given by the following equation[19]:

$$d = (\sqrt{3}/\pi)a_{C\text{-}C}(m^2+mn+n^2)^{1/2} \hspace{3cm} \textit{Equation 2.4}$$

where d is the nanotube diameter in nanometers, and $a_{C\text{-}C}$ is the carbon-carbon bonding distance measured in nanometres, 0.142nm. The bandgap, or, for the case of metallic nanotubes, the gap between the first van Hove singularities, is dependent on the diameter, and hence on the (n, m) values of a nanotube and is given by

$$E_{gap} = 2a_{C\text{-}C}\gamma_0/d \hspace{3cm} \textit{Equation 2.5}$$

where γ_0 is the C-C tight binding overlap energy, experimentally determined to be 2.7±0.1 eV for nanotubes[19].
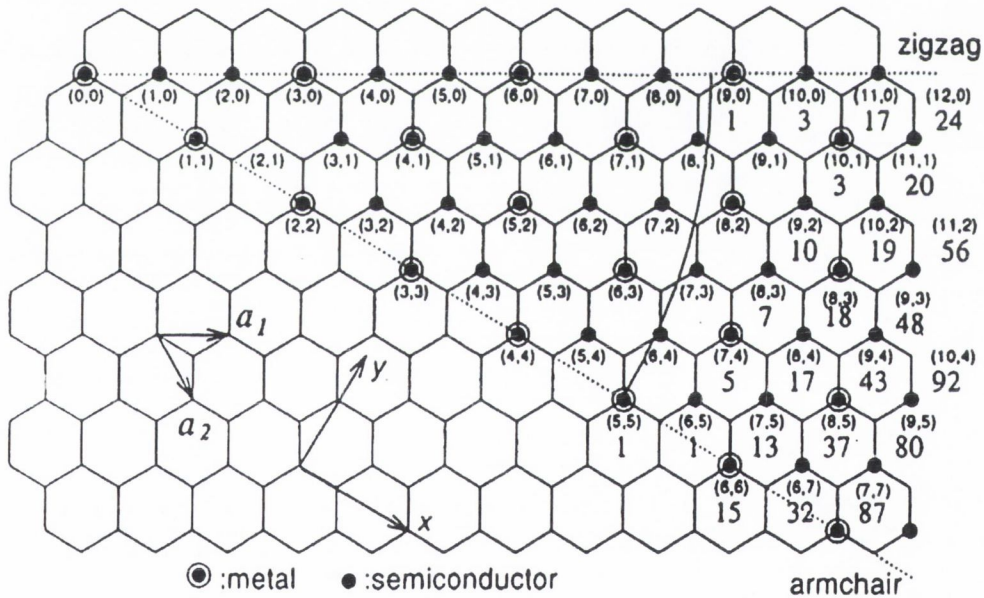
Figure 2.10 Representation of the possible chiral vectors of carbon nanotubes.

Figure 2.10 gives a diagram relating possible chiral vectors to the corresponding lattice symmetry. Nanotube chiralities can be divided into three broad categories. Zigzag nanotubes have chiral vectors of the form (n, 0), and therefore the rows of the lattice structure are perpendicular to the nanotube axis. Armchair nanotubes have

chiral vectors (n, n), and have bonds lying perpendicular to the nanotube axis. All other nanotubes have chiral angle between 0° and 30° and are called chiral nanotubes. These three general types of nanotubes are depicted in Figure 2.11.
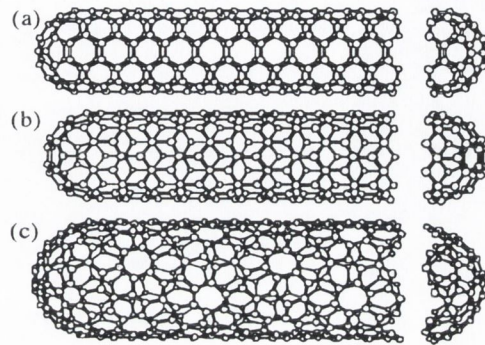
Figure 2.11 The three general types of nanotubes; (a) armchair, (b) zigzag, (c) chiral.

Electronic Structure of Carbon Nanotubes

Carbon nanotubes, as described above, are composed of an sp^2-hybridised graphite sheet scrolled to form a cylinder. The ideal infinite graphene sheet is a semiconductor with a bandgap of 0eV, and hence is usually observed to have metallic conduction properties. The unique feature of carbon nanotubes, and the reason why so much attention has been generated, is due to the quasi-one-dimensional nature of nanotubes. In the radial direction, electrons are confined by the monolayer thickness of the graphene sheet. Electrons can only propagate along the nanotube, and all possible wave-vectors are parallel to the nanotube axis. This leads to the quantum confinement of electrons normal to the tube axis. Furthermore, due to the rotational symmetry of nanotubes, there are additional periodic boundary conditions around the tube circumference. The density of states (DOS) of the nanotube is restricted to states that have this periodicity, and the possible standing waves that are allowed around the circumference of the nanotube. The boundary condition of periodicity is known as

the Born-von Karman boundary condition, and electronic states have to satisfy this condition.

$$\underline{k}.\underline{C} = 2\pi q \qquad\qquad Equation\ 2.6$$

where q is an integer. Applying this to model the electronic structure, it can be seen that nanotubes differ dramatically depending on the circumference of the nanotube, and hence on the (n, m) values of the chiral vector. Depending on the length of periodicity, allowed states can exist at the Fermi energy, and therefore the nanotube will be metallic, or a bandgap can exist at the Fermi level, and the nanotube will be semiconducting.
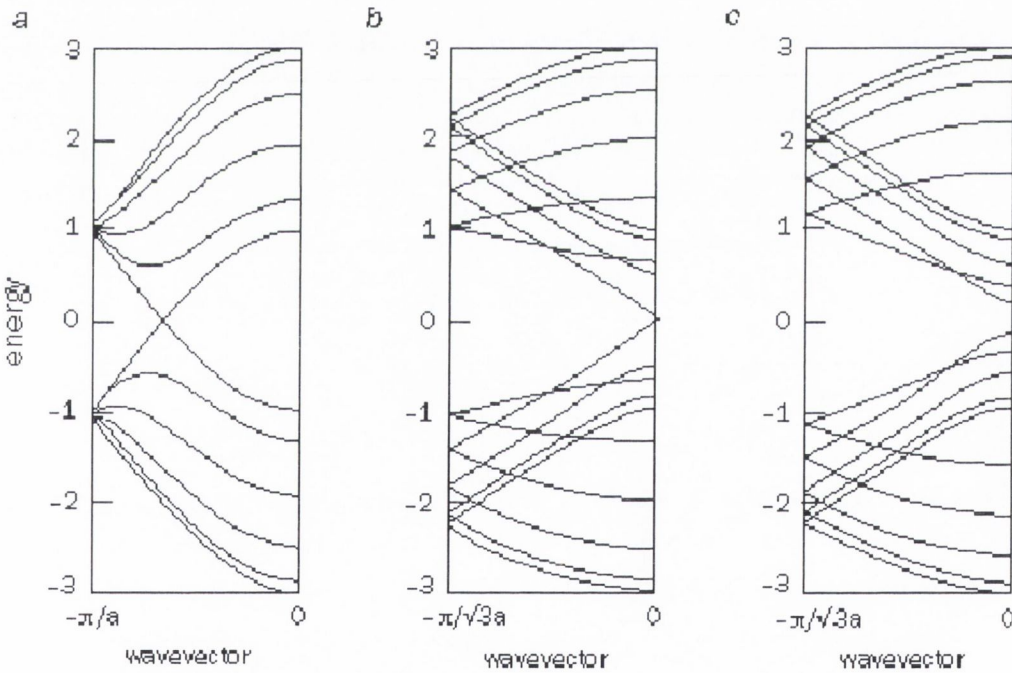
Figure 2.12 Band structure calculations for single walled nanotubes[19].
The left hand graph is due to a truly metallic tube as there is a finite density of states at the Fermi energy. The middle tube is a semiconducting tube with zero bandgap. The right hand tube is semiconducting.

Shown in Figure 2.12 are dispersion relations calculated for the three broad categories of electronic structure into which all nanotubes fall[19]. On the left is a metallic

nanotube, with states existing at the Fermi level. In the middle is a pseudo-metallic nanotube, which is, similar to graphite, a semiconductor with a zero bandgap. This will be metallic at all temperatures above absolute zero, as thermal energy will ensure there is a large amount of occupied states in the conduction band. On the right is a semiconducting nanotube, with a finite bandgap.

The relationship that determines from the chiral vector which nanotubes will be metallic is relatively simple[19], and is

$$\frac{n-m}{3} = p \qquad\qquad\qquad\qquad Equation\ 2.7$$

Thus, if p is zero, the nanotube is metallic, if p is an integer, it is pseudo-metallic, else it is semiconducting. Immediately apparent from this is that 1/3 of all nanotubes are metallic, and that all armchair nanotubes are metallic, as these are nanotubes where n=m.
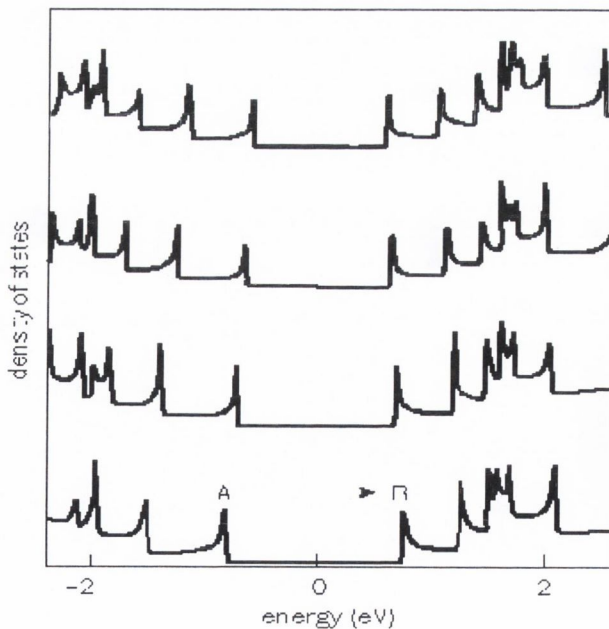
Figure 2.13 The van Hove singularities are apparent as sharp spikes in the DOS[19]. The A-B is the first electronic transition between van Hove singularities, corresponding to the bandgap in semiconducting nanotubes.

As stated previously, $E_{gap} = 2a_{C-C}\gamma_0/d$ determines the bandgap as inversely proportional to the diameter of the nanotube. This can be understood as the curvature of the lattice induces a strain in the graphene sheet, manifesting itself in the bandgap. As the curvature decreases with increasing diameter, the bandgap will reduce. As the diameter goes to infinity, the bandgap goes to zero, and the result is a flat semiconducting graphene sheet with zero bandgap, i.e. graphite.
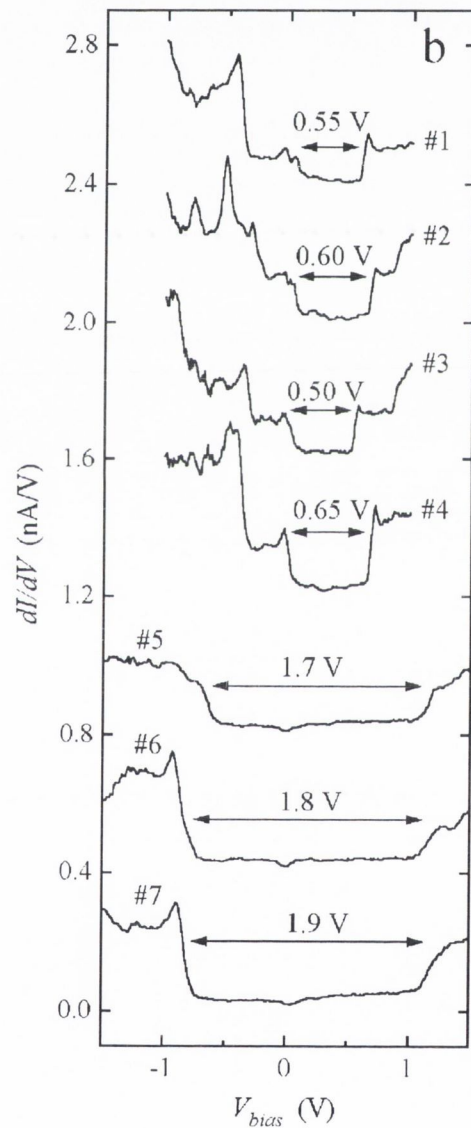
Figure 2.14 Experimentally measured density of states of several different nanotubes[20].

One further notable feature of the electronic structure of nanotubes is the presence of singularities in the density of states, due to the one dimensional nature of nanotubes. These are known as van Hove singularities, and are due to the confinement of the electron wavevectors to directions parallel to the nanotube axis. Calculated DOS of various nanotubes are shown in Figure 2.13, where the singularities are apparent as sharp spikes arranged symmetrically about the Fermi level[19].

Experimentally measured DOS measured by scanning tunneling spectroscopy[20] are shown in Figure 2.14, for comparison with Figure 2.13. The van Hove singularities are apparent as broadened peaks arranged about the bandgap. Due to several factors, such as instrument limitations, and thermal effects, they are not as well resolved or symmetric as theoretical predictions.

Electronic Structure of Multi-Walled Nanotubes

The above explanation of the electronic structure of SWNT is simplified as it refers only to an idealised single nanotube shell. This consists of a perfect hexagonal lattice scrolled into a cylinder. In reality, unfortunately, the situation is much more complicated. Nanotubes are rarely free from defects, such as pentagons, heptagons or sp^3 hybridised carbon in the lattice, leading to kinks, bends and charge localisation in the nanotube[21]. Furthermore, multiwalled carbon nanotubes consists of many close concentric cylinders, and interactions between these can greatly complicate the electronic structure. The original work on shell interactions modelled double-walled nanotubes, and suggested that interlayer coupling had little effect on the electronic structure of the individual shells[22]. Thus, individual shells were predicted to retain their semiconducting or metallic nature. This suggested also the possibility of nanoscale insulated conductors, when a metallic tube is inside a high-bandgap

semiconducting nanotube. Further work by J.C. Charlier *et al*[23], suggests that this might be more complicated. By modelling a (5,5) nanotube inside a (10,10) nanotube, both of which are metallic, they found that for certain orientations of one nanotube with respect to the other, interlayer interactions could cause both to become semiconducting. For other combinations of double-walled nanotubes that were modelled, relative orientations of nanotubes had no effect on the electronic structure. The density of states for a MWNT is far more complicated than for SWNTs, however the outer shell is thought to dominate the electronic structure, as it is the shell that interacts with the external environment.

2.2 Experimental Theory

2.2.1 Scanning Tunneling Microscopy and Spectroscopy

Introduction

Scanning Tunneling Microscopy (STM) has made a dramatic impact on such diverse areas as materials science, semiconductor physics, biology and organic chemistry since its invention in 1982[24]. The basic principle of STM is that, by scanning a metal tip with sufficient precision and proximity to the surface of a sample, and by applying a potential difference between the sample and tip, an image of the surface can be obtained. Atomic resolution image can be obtained, depending on the microscope used, and the nature of the tip and sample. When the voltage is applied, electrons quantum-mechanically tunnel between tip and sample, and this current will have a dependence on the topography and local electronic structure of the sample. The basic principle behind STM, electron tunneling[25], was discovered in 1928 by Fowler and Nordheim, shortly after the development of the theory of quantum mechanics. STM has proven itself unique amongst microscopic techniques, in that it can provide

41

simultaneous information about topographic and electronic structure with atomic resolution.

Basic Concepts of Scanning Tunneling Microscopy

The basic configuration of an STM is a conducting tip and sample separated by a non-conducting medium, usually a vacuum. Essentially this vacuum is a potential barrier between two conducting mediums. This is shown schematically in Figure 2.15.
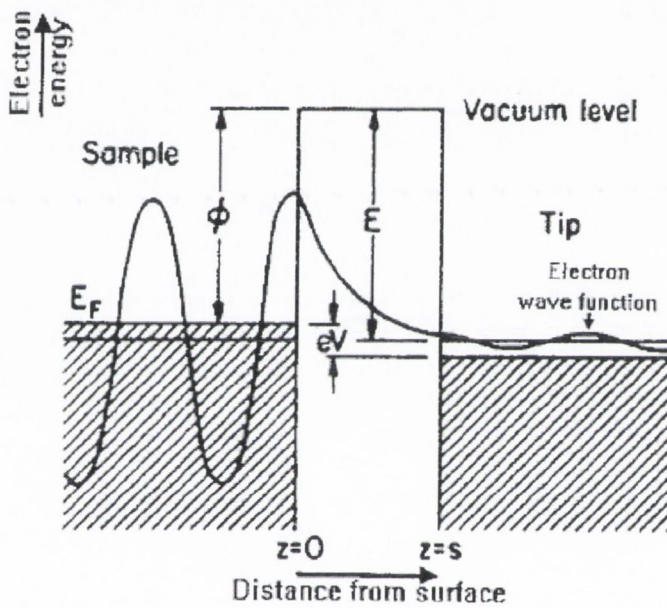
Figure 2.15 Diagram of the wavefunctions of the sample-vacuum-tip configuration[26].

When the tip-sample distance is close enough that the wavefunctions can overlap, there is a small probability that electrons can quantum mechanically tunnel through the potential barrier. This probability depends on the applied voltage, the tip-sample separation, and this tunneling current is given as[26]

$$I = C\rho_t \rho_s e^{s\phi^{1/2}}$$

Equation 2.8

where s is the tip-sample distance, ρ_s and ρ_t are the electron density of the sample and tip respectively, and ϕ is a parameter relating to the potential barrier. From this it can

be seen that the tunneling current is highly sensitive to the tip-sample separation, and a change in separation of 1Å, will result in an order of magnitude change in the tunneling current. It is also dependent on the local electronic structure of the sample, and this dependence can be used to deduce the sample's electronic structure, as will be seen later in the discussion on scanning tunneling spectroscopy.

Design and Operation of an Scanning Tunneling Microscope
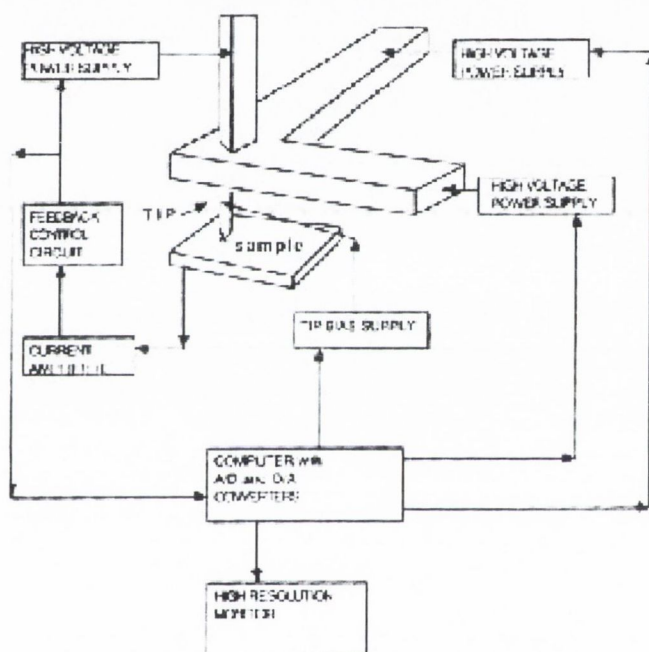
Figure 2.16 Schematic of a Scanning Tunneling Microscope.
Piezo elements Px and Py scan the metal tip over the sample surface. The control unit (CU) modulates the voltage (V_P) applied to the Pz piezo to maintain a constant tunnel current (I_t) at bias voltage V_t. The tip displacement at a surface step (A) and (B) a spot on the surface with a lower work function is illustrated with a dashed line.

The basic design of an STM is relatively simple, consisting of a positionable tip, and a sample holder. The tip's position has to be controlled in the X, Y, and Z planes with high accuracy, to within Angstrom resolution. It is also necessary to have sophisticated control electronics, which both apply a voltage difference between the tip and sample, and, depending on the operating mode, use the resultant current to

control the tip-sample distance. The tip's positioning is achieved by high accuracy

piezoelectronic positioners. A schematic of a scanning tunneling microscope is
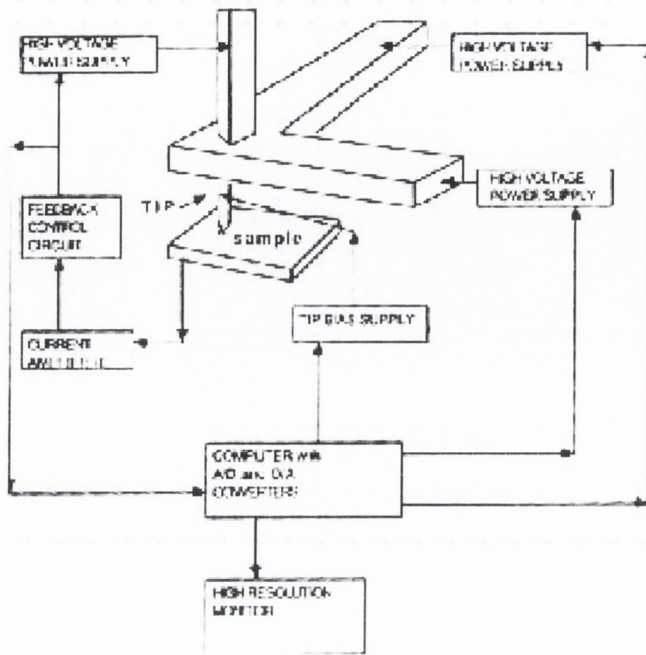
shown in

Figure 2.16. This schematic also illustrates how the positioners react to areas of

different conductivity when in constant current mode.

The STM can be operated in two modes. Constant current imaging uses the feedback
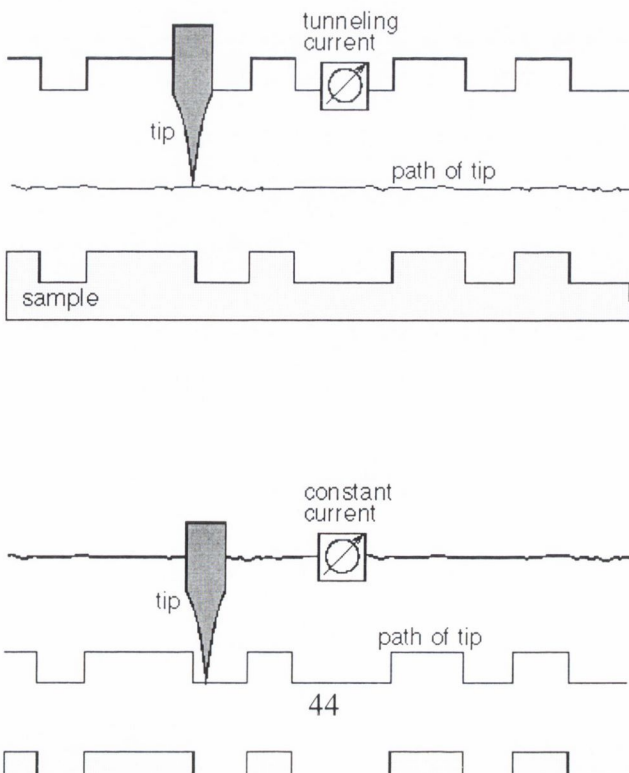
information from the measured current to adjust the tip-sample distance, while a voltage is applied. The tip-sample distance is altered depending on the change in tunneling current; if the tunneling current increases, the distance increases, and if the tunneling current decreases, the tip is brought closer to the sample.

Figure 2.17 Different operating modes of the STM[26].
Constant height mode (top), and constant current mode (bottom).

An alternative method is constant height mode where, the tip travels in a horizontal plane above the sample and the tunneling current varies depending on topography and the local surface electronic properties of the sample. The tunneling current measured at each location on the sample surface constitutes the data set, the topographic image. These two methods are illustrated in Figure 2.17.

The image of the tunneling current corresponds approximately to the topography of the sample. However, it is more complicated than this, as the tunneling current also corresponds to the electronic density of states at the surface. STMs measure the number of filled or unfilled electron states near the Fermi surface, within an energy range determined by the bias voltage. Rather than simply measuring physical topography, it measures a surface of constant tunneling probability. This has to be taken into account when imaging, but it also means that the STM can be used as a probe of local electronic structure, by using scanning tunneling spectroscopy (STS).

Scanning Tunneling Microscopy Theory

The STM can be modelled simply as electrons quantum mechanically tunneling through the potential barrier between the tip and sample. The theoretical basis for this model is outlined here, following the structure outlined elsewhere[26].

Quantum Mechanically, an electron is fully described by the Schrödinger Equation;

$$\left(\frac{-h}{2\pi}\right)^2 \frac{d^2\Psi(z)}{dx^2} + U(z)\Psi(z) = E\Psi(z) \qquad \textit{Equation 2.9}$$

Consider, as in the case of the STM, an electron incident on a potential barrier. Within the barrier, which is the classically forbidden region, the solution to the Schrödinger Equation is real, and has the form of an exponentially decreasing wavefunction.

$$\Psi(z) = \Psi(0)e^{-kz} \qquad k^2 = 2m(V_b - E)/h^2 \qquad \textit{Equation 2.10}$$

where V_b is the height of the potential barrier, i.e. the applied voltage, E is the energy of the state, m is electron mass. The tunneling current across this barrier is the transmission probability, proportional to the wavefunction squared.

$$I \propto e^{-2kd} \qquad \textit{Equation 2.11}$$

This is the case for a simple potential barrier, and the exponential dependence of current on distance is the signature of electron tunneling. However, the situation in the STM is more complicated, as both tip and sample have a characteristic local density of states (LDOS), which can be both non-uniform and discontinuous. When the tip is at a relative bias V to the sample, the tunneling current is directly proportional to the number of states on the sample surface within the energy interval eV. This will be finite for all samples, for semiconductors this will be low, for insulators it will be close to zero. For the STM it can be said that

$$I \propto \sum_{E_n = E_f - eV}^{E_f} |\Psi(0)|^2 e^{-2kz} \qquad \textit{Equation 2.12}$$

If V is small (such that the density of states doesn't vary significantly within this range), then this can be related to the LDOS at the Fermi level. For a separation z and energy E, the LDOS $\rho(z, E)$ of the sample is

$$\rho_s(z,E) \equiv \frac{1}{\varepsilon} \sum_{E_n=E-\varepsilon}^{E} |\Psi_n(z)|^2$$

Equation 2.13

for small ε. This says that the LDOS is the number of electrons per unit volume per unit energy, for a given position and energy. Using the definition given in Equation 2.13 the right hand side of Equation 2.12 is proportional to the Fermi-level LDOS of the sample at the tip surface, where z, the height above the sample, is equal to W, the tip displacement.

$$\sum_{E_F-eV}^{E_F} |\Psi(0)|^2 e^{-2kW} \equiv \rho_s(W, E_F) eV$$

From this, and equation 2.12, the tunneling current can be expressed as

$$I \propto \rho_s(W, E_F) V$$

Equation 2.14

From this, and under the above approximations, the tunneling current can be expressed as a function of the sample LDOS and applied voltage.

Scanning Tunneling Spectroscopy

As said above, the STM is not purely a topographic tool, but the measured tunneling current is highly dependent on the electronic structure of both the tip, and the sample. This has disadvantages when imaging, as both an increase in sample conductivity and an increase in height have the same effect, an increase in measured current. However,

this disadvantage when imaging is more than compensated for, as this sample

dependence gives us a vast amount of information about the local electronic structure

of the sample. Due to the small region (~Angstroms), electronic structure information

can be obtained on a near atom-by-atom basis.

Under the assumptions that i) the tip has a uniform density of states, ii) voltage is

relatively low (typically < 10mV), iii) low temperature, the Tersoff-Hamann theory

predicts that the tunneling current (I) is[26]

$$I \cong R^2 V \phi^2 e^{2kR} k^{-4} D_t(E_F) \rho(r_0, E_F)$$ *Equation 2.15*

where D_t is the density of states per unit volume of tip, R is the tip radius, $\rho(r_0, E_F)$ is

the density of states of the sample, measured at the position below the centre of the

tip. K is the inverse decay length. When the above conditions apply, and at constant

tunneling current, the contour that the tip follows is essentially of constant Fermi level

density of states. Due to the constraints of the assumptions, this theory is of only

limited use, as a typical STM can range over a number of volts. The assumption that

all electrons tunneling from the Fermi level is no longer valid, as electrons can tunnel

from a range of states near the Fermi level.

In this case, a tunneling model based on the Wentzel-Kramer-Brillouin approximation

is more useful. The WKB model predicts that the tunneling current is given by

$$I = \int_0^{eV} \rho_s(r, E) \rho_t(r, -eV + E) T(E, eV, r) dE$$ *Equation 2.16*

$\rho_s(r,E)$ and $\rho_t(r,E)$ are the density of states of the sample and tip at position r, and

energy E with respect to each of their Fermi levels. The tunneling probability T(E,

eV, r) in this case for an electron with energy E, at an applied bias of V is

$$T(E, eV) = \exp\left[\frac{-2Z\sqrt{2m}}{h}\sqrt{\frac{\Phi_s + \Phi_t}{2} + \frac{eV}{2} - E}\right]$$ *Equation 2.17*

By varying the applied bias, it is possible to select which states dominate the tunneling process. From this it is possible to determine the LDOS. For example, the current will increase strongly if the applied bias allows the onset of tunneling into a dense unoccupied range of the sample's LDOS. From this it can be seen, that as a rough approximation, the LDOS can be related to the first derivative of the I-V curve dI/dV. As the electrons in the highest energy states have the lowest potential barrier to tunnel through, most of the tunneling current will arise from electrons near the Fermi level of the negatively biased electrode. Assuming a constant density of states for the tip, and neglecting the influence of the applied voltage on the potential barrier (reasonable for eV<<ϕ) then the current-voltage curve can be related to the density of states as follows:

$$\frac{dI}{dV} = e\rho_s \rho_t \exp\left[-A\sqrt{\Phi - \frac{eV}{2}}\right]Z$$ *Equation 2.18*

Methods of Tunneling Spectroscopy

This electronic structure information can be obtained in a variety of methods. The simplest is constant current imaging, at range of voltages. The relative apparent 'heights' of different features in the image will correspond to characteristics of the electronic structure. Current-voltage (I-V) curves are rapidly acquired at different fixed locations, as the tip scans through the image. The advantage of this is the ease with which electronic structure can be correlated to topographic position. Additionally multiple I-Vs over an area can be acquired, e.g. in a 32x32 grid. For this method, the feedback mechanism that ensures constant current has to disabled briefly

as the current-voltage curve is taken. When the feedback system is active, while imaging, a constant voltage is applied. The feedback mechanism will adjust the tip height to maintain the current setpoint. When I-Vs are taken, the feedback mechanism serves to keep the tip fixed. The voltage is ramped up in discrete steps between two voltage points, and the current is measured for all these. A typical time to take an I-V would be 400 μsec. This ensures that drift of the tip is minimised, so the topography-LDOS correspondence is accurate.

As said earlier, the tunneling current drops off exponentially with distance. This poses a problem when imaging semiconducting materials; as the tunneling current will pass through a large dynamic range, from extremely low currents below the bandgap, to energies above the bandgap tunneling into the conduction band. Using a fixed separation and current setpoint poses problems due to the range, as information at one or other end will be too high or low to measure.

A solution proposed by Feenstra[27] is to move the tip according to a fixed contour as the I-Vs are taken. Usually a V-shaped contour is chosen. The tip will be close to the sample at 0V, and far away at high negative and positive voltages. Because the exponential dependence of the tunneling current is well defined, it is easy to scale the measured currents to take account of the amplification of low voltages. A further modification is also necessary. The LDOS is normalised by taking it as dI/dV(V/I). As V goes to zero, this will diverge. The solution proposed by Feenstra was to take I/V as

$$\frac{I}{V} = \int_{-\infty}^{+\infty} \frac{I}{V} \exp\left(\frac{|V' - V|}{\Delta V}\right) dV'$$

Equation 2.19

This substantially reduces the divergence by avoiding the singularity at V=0.

2.2.2 Transmission Electron Microscopy[28]

Transmission Electron Microscopy (TEM) can provide detailed structural information about samples, with resolution typically of the order of nanometres. High resolution TEM can resolve structure down to atomic dimensions, and is capable of resolving individual shells of MWNT. It images structure by transmitting a beam of high-energy electrons (in this study, usually a 100kV accelerating voltage is used) through a sample (see Figure 2.18). Electrons at this energy have a much shorter wavelength than light, and therefore the resolution will be much higher. For example, an electron accelerated to 100keV will theoretically have a resolution limit of 0.0037nm. This is much lower than atomic dimensions, but other factors limit the resolution limit to much more than this. These factors include grain size of film used, or pixel size of CCD camera, lens aberrations, and how monoenergetic the electron beam is. In addition, a further limitation is that an extremely high intensity beam is needed to achieve discernable contrast at high magnifications. Such intensity is difficult to achieve, and in any case, would significantly damage most organic samples. An advantage of higher accelerating voltages is that thicker films can be imaged due to the increased penetration depth.
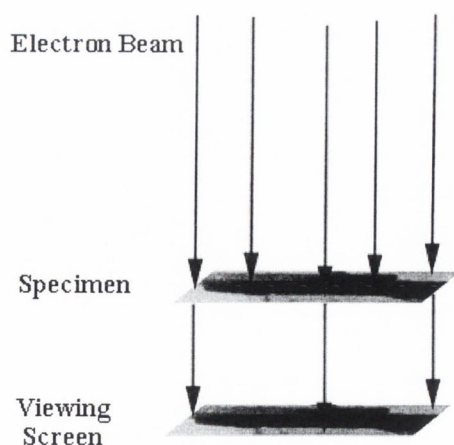
Figure 2.18 Basic Principle of a TEM.

TEM is much more limited than its counterpart of Scanning Electron Microscopy in which samples it can image. The sample has to be mounted on special grids, in this case of 4mm diameter. Furthermore, the electron beam has to penetrate the sample fully, which limits both the nature and the thickness of the sample used. This is usually not a problem in this case as all sample films are cast from solution, and so thin films can easily be achieved.

Design of the TEM[28]

The design of the TEM is similar to that of a light microscope, consisting of an electron source, condenser system, sample stage, an objective lens, and a projection system (Figure 2.19).
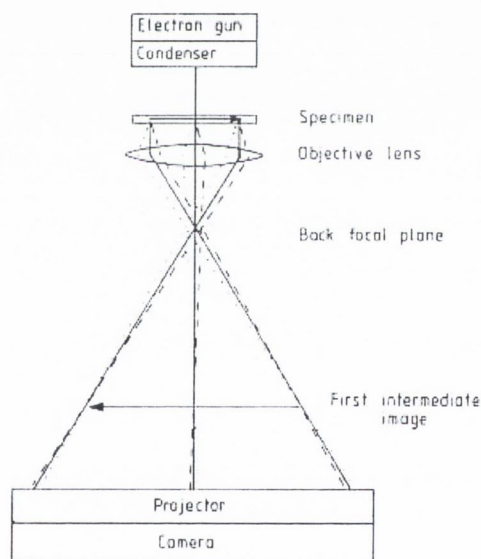
Figure 2.19 Layout of a transmission electron microscope[28].

A typical electron source consists of a sharp tungsten filament heated to emit electrons by thermionic emission. An alternative method of producing an electron beam is to use a field emission source, used in high-resolution studies as the beam is more highly collimated. This source is held at a large negative voltage, so that emitted electrons can be accelerated towards a positive electrode placed in front of the

filament. This creates a monoenergetic beam that passes through a hole in the anode into the lens system. The lens system consists of electromagnets, creating a magnetic field that can shape the electron beam. Focussing can be achieved by varying the current that flows through the electromagnets, and the magnetic field created, hence the strength of the lens. This is one advantage over conventional light microscopy, where lenses have a fixed focus, and so changing the focus requires either changing the lens or the position of the lens or sample. The condenser lens widens the beam so it will cover the sample, and projects this onto the sample. After transmission through the sample, this passes through to the objective lens and projection system, which form an image and magnify this, projecting it down onto a phosphor screen, from which the image can be observed. Alternatively, to record an image, a CCD system or photographic film can replace the phosphor screen.

2.2.3 Optical and Vibrational Spectroscopy

Spectroscopy encompasses a vast range of techniques to characterise the electronic, chemical and physical structure of materials. Optical and vibrational spectroscopies are used to gain understanding of materials by their interactions with photons and indirectly, in the case of vibrational spectroscopies, phonons. Here the various spectroscopies used in this work are outlined. The relevant physics of the materials has been described in the section entitled Photophysics of Conjugated Polymers on page 28.

Optical Spectroscopy

The two principle optical spectroscopic techniques used are the complementary techniques of absorption and fluorescence spectroscopy. These two techniques

examine to optical excitations and de-excitations of materials, and can give a great deal of information about the material and its local environment.

UV-Visible absorption spectroscopy is a relatively simple technique that can give a great deal of information about polymers and the local environment of those polymers. It involves passing a monochromatic beam of light through a sample and measuring the absorption of the material at this wavelength. This absorption is measured as a function of frequency over a frequency range from infrared to ultraviolet. The absorption is usually measured in reference to a blank sample in a double beam arrangement, to eliminate variations caused by the differences in lamp intensities at different frequencies. Typically, measurement ranges here were 900nm down to 200nm.

As the photons pass through a material, it is possible that photons of a suitable energy can interact with the material, resulting in an electron being excited to a higher energy state, and the photon being absorbed. By measuring the amount of light absorbed for a particular wavelength, it is possible to deduce information about the electronic structure of the material. In conjugated polymers, UV-Visible absorption is primarily due to π-π^* transitions, as the energy gap between these levels ranges from near UV to infrared. Excitations from σ electrons are in the near to far ultraviolet, so these are correspondingly left unaffected by the measurements in this study. As ultraviolet light affects these σ bonds, it tends also to alter the polymer's structure, resulting in photo-degradation of the polymer.

As will be seen later, different parts of the polymer are excited at different frequencies. This is useful as it allows us to use UV-Visible spectroscopy as a probe to determine how the polymer is affected by changes in its environment due to such

factors as solvent interaction, concentration changes leading to aggregation, and in this case, the introduction of nanotubes to a polymer solution.

Fluorescence spectroscopy is a useful companion technique to absorption spectroscopy, in that as absorption spectroscopy probes the energies of excitations to higher states, fluorescence spectroscopy probes the energies at which these excited electrons radiate as they decay back to the ground state. Usually a fixed wavelength is used to excite the polymer, and a range of wavelengths are examined for light emitted as the electron decays, giving information about the electronic transitions available to the electron as it decays.

When a π-electron in a solid is excited by a photon, it is promoted into an unstable excited state. This excess energy may be lost in a number of ways, both radiative and non-radiative. These involve the loss of energy as photons and vibrational phonons respectively. On excitation, the electron finds itself in an excited vibronic state of the excited electronic state. Neglecting intersystem crossing and internal conversion, the electron falls very rapidly to the lowest energy state of the vibrational manifold. It is only now ready to undergo radiative decay. The electron can decay into any vibrational state of the ground electronic state with probability amplitude related to the overlap of the wavefunctions of the initial and final state. Thus, the luminescence profile is indicative of the vibrational structure of the ground state.

Vibrational Spectroscopy

Raman Spectroscopy is an extremely useful technique to characterise organic materials. It gives information about the vibrational frequencies of a material, and hence on the structure of that material. It can be used, for example, to identify both individual carbon nanotubes, and the quality of bulk nanotube samples, as there are

both modes that are common to all carbon nanotubes, and there are modes that are strongly diameter dependent, and hence on chiral vector[29]. It can also indicate conformation of polymers, as the vibrational frequencies will be strongly affected by this.

A basic Raman spectrometer is in essence very simple; it consists of a light source, usually a laser, which is shone onto the target, and the light scattered from this is passed into a monochromator and a photomultiplier. The monochromator is cycled through the frequency region of interest, and this gives the resultant Raman spectrum. It has the advantage that, as it analyses the light scattered from the material, it can be used on virtually all samples, in powder or solution form, and requires very little sample to work with. Inelastically scattered light is much weaker than elastically scattered light by a factor of 10^4, so the light source does have to be intense, hence the use of a laser light source, and the optics do have to be highly sensitive.

Transitions between vibrational states can result from the scattering of radiation from molecules. In such scattering processes, the incident radiation can be of an energy that is greater than the energy difference between the vibrational states; for example, the incident radiation can be in the UV or the visible region. The frequency of light that is scattered off the molecules can be of the same or different frequency than the incident light. When the incident frequency equals the scattered, the scattering is referred to as Raleigh or Mie scattering. When the scattered frequency differs from the incident frequency, the scattering is referred to as Raman scattering.
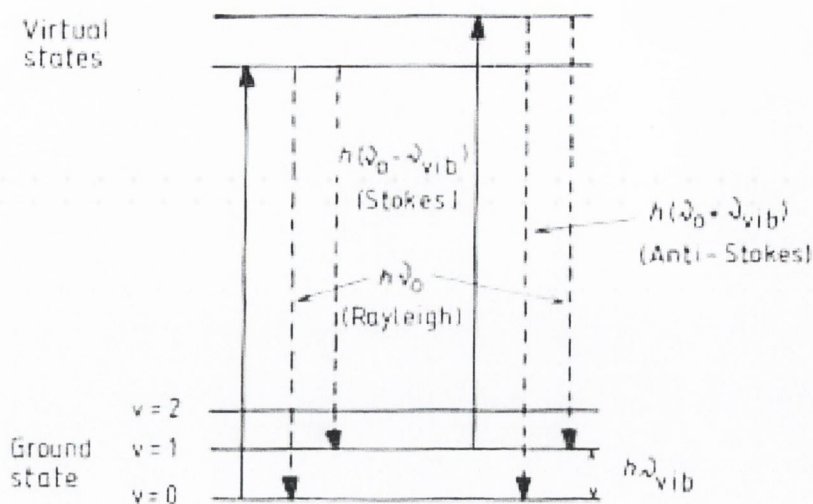
Figure 2.20 Energy Transitions for elastic and inelastic scattering.

In Raman scattering, the difference in frequency between scattered and incident light is equal to a vibrational frequency. There are two types of Raman scattering, Stokes and anti-Stokes. In Stokes Raman scattering, the molecule starts out in a lower energy vibrational state and after the scattering process ends up in a higher energy state. In anti-Stokes Raman scattering, the molecule begins in a higher energy vibrational state and after the scattering process ends up in a lower vibrational state. These are illustrated in Figure 2.20.

2.3 Conclusions

In this chapter, the science of these materials has been reviewed. Beginning with the chemistry of organic materials, this has been extended to explain the physics of conjugated polymers and carbon nanotubes. The photophysics and theoretical basis of conjugated polymers has been outlined. Electronic and physical properties of carbon nanotubes have been summarised.

The experimental theory of relevance to this study has been explained. This encompasses microscopy, as Transmission Electron Microscopy, and Scanning

Tunneling Microscopy. The theories of the optical and vibrational spectroscopies used in this study have also been described.

References

[1] M. Pope, C.E. Swenberg, *Electronic Processes in Organic Materials*, Clarendon Press, Oxford, (1982).

[2] G. Natta, G. Mozzanti, P. Corrandini, *Att. Acad. Naz. Lincei. A. Sci. Fis. Mat. Nat. Rend.*, **25,** 2 (1956).

[3] T. Ito, H. Shirakawa, S. Ikeda, *J. Polym. Sci. Chem.,* **12**, 11 (1974).

[4] H. Shirakawa, T. Ito, S. Ikeda, *Polym. J.*, **4**, 460 (1973).

[5] C.K. Chiang, C.Z. Fincher, Y.W. Park, A.J. Heeger, E. Shirakawa, E.J. Lown, S.C. Gau, A.G. Mac Diarmuid, *Phys. Rev. Lett.*, **39C**, 1098 (1977).

[6] C.S. Vannoni, T.C. Clarke, *Phys. Rev. Lett.*, **51**, 1191 (1983).

[7] R. Peierls, *Quantum Theory of Solids*, Oxford University Press, Oxford (1955).

[8] R.H. Baughman *et al*, *J. Polym. Sci, Polym. Phys. Ed.* **14**, 2037 (1976).

[9] A. Kearwell and F. Wilkinson, *Transfer and Storage of Energy by Molecules* (G. M Burnett and A. M. North, eds.) Vol. 1, Wiley, New York (1969).

[10] R. P. Wayne, *Photochemistry*, Butterworths and Co. (1970).

[11] W.P. Su, J.R. Shrieffer, A.J. Heeger, *Phys. Rev. Lett.,* **42**, 1968 (1979).

[12] D. Baeriswyl, K. Maki, *Phys. Rev. B*, **31**, 6633 (1985).

[13] S. A. Brazovskii and N. N. Kirova, JEPT Lett. 33, 4 (1981)

[14] M. Gabrowski, D. Home, J. R. Schreiffer, *Phys Rev. B,* **31**, 7850 (1985).

[15] U. Sum, K. Fesser, H. Buttner, *Solid State Comm.*, **61**, 607 (1987).

[16] H.E. Kroto, J.R Heath, S.C. O'Brien, R.F. Curl, R.E. Smalley, *Nature*, **318**, 162 (1985)

[17] S. Iijima, *Nature*, **354**, 56 (1991).

[18] S. Iijima, T. Ichihashi, *Nature*, **363**, 603 (1993).

[19] M S Dresselhaus, G Dresselhaus, P C Eklund, *Science of Fullerenes and Carbon Nanotubes*, Academic Press, New York (1996).

[20] J.W.G. Wildoer, L.C. Venema, A.G. Rinzler, R.E. Smalley, C. Dekker. *Nature*, **391,** 59 (1998).

[21] P. Lambin, A. Fonseca, J.P. Vigneron, J. B.Nagy, A.A. Lucas, Chem. *Phys. Lett.*, **245**, 85 (1995).

[22] R. Saito, M.S. Dresselhaus, G. Dresselhaus, *J. Appl. Phys.*, **73**, 494 (1993).

[23] J.C. Charlier, J.P. Michenaud, *Phys. Rev. Lett.*,**70,** 1858 (1993).

[24] G. Binnig, H. Rohrer, *Helv. Phys. Acta*, **55**, 726 (1982).

[25] R.H. Fowler, L. Nordheim, *Proc. Roy. Soc.*, **A119**, 173 (1928).

[26] Dawn A. Bonnell, Scanning Tunneling Microscopy And Spectroscopy, VCH, London (1993).

[27] R.M. Feenstra, *Phys. Rev. B*, **50,** 4561 (1994).

[28] B.J. Hunt, M.I. James, *Polymer Characterisation,* Blackie Academic & Professional, (1993).

[29] R. Saito, M. S. Dresselhaus, G Dresselhaus, *Physical Properties of Carbon Nanotubes*, Imperial College Press (1998).

Chapter 3

Sample Preparation and Experimental Methods

3.1 Introduction

In this chapter, the main experimental procedures will be described. These fall into two broad categories; those of materials synthesis, and those experimental techniques and methods employed to characterise the composite. Materials synthesis encompasses the synthesis of PmPV, the production of carbon nanotubes by several different methods, and the optimal techniques for preparation of both SWNT- and MWNT-based composites. The experimental methods applicable to the relevant experimental techniques will also be briefly reviewed.

3.2 Materials Synthesis
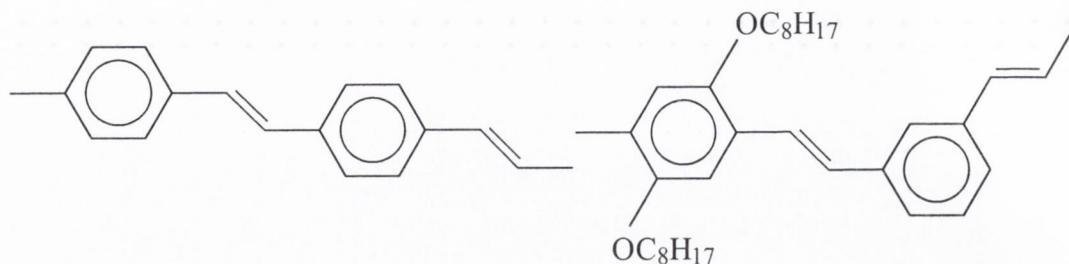
Figure 3.1 Comparison between the standard PPV (a) and PmPV (b). Aliphatic side groups have been added to the para linked phenyl to solubilise the polymer. In addition to this approximately one third of the repeat units contain a meta-linked phenyl. This adds curvature to the chain, causing it to form into a helix like shape. It also disrupts conjugation, and so reduces vibronic electronic decay as well as blue shifting emission, without compromising thermal stability by the introduction of non-conjugated regions[1].

All conjugated materials were synthesised by the research group in TCD. The conjugated polymer used was poly(p-phenylenevinylene-co-2,5-dioctyloxy-m-phenylenevinylene), PmPV. This is a derivative of the more widely studied polymer polyphenylenevinylene (PPV). The difference in these polymers is that PmPV is a co-polymer with some of the repeat units altered by changing the phenyl linkage to a *meta* conformation rather than a *para* one. This is shown in Figure 3.1.

3.2.1 Polymer Synthesis

The starting material in both cases is hydroquinone. This material is reacted with potassium hydroxide and bromooctane in a solution of dimethyl sulphoxide (DMSO) to form 1,4 dioctoxybenzene. This material will eventually become the substituted *meta* phenyl on the polymer backbone.

A methyl bromination is performed on 1,4 dioctoxybenzene using potassium bromide and paraformaldehyde in the presence of acetic and sulphuric acids to produce 1,4-Bis (2,5-di-n-octoxy) bromomethyl benzene. This was then heated with triethyl phosphite

to form the Horner ester, 1,4-Bis (2,5-di-n-octoxy) phenyl diethyl phosphonate. This material is the immediate precursor of the polymer.
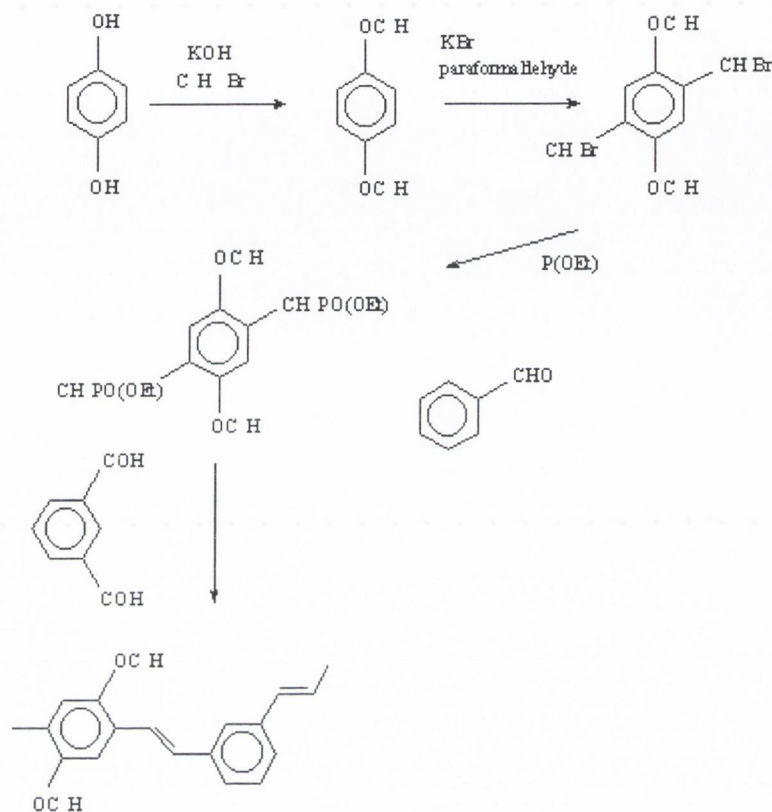
Figure 3.2 Reaction routes for synthesis of PmPV.

The conversion of the precursor to polymer is done by the Horner-Emmons condensation reaction. For the polymer, the ester is reacted with isopthaldehyde. This molecule has two CHO groups (in the *meta* position) compared with benzaldehyde's one. This means that when it reacts with the Horner ester there is still a free CHO group to react with another ester molecule. This can continue until the reaction is quenched to produce a long chain polymer. It should be noted that if the precursor were reacted with para-pthaldehyde the result would be all *para* PPV. In the case of the polymer a polycondensation reaction terminates the reaction.

The introduction of *meta* linkages introduces two main effects, one steric and one electronic. Energy minimisation calculations for a perfect PmPV chain in which all the vinylene double bonds are in the *trans* position have been carried out[2]. These show that a single PmPV strand tends to form a planar strand with a slight helical twist. In comparison, all-*trans* PPV is a planar molecule. This is one reason why we chose to work with this polymer. Its slight curvature should make the molecule much more flexible. This should enable it to interact with a nanotube over the whole of its length through bending and hence provide a stronger interaction. In reality however, there will always be some *cis* linkages but Horner PmPV has been characterised as having a very low *cis-trans* ratio.

The electronic change is due to the interruption in conjugation caused by the introduction of the *meta* linkage. This has a number of effects. The band gap or HOMO-LUMO transition is widened because of the shortening of the average length of conjugated sections. This is due to the increased localisation of π electrons and increased degeneracy of the system. In addition, phonon propagation along the chain is interrupted, reducing the probability of non-radiative decay. This both increases luminescence efficiency for optical applications and blueshifts the emission. Conjugation can also be broken by the introduction of non-conjugated sections to the chain. However, unlike the introduction of *meta*-linked phenyls, introduction of saturated segments degrades the thermal stability of the material. In summary, introduction of the *meta* linkage is desirable in that it blue shifts and increases the polymers light emission compared to PPV without decreasing the polymers thermal stability.

3.2.2 Nanotube Synthesis

Since their discovery[3], carbon nanotubes have caused a great deal of interest due to the extra-ordinary electronic and mechanical properties predicted. However, it is probable that nanotubes and fullerenes were made by Bacon[4] as early as 1960, unknown to him, using an arc discharge apparatus to produce carbon whiskers. The breakthrough in Fullerene science took place in 1985[5] when Harry Kroto, Richard Smalley and Robert Curl discovered a new carbon allotrope with remarkable geometric ordering. These C_{60} or 'buckyball' molecules drove many groups to start looking into the production and analysis of carbon filaments further. As a production technique, it was first developed by Krätschmer *et al* .in 1990[6] to produce fullerenes in large quantities. The optimal conditions necessary to produce carbon nanotubes in a Krätschmer generator were found in 1992[7] by Ebbesen and Ajayan.
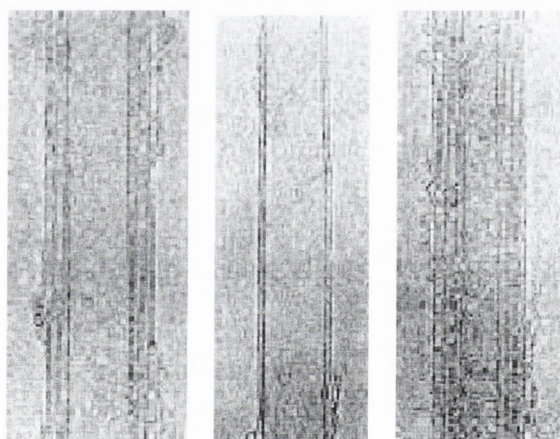
Figure 3.3 High Resolution TEM of MWNT[7].

This was further optimised later by Journet *et al.*, to produce large quantities of relatively pure SWNT[8].

Nanotubes in this work were made by two different processes. The most important is by the Arc Discharge Method (ADM), which was employed to make all single-walled samples, and some multi-walled samples. The only other method employed here is by

Catalytic Decomposition of Acetylene (CDA). Dr. Bernier's group in Montpellier supplied the single-walled nanotubes. The multi-walled nanotubes were made both in Trinity College (ADM nanotubes), and in Professor B.Nagy's group in Namur (CDA nanotubes). As is seen, the method of production drastically affects the characteristics of the nanotubes produced.

Arc Discharge Method
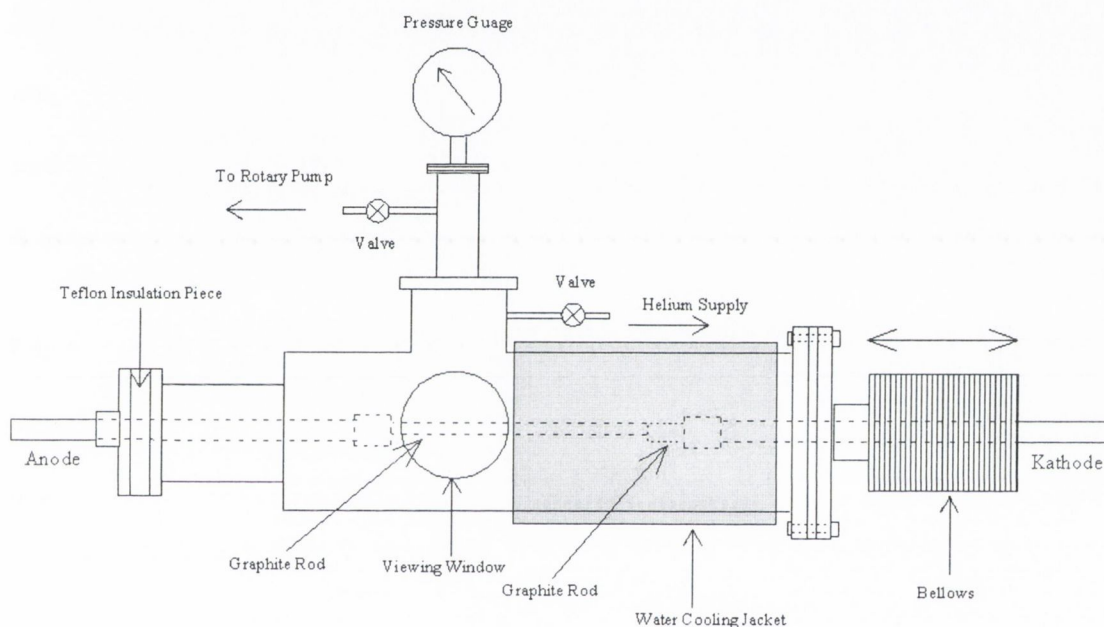
Figure 3.4 Schematic of a Krätschmer Generator as used in TCD.

The basic principle of a Krätschmer generator is to create a plasma between two carbon electrodes by driving a current between them. This takes place in a controlled inert environment, and as the carbon vapour sublimes out of the plasma, carbon nanotubes form readily. These precipitate onto the anode in the case of MWNT, and onto the chamber walls in the case of SWNT.

The Krätschmer generator in TCD consists of a cylindrical chamber approximately 300 mm long and 100 mm in diameter, shown in Figure 3.4. This chamber is water cooled, evacuated and filled with an inert gas. For MWNT this is usually helium but

for single walled nanotubes (SWNT), other gases such as argon and nitrogen can be used. Enclosed in the chamber are two graphite electrodes, a stationary anode made of 95% pure graphite and a 99.99% pure moveable cathode. The purity of the cathode is important, as it is this material that is consumed to form nanotubes.

Experimental Procedure

The power to sustain the arc is provided by a small DC welding supply (Thytronic 125) that delivers up to 3.2kW. In addition, a multimeter (Keithley 169) is attached across the generator to monitor the potential difference between electrodes. The cathode has a diameter of 6mm and a length of about 5cm. The anode's diameter is 4.5mm with an initial length of about 20cm.

Due to the high currents involved in maintaining the arc plasma and consequent large heat dissipation, cooling is necessary around the region of the arc. This is done by the use of a water-cooling jacket attached to the exterior of the main housing. Both sides of the generator are insulated from each other. Helium is used to provide an inert atmosphere. While the anode stays fixed during the experiment, the cathode holder has a bellows mechanism that allows translation towards the anode. Maximum bellows contraction is 4.8cm.

The chamber is evacuated and refilled with helium. This is done three times to remove the oxygen, preventing the formation of CO and CO_2. For the production of Nanotubes a pressure of ~400-500 Torr appears to be optimal[9], while for the production of Fullerenes 100-200 Torr is usually chosen.

Plasma ignition is initiated by applying the power and pulling the rods apart. The actual rod distance cannot be seen during the experiment, but it can be varied from

0.5mm to almost 10 mm. The plasma light can be observed indirectly through the view port of the chamber as well as the amount of soot that is being produced. This allows the stability and intensity of the plasma to be monitored.

During the experiment, the cathode is consumed and a deposit forms on the anode. In contrast to former experiments with this generator, not the brightness of the arc is taken as an indicator for the optimum burning condition, but the voltage. The voltage is monitored by a multimeter and maintained at a certain value. A potential difference of 22V has been found to be optimal[9]. The voltage depends on the distance between the rods. By slowly moving the cathode towards the anode and aiming to keep the voltage constant, one gets a more or less stable arc discharge. Due to the vapour produced during the experiment, the pressure increases and it is necessary to open the valve to the rotary pump from time to time. Upon full completion, a cylindrical deposit of about 6cm in length is found on the anode, shown in Figure 3.5.
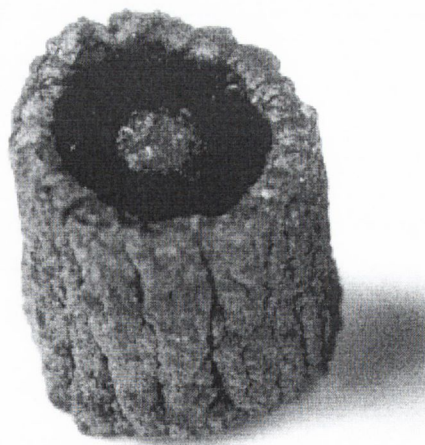
Figure 3.5 Cylindrical deposit where nanotubes are found between the core and shell.

The deposit consists of a grey hard outer shell, which is rich in polyhedra with some nanotubes and amorphous carbon. The inner core is under ideal conditions a black,

soft and fibrous material that can be easily removed from the inside. The usual method of removal is to break the deposit open and scrape the powder inside out with a spatula.

Production of Single-Walled Nanotubes

Although Iijima's first observations were of multi-wall nanotubes, he observed single-wall carbon nanotubes less than two years later[10], as did Donald Bethune and colleagues at IBM in California[11]. In the case of the IBM group, they were trying to put cobalt inside fullerenes. Cobalt powder was put in one of the electrodes and the generator was allowed to arc. However, instead of metallo-fullerenes they found rubbery soot. TEM images showed this soot to contain intricate ropes of carbon fibrils with diameter of approximately 1.2 nanometers. It was found that nickel works as well and a 50/50 mixture of nickel with cobalt gave optimum amounts of these single-walled nanotubes. It is clear that these metals work as a catalyst, preventing the growing tubular structure from wrapping around and closing into a smaller Fullerene cage. The presence of the metal also lowered the temperature of the plasma. Without this cooling process, the nanotubes can coalesce and merge. Figure 3.6 shows a micrograph of single-walled nanotube ropes clearly showing individual nanotubes in ropes.

More recently, P. Bernier and co-workers at Montpellier developed a method to produce arrays of single walled nanotubes with high product yields[8]. Ordered nanotubes were produced from ionised carbon plasma, and joule heating from the discharge generated the plasma. Using a 1 at. %Y and 4.2 at. % Ni, they observed large quantities of rubbery soot on the chamber walls, web like structures between the cathode and the chamber walls (which only appeared when the catalysts were

present), and a collar containing black, porous material. The resultant yield was in the range 70-90%, an average diameter of 1.4 nm, and arranged into crystalline bundles with a diameter in the range of 5 to 20 nm. They conclude that the use of the second catalyst (e.g. Yttrium) in the production is vital to the process, and is responsible for the high tubule yield. In a scanning electron microscope, the nanotube material produced by this method looks like a mat of carbon ropes.
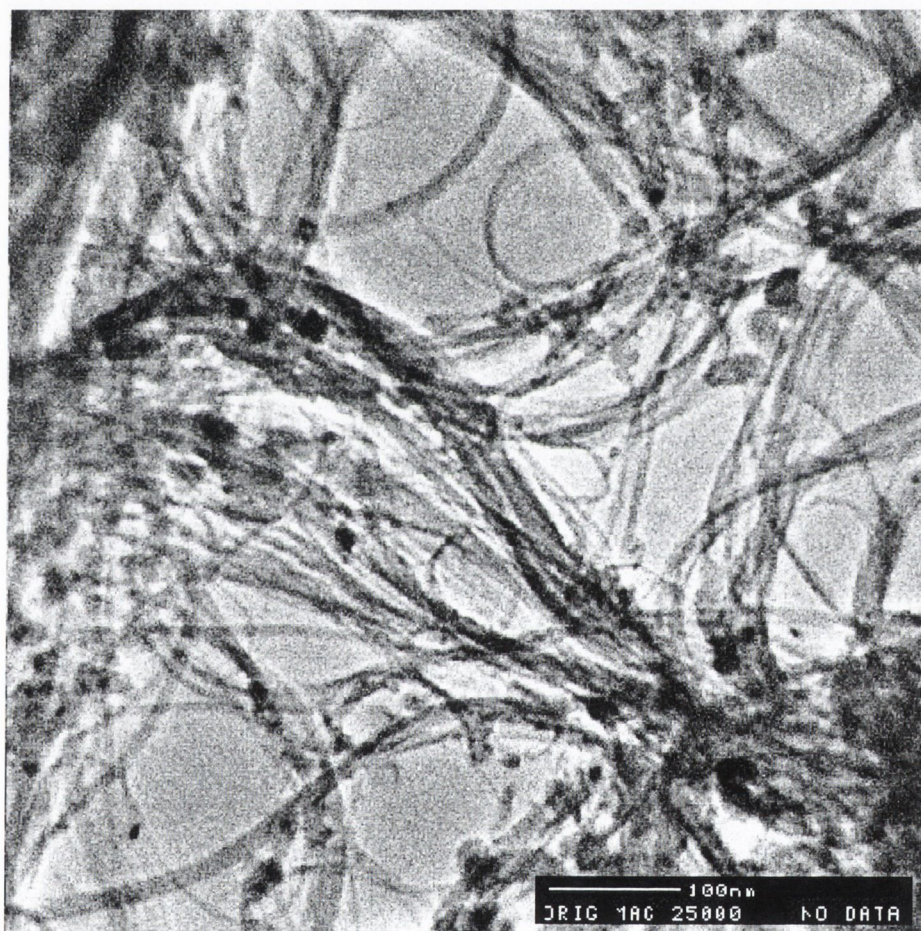
Figure 3.6 High-resolution micrograph of SWNT ropes produced by arc-discharge[12].

Production of Nanotubes by Catalytic Decomposition of Acetylene

The other production technique used in this thesis was by catalytic decomposition of hydrocarbons aided by transition metal oxide catalysts, carried out by B.Nagy and colleagues, Namur[13]. A typical reaction would be passing a hydrocarbon mixture (10% acetylene in an inert buffer, typically nitrogen) over a catalyst bed in a flow

furnace for several hours at temperatures typically in the region of 1000 degrees Celsius. A typical TEM of a sample produced by this method in given in Figure 3.7. These nanotubes tend to form large networks of interconnected nanotubes, due to their long length and low numbers of shells, which makes them highly flexible. Nanotubes produced by this method tend to be only partly graphitised, with a large number of defects. This means that the carbon atoms are not always sp^2 hybridised and therefore do not always form hexagons. Defect sites in the form of pentagons and heptagons are common. Irregular structures, such as helical nanotubes are also commonly observed[14].
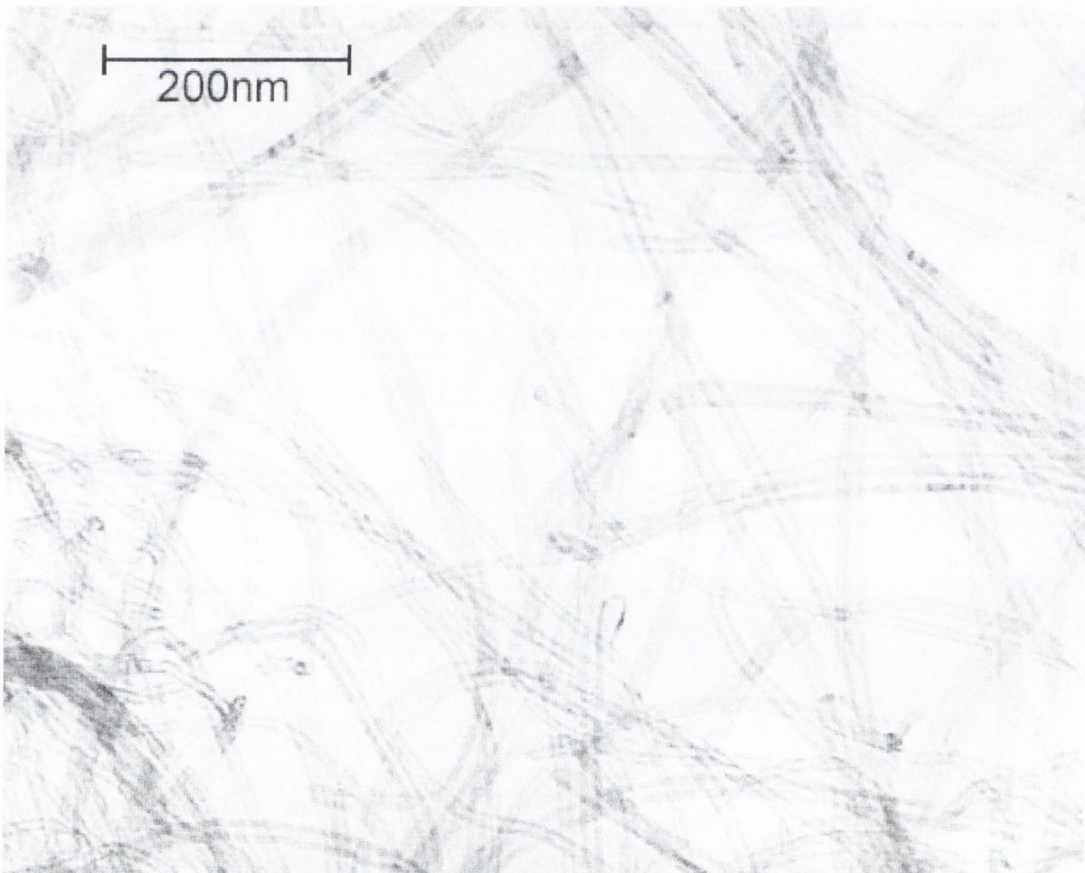
Figure 3.7 TEM of a typical sample produced by catalytic decomposition of acetylene.

3.2.3 Composite Preparation

The method was similar for preparation of both MWNT-based and SWNT-based composites, differing mainly in concentration of sample used.

Preparation Technique

1. A small amount of PmPV (typically 5-50mg) is weighed out on wax weighing paper. This is carefully poured into a suitable sample bottle. To this, toluene is added to make a solution of known concentration (typically a concentrations of between 0.5g/L and 20g/L were made). This is then sonicated until the PmPV is well dissolved in the toluene.

2. A mass of nanotube soot (0.5% to 400% that of the PmPV) is weighed out. This is added to the PmPV solution.

3. This is ultrasonically agitated using a high power sonic tip. This has the effect of dispersing the raw nanotube soot in the solution, so that it appears homogeneous to the eye. This greatly accelerates the interaction process, due to the much larger surface area of the exposed soot. However, it is believed that overexposure to sonication can damage the nanotubes, and hinder interaction between the two components due to the extreme agitation.

4. To avoid this, the solution is transferred to a low power sonic bath, where it is gently agitated for a number of hours. This assists interaction between polymer and nanotube by further breaking up aggregates and ropes, and by bringing the two components into more intimate contact.

5. The bulk of the excess uncoated nanotubes were removed. This is done in the case of MWNT-based composites by allowing the solution to stand for several hours, and then decanting it. For SWNT-based composites, the excess is removed either by pipetting off the solution from the sponge-like precipitate, or by filtering the solution using a large pore filter.

In all cases, the result of this procedure is a solution that is darker than the original, almost black in the case of high concentration MWNT composites, but only slightly darker for SWNT composites. The maximum weight of nanotubes that can be held in stable solution by PmPV is highly concentration dependent, but for all cases, the mass of MWNT is two orders of magnitude greater than the SWNT. The highest mass fraction of CDA MWNT that was prepared was 400%, for ADM MWNT it was 80%. Note that these mass fractions refer to mass of raw sample added, which vary widely from sample to sample, and in all cases, there was some precipitate. However, the precipitate has been characterised as being predominantly non-nanotube graphitic particles[15]. Maximum mass fractions of SWNT achieved were typically of the order of 1%; most masses higher than this aggregated substantially, and were removed during the final stage of composite preparation. SWNT themselves tend to aggregate substantially, the majority forming ropes. This hinders interaction with, and coating by, the PmPV, hence limiting the amount of SWNT that can be held in solution. PmPV forms aggregates[16], and so the saturation level for all types of nanotubes is highly concentration and solvent dependent.

Comparison between MWNT and SWNT Composites

Figure 3.8 shows a TEM image of the MWNT composite (Prof. Ajayan, Rensselaer Polytechnic Institute) published in the original paper on PmPV/nanotube composite materials[17]. Several nanotubes can be seen protruding from the film. Enveloping these protruding nanotubes is a thin film of PmPV. Immediately noticeable is the good wetting of the nanotubes by the PmPV, giving the first clear indication of how the PmPV solubilised the nanotubes. The nanotubes are also well dispersed, showing that the PmPV is effective at breaking up the initial aggregates, and keeping them separated.

Figure 3.8 TEM of Arc Discharge Method MWNT Composite.

Figure 3.9 shows a composite of PmPV and catalytically grown nanotubes. The structure of the aggregates can be seen as unchanged from the raw powder shown in Figure 3.7, although the intertwined aggregates shown here do tend be smaller and more numerous as they are broken up by sonication.
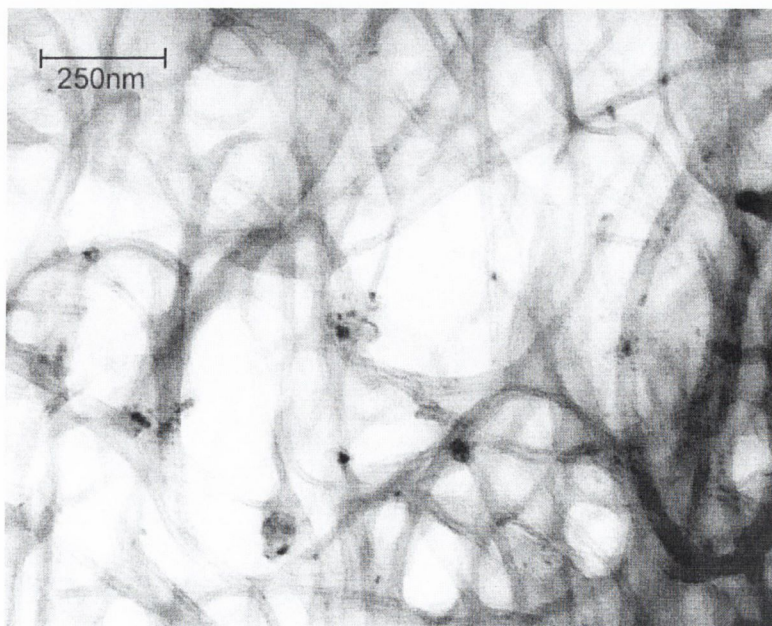
Figure 3.9 TEM of Catalytically grown MWNT Composite.

The defects affect the interaction of the nanotubes with the PmPV, which will be discussed in more detail later.

3.3 Experimental Techniques

3.3.1 Electron Microscopy

Two principal forms of Electron Microscopy were carried out, Transmission Electron Microscopy and Scanning Tunneling Microscopy.   In addition, some Scanning Electron Microscopy was carried out for some macroscopic characterisations of film morphology.   However, it is unsuitable for most samples examined, due to both sample requirements, and range of magnification available.

Transmission Electron Microscopy

All Transmission Electron Microscopy (TEM) was done on formvar coated copper grids, and holey carbon grids. The TEM used was a Hitachi H7000 (Figure 3.10), capable of magnification up to 600K.
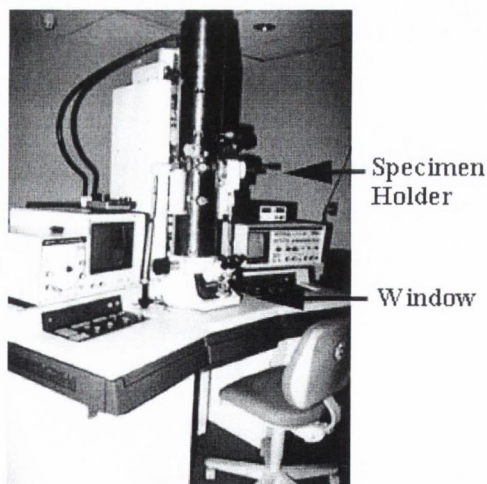
Figure 3.10 Hitachi H7000 Electron Microscope.

The accelerating voltage used was typically 100keV. All MWNT images were taken on photographic film, nearly SWNT composite images were taken using a recently

acquired CCD system within the chamber. The CCD has the advantage of being much more sensitive, and higher magnification images can therefore be observed.

Samples were prepared by two methods, either dipping the grids into the solution, or using a pipette to drop some of the solution onto the grids. Much of the difficulty with TEM of composite samples is the low transparency of the polymer, making it difficult to see nanotubes. Dropping tends to leave a uniform relatively dark film, against which there is little contrast with the nanotubes. Dipping the grids incompletely works well, as there is a gradient of film thickness. Much of it is sufficiently thin to be transparent to the electron beam. In particular, due to the rigidity of MWNT, it is relatively easy to find MWNT protruding from the film. SWNT are more difficult to locate, as they are highly flexible, but usually can be found at tears in the film, or sometime protruding from film edges. Tears in the film can be easily induced by stretching or bending the grids with a tweezers. For pure nanotube samples, which are insoluble, samples were prepared by briefly sonicating the nanotubes in ethanol or chloroform, and dropping this suspension onto the copper grids. This works well for pure nanotube samples, giving a dispersed film of nanotubes and nanotube aggregates.

Scanning Tunneling Microscopy/Spectroscopy

All STM was done on a substrate of Highly Ordered Pyrolytic Graphite (HOPG). For the composite samples, the composite was diluted heavily with toluene, to minimise PmPV film thickness. This dilute solution was then dropped onto HOPG, and again allowed to dry. The films were then transferred into the ultra high vacuum ($< 10^{-9}$ Torr) STM (RHK Technology). A similar technique is used for STM on pure PmPV samples. Films were imaged using mechanically formed Platinum-Iridium tips.

Atomic resolution on the HOPG was used as a gauge of tip quality as well as a calibration for x-y piezos. The topographic images were obtained in constant current mode with a scan rate of approximately 60 ms/point. Tunneling setpoints were typically 10s of pA and 100s of mV.

3.3.2 Optical Spectroscopy

All optical spectroscopy was carried out by measuring the spectrum of the composite and a pure polymer solution of the same concentration as a reference. For solid-state measurements requiring a pure nanotube reference as well, an unstable suspension of nanotubes in chloroform or toluene was used after sonication, and before the bulk of the nanotubes had precipitated. Fluorescence measurements were carried out with a Perkin Elmer LS50B Luminescence Spectrometer. UV-Visible absorption measurements were carried out using a Shimadzu UV1601-PC Spectrophotometer. All fluorescence was carried out in solution, using 1mm glass or quartz cuvettes. Absorption measurements were carried out in solid state, for examination of the higher energy absorption (4-7eV). For these measurements, the solutions were spuncoat onto Spectrosil B 15mm disks using a Convac 1001 spincoater. Typically up to 10 layers were put down in order to achieve sufficient thickness for a strong absorption spectrum. Previous characterisation[18] has shown that despite the inhomogeneity in the composite solutions, spincoating is effective, and does not affect the concentration of nanotubes in the composite. There are differences between spectra of polymers in the solid state and in solution; peaks are generally redshifted and broader in solution due to the higher mobility, lower interchain interactions, and greater range of orientations possible.

3.3.3 Vibrational Spectroscopy

Raman spectroscopy was carried out on an Instruments S.A. Labram 1B in reflectance mode. Samples were dropcast onto a glass microscope slide. Dropcasting was advantageous for these experiments, as the film encompasses a wide range of thicknesses, so an optimal thickness in the film is relatively easy to locate. Nanotube measurements were carried out on the raw powder. Both Helium-Neon (632.8nm, 11mW) and Argon ion (514.5nm, 50mW) are available as sources.

3.4 Conclusions

This chapter has described the experimental techniques used in the course of this study, both to produce materials and to prepare samples for examination. In Section 3.2, synthesis of the materials studied is described. This covers three sections; synthesis of the conjugated polymer, PmPV, production methods for the carbon nanotubes used in this study, and the techniques used to combine these two components into successful composites. Section 3.3 summarises the various experimental techniques used to prepare samples for easy examination. These have been optimised by trial and error over the course of this study, and the optimal methods are outlined here.

References

[1] S. Maier, Diploma Arbeit Thesis, Trinity College Dublin (1997).

[2] M. in het Panhuis, R.W. Munn, W.J. Blau, Proceedings of the International Conference on the Science and Technology of Synthetic Metals, Austria, 2000, to be published in *Synthetic Metals*.

[3] S. Iijima, *Nature*, **354**, 56 (1991).

[4] R. Bacon, *J. Appl. Phys.*, **31**, 283 (1960).

[5] H. W. Kroto, J. R. Heath, S. C. O'Brien, R. F. Curl, R. E. Smalley, *Nature*, **318**, 162 (1985).

[6] W. Krätschmer, L.D. Lamb, K. Fostiropoulos D.R. Huffman, *Nature*, **347**, 354 (1990).

[7] T.W. Ebbesen, P.M. Ajayan, Nature, **358**, 220 (1992).

[8] C. Journet, W.K. Maser, P. Bernier, A. Loiseau, M. Lamy de la Chapelle, S. Lefrant, P. Deniard, R. Lee, J.E. Fischer, *Nature*, **388**, 756 (1997).

[9] B. Lahr *et al.*, unpublished results.

[10] S. Iijima, T. Ichihashi, *Nature*, **363**, 603 (1993).

[11] D. S. Bethune, C. H. Kiang, M. S. de Vries, G. Gorman, R. Savoy, J. Vasquez, R. Beyers, *Nature*, **363**, 605 (1993).

[12] A. Thess, R. Lee, P. Nikolaev, H. Dai, P. Petit, J. Robert, Y. H. Lee, A. G. Rinzler, D.T. Colbert, D. Tománek, J. E. Fischer, R. E. Smalley, *Science*, **273**, 483 (1996).

[13] A. Fonseca, K. Hernadi, P. Piedigrosso, J.-F. Colomer, K. Mukhopadhyay, R. Doome, S. Lazarescu, L. P. Biro, Ph. Lambin, P. A. Thiry, D. Bernaerts, J. B.Nagy, *Appl. Phys. A*, **67**, 11 (1998).

[14] D. Bernaerts, X.B. Zhang, X.F. Zhang, S. Amelinckx, G. van Tendeloo, J. van Landuyt, V. Ivanov, J. B.Nagy, *Philos. Mag.*, **71**, 605 (1995).

[15] J. N. Coleman, D.F. O'Brien, A.B. Dalton, B. Mc Carthy, B. Lahr, A. Drury, R.C. Barklie, W.J. Blau, *Chem. Comm.*, 2001 (2000).

[16] A.B Dalton, PhD. Thesis, Trinity College Dublin (1999).

[17] S. Curran, P. M. Ajayan, W. Blau, D. L. Carroll, J. N. Coleman, A.B. Dalton, A.P. Davey, A. Drury, B. McCarthy, S. Maier, A. Strevens, *Adv. Mat.*, **10,** 1091 (1998).

[18] J.N. Coleman, PhD. Thesis, Trinity College Dublin (1999).

Chapter 4

Review of Research on PmPV/Nanotube Composites

4.1 Introduction

Nanotubes have generated much interest since their discovery in 1991[1]. Initially most work on nanotubes concentrated on characterising their unique properties. In recent years, as these properties have been better understood, the emphasis has shifted towards developing applications for these materials. Proposed applications have been diverse, ranging from biosensors[2] to molecular diodes[3, 4], templates for assemblies of nanowires[5] to reinforcement for plastics and epoxy resins[6]. Nanotubes have been shown to have potential for all these ideas, but there still are several problems hindering realisation of these applications on a commercial scale. One is the problem of reliably and economically manipulating of nanoscale size, which is a limitation of current technology. A further problem is economic production in large quantities of pure nanotube samples. As a means of avoiding and overcoming these problems, research in recent years has examined the idea of composites based on carbon

nanotubes[6,7]. These have used carbon nanotubes as bulk mechanical reinforcement in commercial polymers, and thus are not substantially hindered by purity of nanotube samples. Impurities in nanotube samples are disadvantageous, but high purity samples are not critical.

Further problems with using nanotubes as mechanical reinforcement of non-interacting commercial polymers have been noted[6]. These problems include nanotube aggregation, and the lack of a strong polymer-nanotube interaction. The strong propensity of nanotubes to aggregate means that they tend not to be well dispersed throughout the sample, leaving weak points at which these composites can fracture, and also dramatically limits the surface area between the polymer and nanotubes. Furthermore, the lack of strong interfacial binding between the two components limits the reinforcement, as the nanotubes can readily slip through the holding matrix as force is applied.

Research in Trinity has focussed also on composites of polymers and nanotubes. The polymer used is a functional organic polymer, poly(m-phenylenevinylene-co-2,5-dioctyloxy-p-phenylenevinylene), or PmPV[8]. This has several substantial advantages over other composites developed. The polymer is a poly(phenylene-vinylene), PPV, derivative, a conjugated electronically active polymer notable for its use in organic LEDs[9]. As will be presented here, it has a strong interaction with nanotubes, so the lack of interfacial binding that is problematic with some other polymers is not a problem here. Furthermore, as will be reviewed in this chapter, it has been shown that during the composite formation, the nanotube aggregates are broken up, and the polymer coating hinders their re-aggregation. This interaction has several interesting properties. It binds to the lattice structure of the nanotubes, and as PmPV is soluble in

many organic solvents, unlike the pure nanotubes themselves, stable solutions of these composites are readily attainable. This also allows the preferential selection of nanotubes from the raw nanotube powder, giving a previously unachieved method of both purifying and characterising raw nanotube powder. Raman studies indicate that the PmPV interacts preferentially with particular diameters of single-walled nanotubes, suggesting the possibility of a technique to preferentially select nanotubes of a particular diameter. As PmPV is both optically and electronically active, these composites, as the active layer in organic devices such as LEDs and field effect transistors, could have greatly enhanced stability and transport properties as compared to the pure polymer.

4.2 Research in Trinity

In this section, research of relevance to the present study will be reviewed. In Section 4.2.1, theoretical modelling of the structure of PmPV will be reviewed, as this is greatly beneficial in understanding later observations. Some notable aspects of the characterisation of PmPV/nanotube composites will also be summarised. This includes the utilisation of the PmPV-nanotube binding process to purify raw Krätschmer MWNT powder by selectively suspending and filtering multi-walled nanotubes. Indications that the binding process, in the case of SWNT, is dependent on the diameter of the nanotube, have implications for the present study, and will be reviewed here. To conclude this chapter, investigations underway to examine potential applications will be summarised.

4.2.1 Theoretical Modelling of PmPV Structure

Figure 4.1 gives the chemical structure of PmPV. It differs from the standard PmPV, in that there are alternating *para-meta* linkages along the polymer backbone. This has

the effect of slightly interrupting the conjugation, resulting in decreased electron delocalisation, and therefore a blueshifted emission spectrum. The introduction of *meta* linkages are also expected to assist in achieving high solid state luminescence efficiency by limiting the amount of interchain interaction, thus reducing aggregation and the associated detrimental effects on the optical properties. The dioctyloxy sidegroups have the effect of making this polymer soluble, and therefore easing processing and device applications[10]. Without sidegroups, PmPV is not soluble, and has to be polymerised *in situ* from films of the precursor.
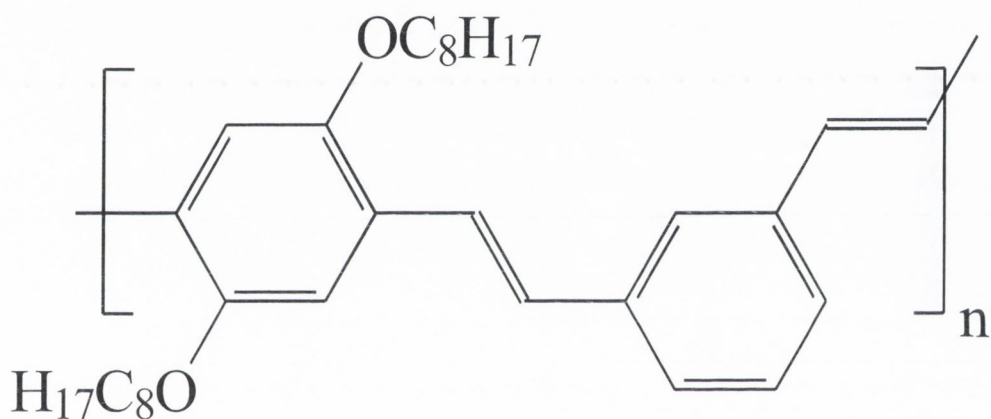
Figure 4.1 Chemical Structure of PmPV.

Sidegroups do also have significant effects on the morphology of PmPV, by altering backbone conformation, and thus the capability of the polymer strands to interact with each other. For example, PPV with octyloxy side groups is semi-crystalline at about 20% crystallinity, while PPV with 4-phenoxyphenyl sidegroups is totally amorphous[11]. This is also demonstrated in waveguide investigations, as PmPV with octyloxy sidegroups has little potential due to high scattering from crystalline regions, as compared to PmPV with methoxy sidegroups, which has lower scattering due to a more amorphous nature[12]. X ray diffraction studies have attributed this to the methoxy sidegroups inhibiting the formation of a planar backbone[13].

The effect of the sidegroups also has implications for the formation of stable PmPV/nanotube composites. PmPV with dioctyloxy sidegroups is the only polymer found to hold nanotubes in solution, despite a range of polymers investigated. Even an extremely similar polymer, such as PmPV with one octyloxy group replaced by a methoxy group does not hold nanotubes in solution.

The reasons for this are not fully understood yet, but there is much that can be said about the necessary polymer conformation to hold nanotubes in solution.

(a)   (b)
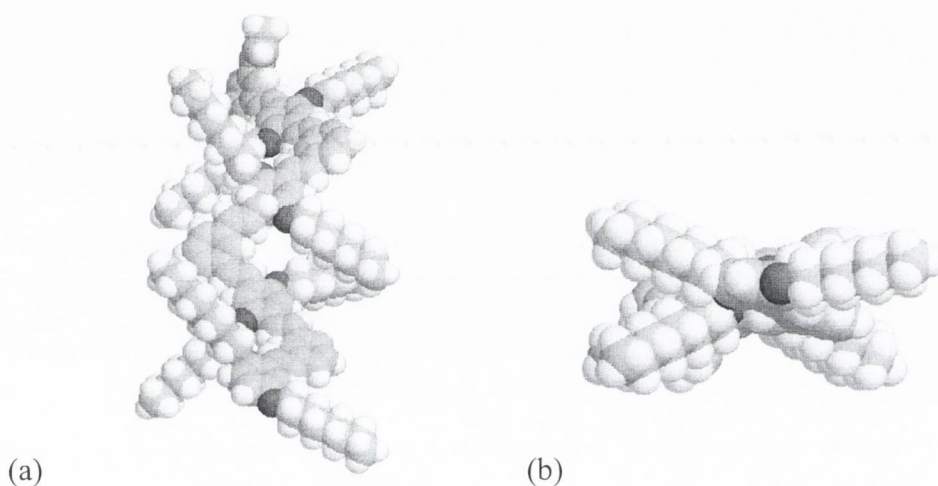
Figure 4.2 Optimised geometry of all-trans PmPV polymer (4 repeat units). top and (b) side view. Carbon, hydrogen and oxygen atoms are shown in grey, white and black, respectively.

Figure 4.2 shows a geometry-optimised model of an all *trans* dioctyloxy PmPV[14]. The backbone reorganises into a relatively flat zigzag structure due to *meta* phenylene linkage and van der Waals interactions between the octyloxy groups. There is also a slight but noticeable helicity to the backbone. The van der Waals interaction between the sidegroups keeps them relatively planar, and exposes the polymer backbone, as can be seen in Figure 4.2 (b). Contrast this with Figure 4.3, a geometry optimised model of the same PmPV, but with one octyloxy sidegroup replaced by a methoxy sidegroup, a polymer that has been found not to keep nanotubes in solution.
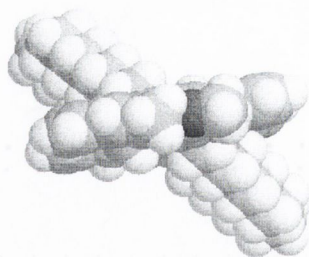
Figure 4.3 Side view of optimised geometry of all-trans PmPV polymer.
(Four repeat units, with one octyloxy group replaced by methoxy group).

It can be seen that the sidegroups are not as co-planar with the PmPV backbone as the previous example. This is due to the lessened effect of sidegroup interactions. Consequently, the backbone of the polymer is less exposed. It appears that an exposed planar backbone is necessary for polymer/nanotube binding. This suggestion is further strengthened by an examination by A.B. Dalton of dioctyloxy PmPV produced by different synthesis routes[15]. This found that dioctyloxy PmPV made by one particular synthesis route, the Wittig reaction, does not interact with nanotubes. FTIR analysis shows that this PmPV differs by having a much higher proportion of *cis* linkages on the vinylene bond. This affects the polymer structure by disrupting the planar nature of the backbone, and reducing the order in the polymer structure. The optimised geometry of this all-*cis* PmPV is shown in Figure 4.4. The backbone reorganises into a non-exposed non-regular helical structure with solubilising sidegroups pointing upwards and outwards. Thus, this structure is missing the planar exposed backbone of the all-*trans* PmPV, and this explains the difference in nanotube interactions between these two conformations.
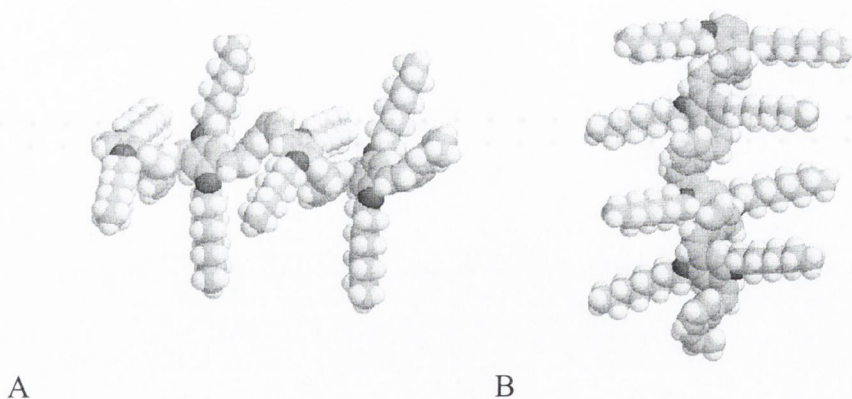
Figure 4.4 Optimised geometry of all-cis PmPV polymer (4 repeat units).

This planar and exposed backbone conformation explains the crystalline nature of dioctyloxy PmPV. X-Ray crystallographic studies of a similar all-*trans* PPV oligomer shows that the crystalline structure consists of parallel strands at an angle to the crystal axis, separated in plane by the long sidegroups, and vertically by a distance of 3.77Å[16]. The PmPV backbones are separated in plane by a distance of 16Å due to the extended sidegroups[11]. The exposed backbone conformation that allows the polymer to interact with itself in an ordered way is also hypothesised to allow the polymer to interact with carbon nanotubes and bind to them.

4.2.2 Purification of Raw Multi-Walled Nanotube Powder[17]

Initial work on the purification abilities of the composite concentrated on characterising the phase separation effects of the composite, the preferential selection and suspension of nanotubes. This was first suggested by a TEM image taken by Professor Ajayan of Rensselaer Polytechnic Institute, showing nanotubes coated in PmPV protruding from the edge of a composite film[18] (Figure 4.5).

Figure 4.5 TEM image of PmPV/MWNT Composite.

The PmPV film can be clearly seen to wet all the nanotubes protruding from the composite film. There are no graphitic impurities visible, despite the raw powder from which this composite is formed being about 75% graphitic particles. These particles are usually seen attached to the walls of nanotubes, suggesting that the PmPV coating the nanotube in some way displaces the graphitic particles from the nanotube. The PmPV thus acts as a filtering system, removing the nanotubes from the accompanying graphitic particles.

To investigate the purification effect of the composites, Dr. S. Curran of Trinity College carried out initial Raman studies[19]. The Raman spectrum of raw powder is shown in Figure 4.6. The broad feature at $1350cm^{-1}$ is arises mainly from graphitic carbon particles, with some contribution from defect sites and tips of nanotubes. The peak at 1580^{-1} is assigned to the E_{2g} mode of multi-walled carbon nanotubes, arising from the ordered graphitic lattice structure of the nanotube. Thus, the relative

intensities of these two peaks can be used to give some indication of the purity of a nanotube sample. This is not exact, as the nanotubes contribute to both peaks, and this contribution varies from sample to sample. Here, as we are comparing the same nanotube samples, this is not a problem.
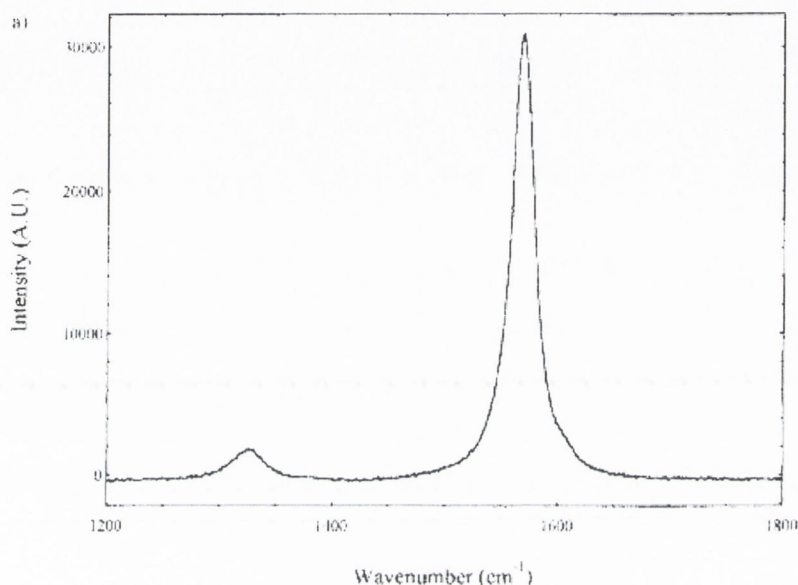
Figure 4.6 Raman Spectra of raw nanotube powder.

Comparing Figure 4.6 to Figure 4.7, the Raman spectrum of the composite material, it can be clearly seen that there is a change in the relative peak heights. The 1350cm^{-1} line, prominent in the raw sample, is significantly reduced in the composite. It appears as a minor bump above the broad background. This gives some confirmation to the hypothesis of sample purification by preferential polymer interaction.

This preferential suspension of nanotubes was further investigated by Dr. J. Coleman using electron paramagnetic resonance[20] (EPR). EPR is a very useful method for characterising nanotube samples. It measures the absorption of microwaves by a sample in the presence of a magnetic field. Transitions are induced for unpaired electrons between the m_s=1/2 and m_s=-1/2 states, which split due to the magnetic

field. Unpaired electrons in different environments may be distinguished using this technique by differences in their resonance spectra.
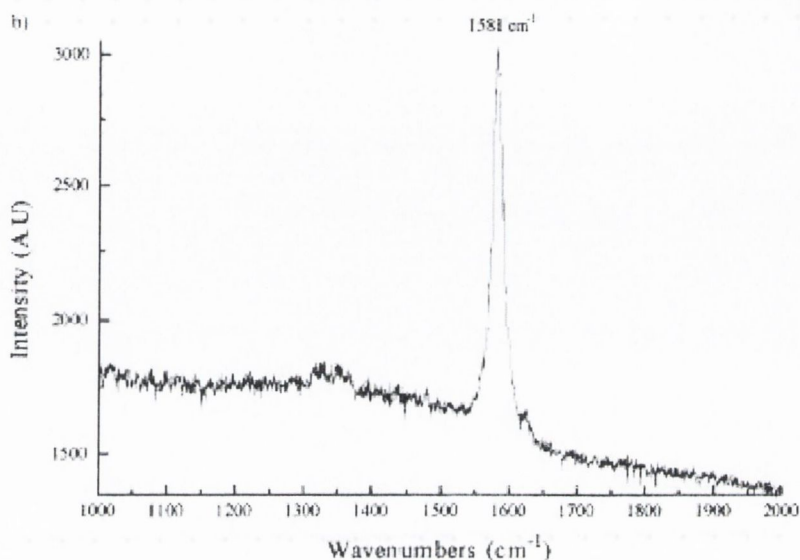
Figure 4.7 Raman Spectra of Composite.

The local environment of unpaired electrons of a MWNT differ strongly from that of turbostratic graphite (TSG), and this is reflected in both the position and the width of the absorption peak. For MWNT electrons, the Lorentzian linewidth is approximately 10G, and the g_0 value (a experiment independent parameter describing the position of absorption) is approx 2.01. For an unpaired electron of TSG, the values are 15g and 2.02 respectively. Thus, EPR makes it a simple matter to investigate relative changes in the raw nanotube samples due to the effects of the PmPV.

To characterise the effects of the PmPV, Dr. Coleman prepared a composite solution (10% mass fraction nanotubes, 20g PmPV/L in toluene). After allowing this to settle for a week, this was decanted, giving a solute, that which was kept in solution, and a precipitate, which had fallen out of solution. EPR was then used to investigate these samples. The results are shown in Figure 4.8. It can be seen that the solute is highly symmetrical, indicating a one-phase system, i.e. one of the parts of the raw powder

(MWNT and TSG) has precipitated completely. The g-values and widths of the absorption lines for these two fractions agree well with expected values for MWNT, indicating that it is the MWNT that remain in solution, whereas the TSG precipitates completely. The TSG absorption line is dominant in the precipitate, that taken from the bottom of the solution. Finally, to show that the polymer interaction was responsible for this suspension, and it was not due to other effects, such as viscosity or buoyancy, this was repeated with a non-interacting polymer, polystyrene. This showed that all powder had precipitated, with none left in the top fraction, and the bottom fraction's spectrum being similar to that of the raw powder.
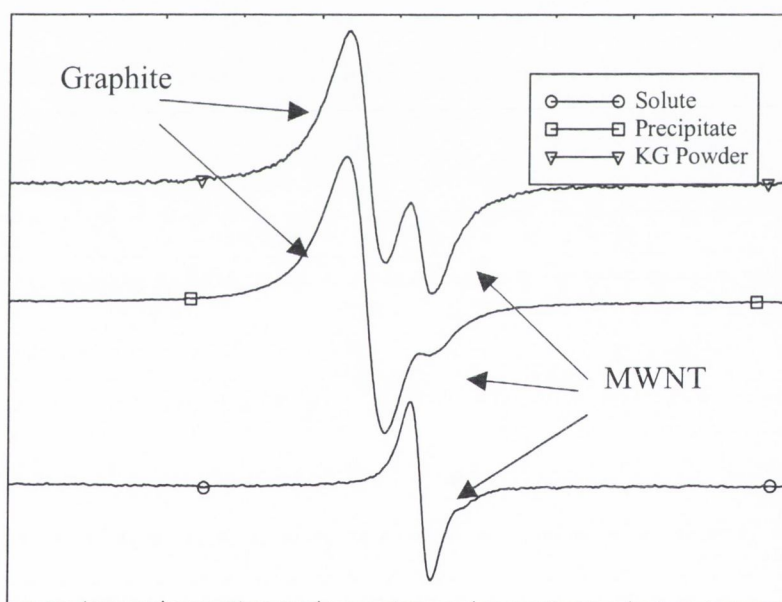
Figure 4.8 EPR spectra of different composite fractions and raw nanotubes. From top to bottom the graphs show the raw powder, the precipitate, and the solute respectively.

4.2.3 Quantification of Sample Purity

In the previous section, it was shown that EPR could easily distinguish between MWNT and TSG. This has been further extended to determine the mass of each component that contributes to the signal[20]. The signal intensities of each line can be measured, and this is proportional to the mass of the component that gives rise to this line. By assuming that the measured sample is representative of the total fraction, the measured intensity can be normalised to be representative of the total sample. This is done by multiplying the measured signal intensity by a factor of M_T/M_{EPR} where M_T is the total sediment or solute mass and M_{EPR} is the mass of the sample measured, yielding a normalised signal intensity (NSI).

These NSI are presented in Figure 4.9 for samples allowed to settle for different amounts of times. It can be seen that the TSG impurities fall out rapidly once the solution is allowed to settle. The majority has fallen out within approximately six hours, and after 48 hours, there is practically none left. This is in sharp contrast to the MWNT, which show no change over 96 hours.

The percentage of either component that remains in solution can be quantified by noting that the total signal intensity of solute and sediment will be constant over time. Therefore, for a given component at a given time, the percentage (P) that is in solution is given by:

$$P = 100 \times \frac{NSI_{solution}}{NSI_{solution} + NSI_{sediment}}$$

Equation 4.1

where $NSI_{solution}$ and $NSI_{sediment}$ are the normalized signal intensities for the same species in solution and sediment respectively.

So for example, after 48 hours $NSI_{solution}(MWNT) = 4.5$ while $NSI_{sediment}(MWNT) = 2.6$ (in arbitrary units). By comparison for the same sample $NSI_{solution}(TSG) = 0.5$ while $NSI_{sediment}(TSG) = 26.5$. Using this we can calculate that 63% of the added nanotubes go into solution while only 1.9% of the added TSG remains in solution.
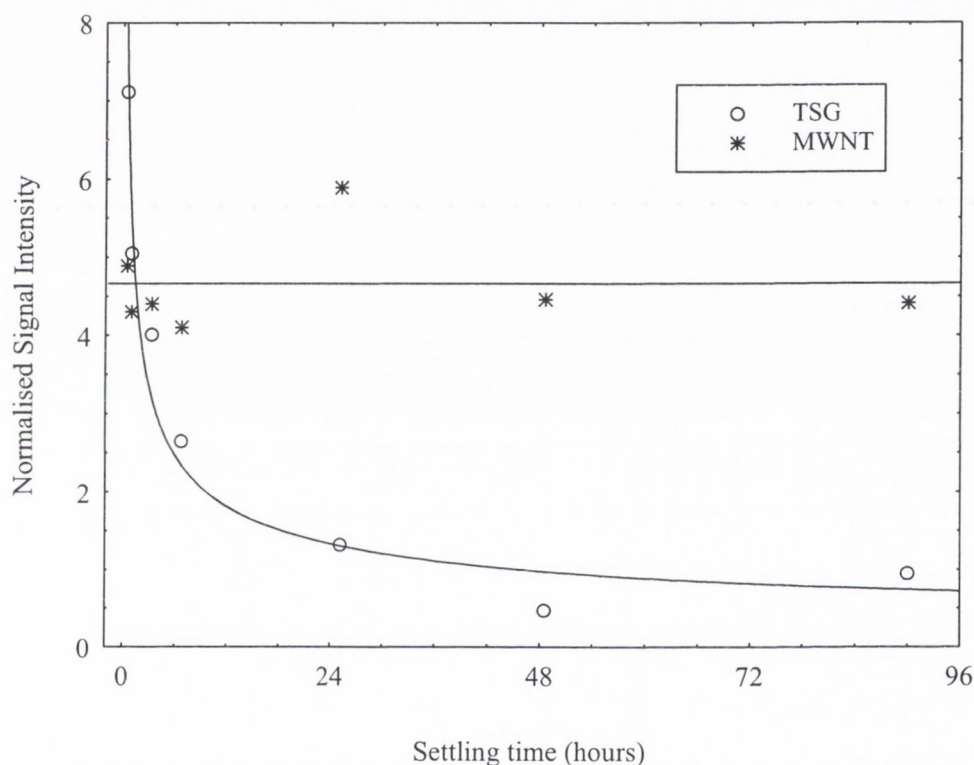
Figure 4.9 NSIs for nanotube and TSG components for various settling times. These NSIs are proportional to the entire mass of each component for each solute. Note that while the nanotube component remains approximately constant the turbostratic graphite component decreases as the TSG falls out of solution.

This technique is extremely useful, as it allows the relative change in the composite over time to be characterised. However, EPR alone does not give enough information to quantify the actual mass of each component in the composite. This is because further information is needed to determine the proportionality of NSI to mass, and thus allow a given NSI to be related back to mass of component giving that signal. In

order to do this we need to be able to calculate a nanotube signal intensity per unit mass, k, such that we can write an equation of the form;

$$S_i = k_i \, m_i \qquad\qquad\qquad \textit{Equation 4.2}$$

This is done by thermogravimetric analysis, TGA. This relatively simple technique monitors the mass of a sample as a function of temperature. TGA curves for raw nanotube powder, a well-settled composite and PmPV are shown in Figure 4.10. Note that all the PmPV bar some impurities is oxidised by 650°C, whereas the powder only begins to oxidise at 700 °C. Thus, a well-settled composite between these temperatures will consist only of nanotubes and some PmPV impurities.
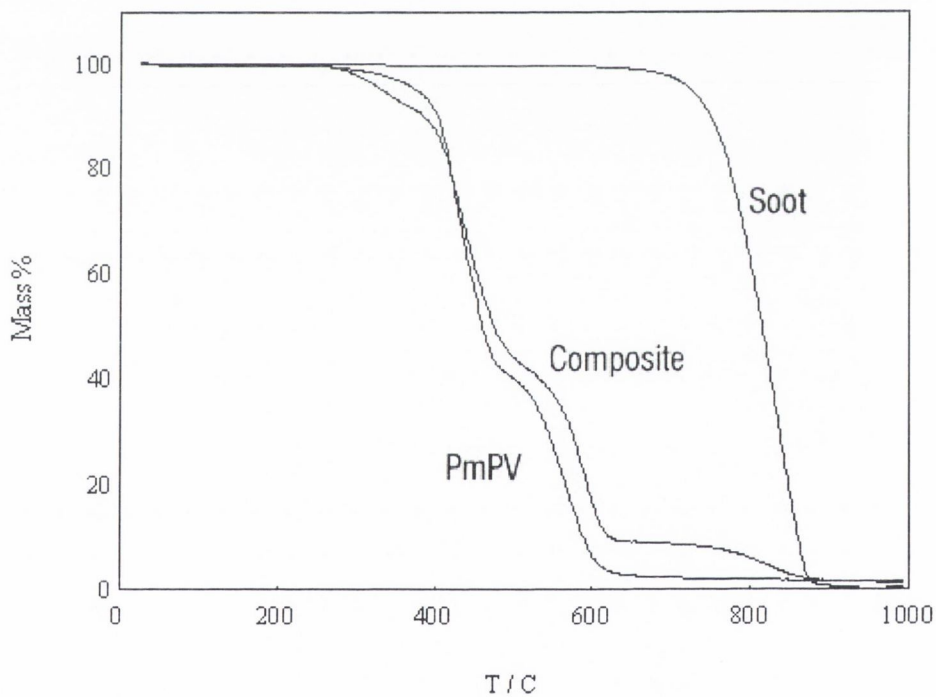
Figure 4.10 Thermogravimetric analysis of Composite, PmPV and MWNT.
Note that PmPV stops burning at approximately 600°C while the Carbon soot only begins to burn at 750°C. In the case of the composite sample, there is no oxidisation between these temperatures. This allows us to calculate the mass of nanotubes in this sample.

The polymer impurities can be accounted for by comparison with the TGA spectrum of pure PmPV, and so the mass of nanotubes in the composite can be calculated. In

the case of the composite solute measured here the nanotube mass was calculated at 5.1% of the total composite mass. This allows us to calculate the actual mass of nanotubes present in the (same) sample measured by EPR. As we know the nanotube EPR signal intensity (S_n) for this sample, we can calculate a signal intensity per mass of nanotubes, k_n. This works out to be 1.04/mg.

From this the mass of nanotubes in the raw soot can be calculated. For 1.5mg of soot dispersed in toluene, the NSI is measured as 0.53, and so the mass of nanotubes is $0.53/1.04$ mg^{-1}= 0.51 mg. This gives us a fully quantitative method of calculating the nanotube component of raw powder, which is in this case 34%.

Thus, by using the composite to selectively select nanotubes, and using EPR and TGA, it is possible to purify nanotube samples, and quantify these samples. This quantification is much improved on previous methods, which depended on visual observations by electron microscopy, or Raman spectroscopy, where there is some ambiguity about peak assignation.

4.2.4 Size Selection

The previous section reviewed multi-walled nanotube composites, showing how they can be used to facilitate both characterisation and purification of MWNT samples. Dr. A. Dalton (Trinity College, Dublin Institute of Technology) has characterised single-walled nanotube composites by Raman spectroscopy[21]. The same preferential selection of nanotubes is observed, but spectroscopy shows that the interaction seems to be selective, in that some nanotube diameters are preferentially suspended. Figure 4.11 shows the absorption spectra of SWNT, and the SWNT/PmPV composite. These are broadly similar, showing three main features that dominate the spectrum, at 0.68, 1.2 and 1.7eV. The features at 0.68 and 1.2 eV have been assigned to band gap

95

transitions in semiconducting tubes, whereas the feature at 1.7 eV originates from metallic tubes[22]. The width of the features is due to the superposition of narrower absorption bands corresponding to individual nanotubes of different chiral indices and diameter. For the composite, all three features suffer modifications. The full width half maximum of the feature at 0.68 eV has decreased while the features at 1.2 and 1.7 eV appear to resolve into a number of distinct features. This indicates that not only are the SWNT being separated from each other and other amorphous carbon but there is also a change to the distribution of nanotubes from raw powder to composite.
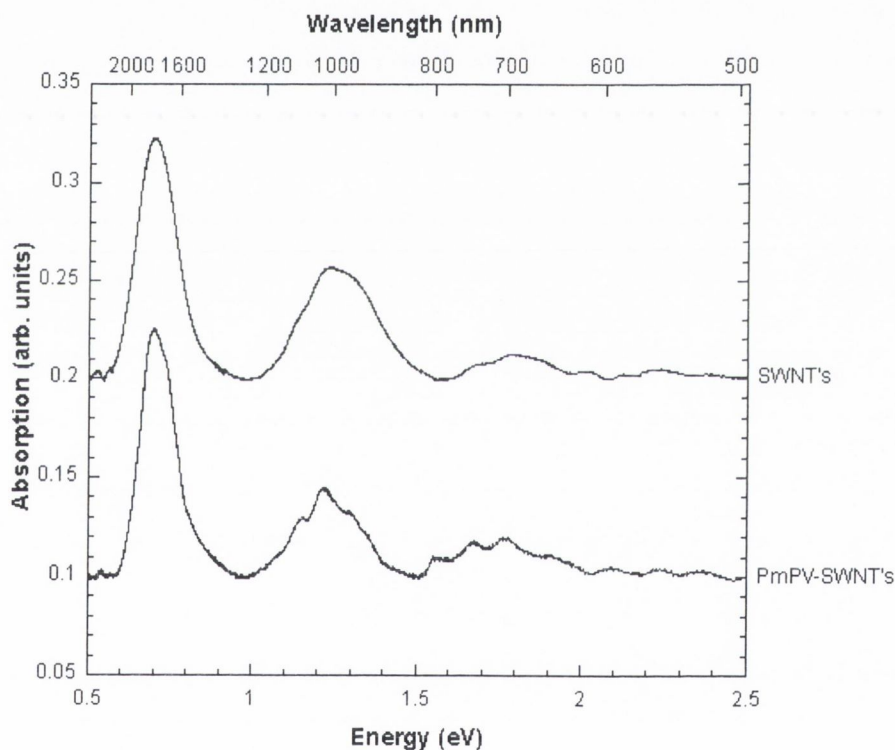
Figure 4.11 Absorption Spectra of SWNT, and SWNT/PmPV composite.

Raman Spectroscopy was used to investigate this further. Raman spectroscopy is an especially useful technique here, as it is sensitive to the radial breathing modes (RBM) of SWNTs, which are highly diameter dependent. The RBM region of the Raman spectra of SWNT composite and SWNT are shown in Figure 4.12 and Figure 4.13 respectively.
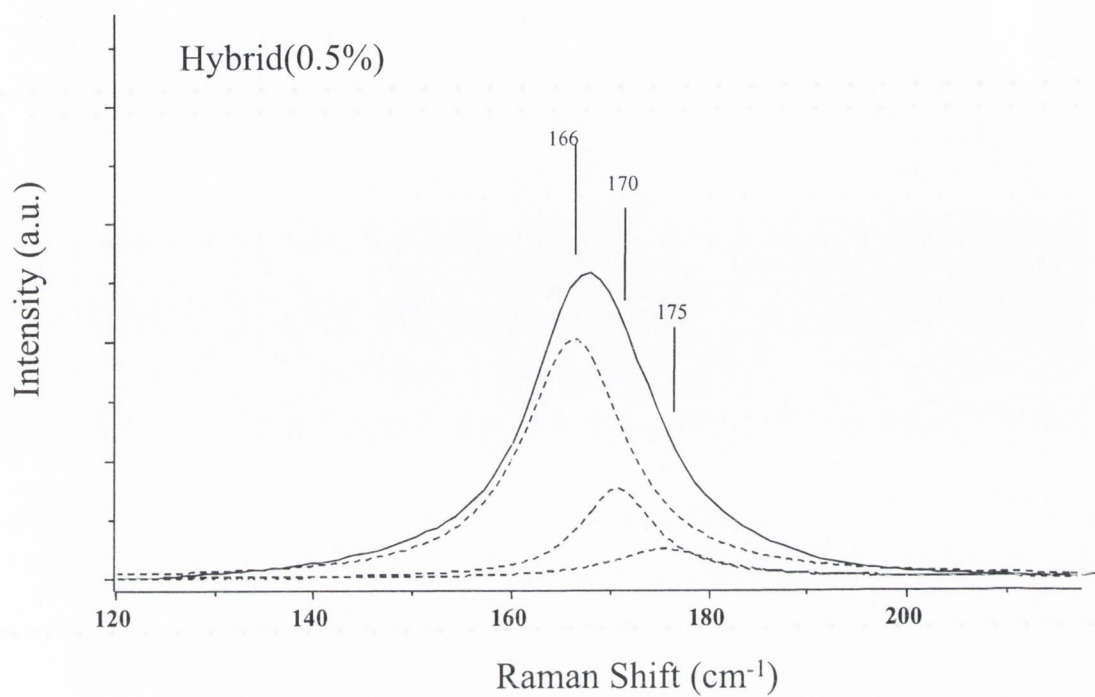
Figure 4.12 Raman Spectrum of the RBM region of the composite.
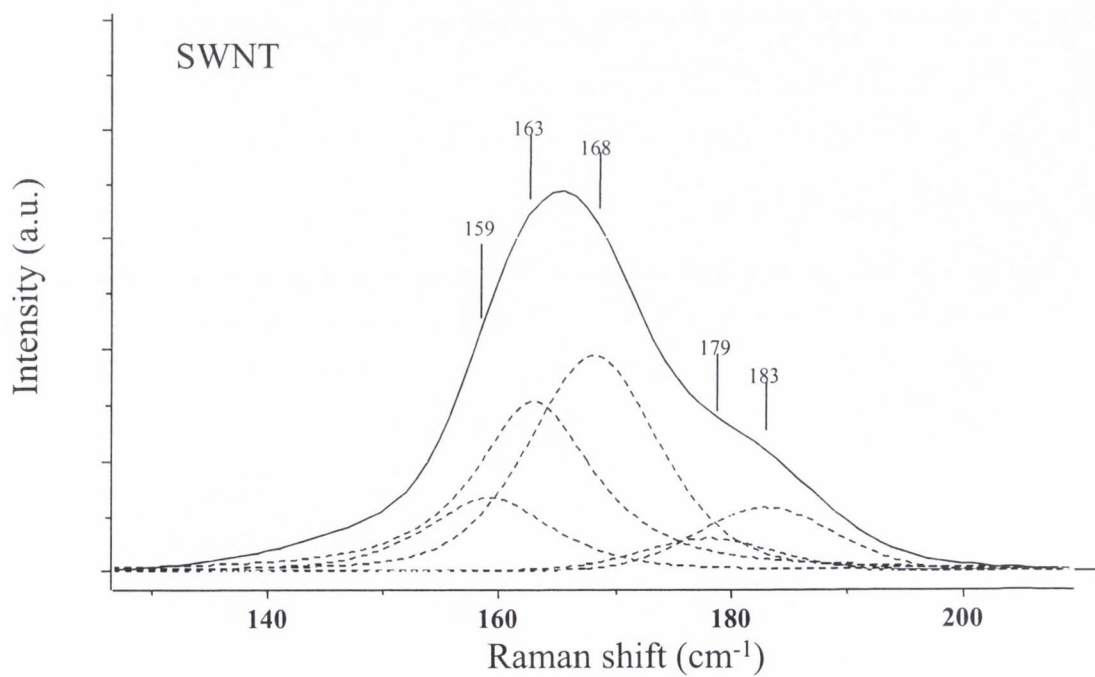
Figure 4.13 Raman Spectrum of the RBM region of the raw powder.

The raw powder is shown to have five components: 159, 163, 168, 179 and 183 cm^{-1}. The composite, in contrast, has three components centred at 166, 170 and 175 cm^{-1} respectively. It would appear that not only the frequency distribution of modes has changed but that the modes are being up-shifted by approximately 7 cm^{-1}.

Similar differences were found for excitations at other excitation wavelengths. One possible explanation is that the polymer interaction with nanotubes of small diameters is much less. As already mentioned, the low frequency part of the Raman spectra is very sensitive to the diameter of tubes and can thus be used as a probe of the size and polydispersivity of the SWNT. Rao et al established a linear dependence of the breathing mode frequency on the inverse of the tube diameter.[23] Recently, this has been amended to take into account the intertubule interaction within a bundle[24]:

$$\omega_r = \frac{223.75 cm^{-1}.nm}{d(nm)} + 14 cm^{-1}$$
<div align="right">Equation 4.3</div>

in which ω_r is the radial breathing mode frequency, d is the diameter, and the 14 cm^{-1} correction represents a diameter-independent approximation to the effect of the weak inter-tubule interaction.

1064 nm excitation

SWNT				Composite			
ω(cm^{-1})	γ(cm^{-1})	I(a.u)	δ(nm)	ω(cm^{-1})	γ(cm^{-1})	I(a.u)	δ(nm)
159	14	12	1.54	166	10	40	1.54
163	15	30	1.5	170	8	13	1.5
168	15	38	1.45	175	8	5	1.45
179	8	5	1.36				
183	14	12	1.32				

Table 4.1 Diameter distribution of SWNT in powder and composite form

Using this relationship, the diameter range of SWNT in our powder has been calculated and is summarised in Table 4.1. It is apparent that the frequency

distribution and relative mode intensity has changed for the composite compared to the SWNT powder.

This suggests that these modifications occur due to the polymer preferentially interacting with SWNT of certain diameters, leaving the remainder to precipitate from solution. There is also an indication that the polymer-tube system increases the frequency of the modes by 21 cm^{-1} compared to 14 cm^{-1} for tube-tube interactions. It should be noted that this effect is only observed at low concentrations, as at high concentrations, SWNT aggregate strongly, hindering PmPV-nanotube interactions, and thus this selection process.

4.2.5 Potential Applications of PmPV/Nanotube Composites

In addition to the very interesting features of these composites outlined in the previous sections, work has also focussed on potential device applications of these materials. PmPV is, as previously mentioned, an optically and electronically active polymer that has much potential for organic electronics[25]. It is expected that the introduction of nanotubes, whilst possibly having some adverse effects, should have potential for a range of organic devices. Work in Trinity has focussed on three possible device applications; composites as the active layer in LEDs (A. Strevens), as an electron transport layer in LEDs (P. Fournet), and organic heterojunctions (B. Kilbride). This research has only begun recently and is ongoing. One possible application that is showing much promise is using the composite as an electron transport layer. This will be reviewed here.

P. Fournet[26] has made a variety of LEDs, all with M3EH-PPV as the active optical material, and two hole transport layer (HTL) materials; PVK and poly-TPD-DPX, and a PmPV-MWNT composite as an electron transport layer (ETL) material. Use of the

PmPV/nanotube material as a HTL shows promise; the brightness of the devices increased significantly for all but the highest mass fraction composites, and the PVK/ M3EH-PPV/ PmPV-MWNT multiplayer device shows an order of magnitude increase in brightness compared with the single layer M3EH-PPV device. One drawback is that the applied voltage required to reach a threshold current is significantly higher with the composite. The brightness and applied voltage are shown as a function of nanotube mass fraction in Figure 4.14.
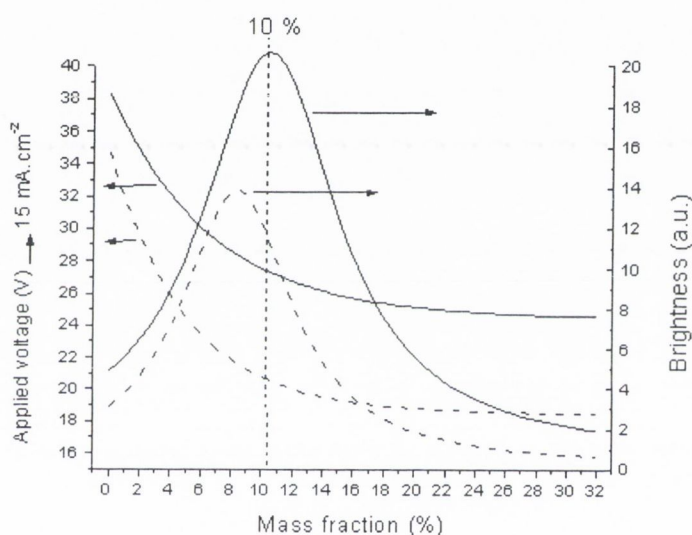
Figure 4.14 Brightness and voltage to reach 15 mA.cm^{-2} for different mass fractions. M3EH-PPV/comp. (dash lines) and PVK/M3EH-PPV/comp. (solid lines) devices

The electroluminescence spectra for this range of devices are shown in Figure 4.15. It can be seen that although the luminescence is much higher due to the composite, the shape is not changed, showing that the composite is acting only as an ETL.
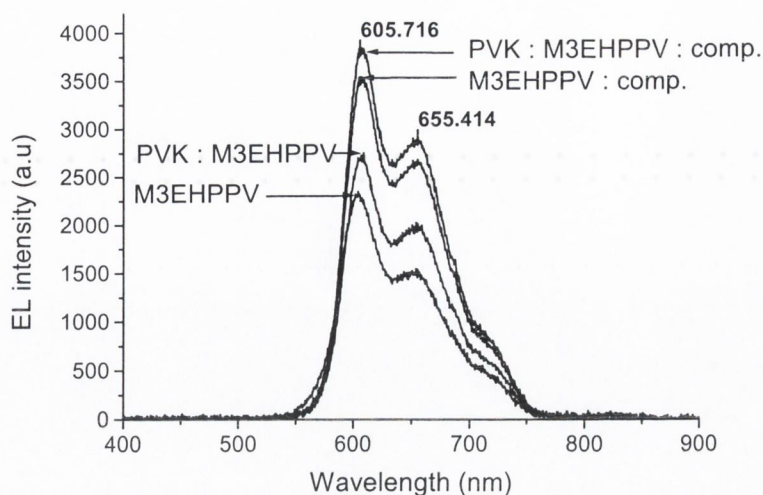
Figure 4.15 EL spectra for the SL, DL and TL devices at J = 15 mA.cm^{-2}.

4.3 Conclusions

In this chapter, several interesting aspects of PmPV/nanotube composite research have been presented. These serve to explain both the motivation for research on these particular composites, and the advantages of these composites. These are also of relevance for the presentation of results in later chapters. Section 4.2.1 reviews computational investigations of the structure of dioctyloxy PmPV, and how this relates to polymer morphology, and polymer-nanotube interactions. Sections 4.2.2 and 4.2.3, present evidence of how this polymer-nanotube interaction can be used to selectively hold nanotubes in suspension, and consequently purify and quantify raw Krätschmer multi-walled nanotube powder. Of further interest, is the demonstration of a diameter dependence of these interactions for single-walled carbon nanotube samples, presented in Section 4.2.4. Finally, to conclude this chapter, Section 4.2.5 describes some current investigations on potential applications of these materials.

References

[1] S. Iijima, *Nature*, **354**, 56 (1991).

[2] F. Balavoine, P. Schultz, C. Richard, V. Mallouh, T.W. Ebbesen, C. Mioskowski, *Angew. Chem. Int. Ed.* **38,** 1919 (2000).

[3] L. Chico, V.H. Crespi, L.X. Benedict, S.G. Louie, M.L. Cohen, *Phys. Rev. Lett.*, **76**, 971 (1996).

[4] P.G. Collins, A. Zettl, H. Bando, A. Thess, R.E. Smalley, *Science*, **278**, 100 (1997).

[5] S. Fullam, D. Cottell, H. Rensmo, D. Fitzmaurice, *Adv. Mater.*, **12**, 1430 (2000).

[6] P. M. Ajayan, L. S. Schadler, C. Giannaris, A. Rubio, *Adv. Mater.,* **12**, 750 (2000).

[7] C. Stephan, T.P. Nguyen, M. Lamy de la Chapelle, S. Lefrant, C. Journet, P. Bernier, *Synth. Met.,* **108**, 139 (2000).

[8] A.P. Davey, A. Drury, S. Maier, H.J. Byrne, W.J. Blau, *Synth. Met.*, **103**, 2478 (1999).

[9] J. J. Burroughs, D. D. C. Bradley, A. R. Brown, R. N. Marks, K. MacKay, R. H. Friend, P. L. Burn, A. B. Holmes, *Nature,* **347**, 539 (1990).

[10] D. Braun, A.J Heeger, *Appl. Phys. Lett.*, **58**, 1982 (1991).

[11] R. Resel, B. Tertinek, S. Tasch, A.P. Davey, W. Blau, H. Horhold, H. Rost, G. Leising, *Synth. Met.*, **101**, 96 (1999).

[12] S.M. Lipson, private communication.

[13] J.H.F. Martens, E.A. Marseglia, D.D.C. Bradley, R.H. Friend, P.L. Burn, A.B. Holmes, *Synth. Met.,* **55**, (1993).

[14] M. in het Panhuis, R.W. Munn, W.J. Blau, *Proceedings of the International Conference on the Science and Technology of Synthetic Metals*, Austria, 2000, to be published in *Synthetic Metals*.

[15] A.B. Dalton, Ph.D. Thesis, Trinity College Dublin, (1999).

[16] R.E. Gill, A. Meetsma, G. Hadziioannou, *Adv. Mater.*, **8**, 212 (1996).

[17] J. N. Coleman, A. B. Dalton, S. Curran, A. Rubio, A. P. Davey, A. Drury, B. McCarthy, B. Lahr, P. M. Ajayan, S. Roth, R. C. Barklie, W. J. Blau, *Adv. Mat.*, **12**, 213 (2000).

[18] S.A. Curran, P.M. Ajayan, W.J. Blau, D.L. Carroll, J.N. Coleman, A.B. Dalton, A.P. Davey, A. Drury, B. Mc Carthy, S. Maier, A. Strevens, *Adv. Mater.*, **10**, 1091 (1998).

[19] J. N. Coleman, A. B. Dalton, S. Curran, A. Rubio, A. P. Davey, A. Drury, B. Mc Carthy, B. Lahr, S. Roth, R. C. Barklie, W. J. Blau, *Adv. Mater.*, **12**, 213 (2000).

[20] J. N. Coleman, D.F. O'Brien, A.B. Dalton, B. Mc Carthy, B. Lahr, A. Drury, R.C. Barklie, W.J. Blau, *Chem. Comm.*, 2001 (2000).

[21] A.B. Dalton C. Stephan, J. N. Coleman, B. McCarthy, P. M. Ajayan, S. Lefrant, P. Bernier, W. J. Blau, H.J. Byrne, *J. Chem. Phys. B*, **104**, 10012 (2000).

[22] H. Kataura, Y. Kumazawa, Y. Maniwa, I. Umezu, S. Suzuki, Y. Ohtsuka, Y. Achiba, *Synth. Met.*, **103**, 2555 (1999).

[23] A. M. Rao, S. Bandow, E. Richter, P. C. Eklund, *Thin Solid Films*, **331**, 141 (1998).

[24] U. D. Venkateswaran, A. M. Rao, E. Richter, M. Menon, A. Rinzler, R. E. Smalley, P. C. Eklund, *Phys. Rev. B*, **59**, 10928 (1999).

[25] R.H. Friend, R. W. Gymer, A. B. Holmes, J. H. Burroughes, R. N. Marks, C. Taliani, D. D. C. Bradley, D. A. Dos Santos, J. L. Brédas, M. Lögdlund & W. R. Salaneck, *Nature*, **397,** 121 (1999).

[26] P. Fournet, D.F. O' Brien, J.N. Coleman, H.H. Hörhold, W.J. Blau, *Proceedings of the International Conference on the Science and Technology of Synthetic Metals*, Austria, 2000, to be published in *Synthetic Metals*.

Chapter 5

Electron Microscopy of PmPV/Nanotube Composites

5.1 Introduction

In this chapter, a review of the Transmission Electron Microscopy studies carried out during the course of this thesis will be presented. Initially, a brief TEM characterisation of the nanotube samples will be presented to give an idea of the morphology of the nanotube samples that were used. This is followed by a study of the composite systems in more detail, including a general overview, and an examination of the interesting features of these composites.

5.2 Characterisation of Nanotube Samples

As explained in Chapter 3, three different nanotube samples were used in these studies. Arc Discharge Method multi-walled nanotubes (ADM MWNT) were made in Trinity. These tend to be easy to work with, as they are rigid due to the high number of shells, and do not aggregate as easily as the more flexible Catalytic

Decomposition of Acetylene multi-walled nanotubes (CDA MWNT), or the Arc Discharge Method single-walled nanotubes (SWNT). In addition, as seen in Chapter 4, the raw powder has a high yield of good quality nanotubes, which are purified further upon composite formation. A typical TEM image (magnification x20k) of a raw ADM MWNT powder sample is shown in Figure 5.1.
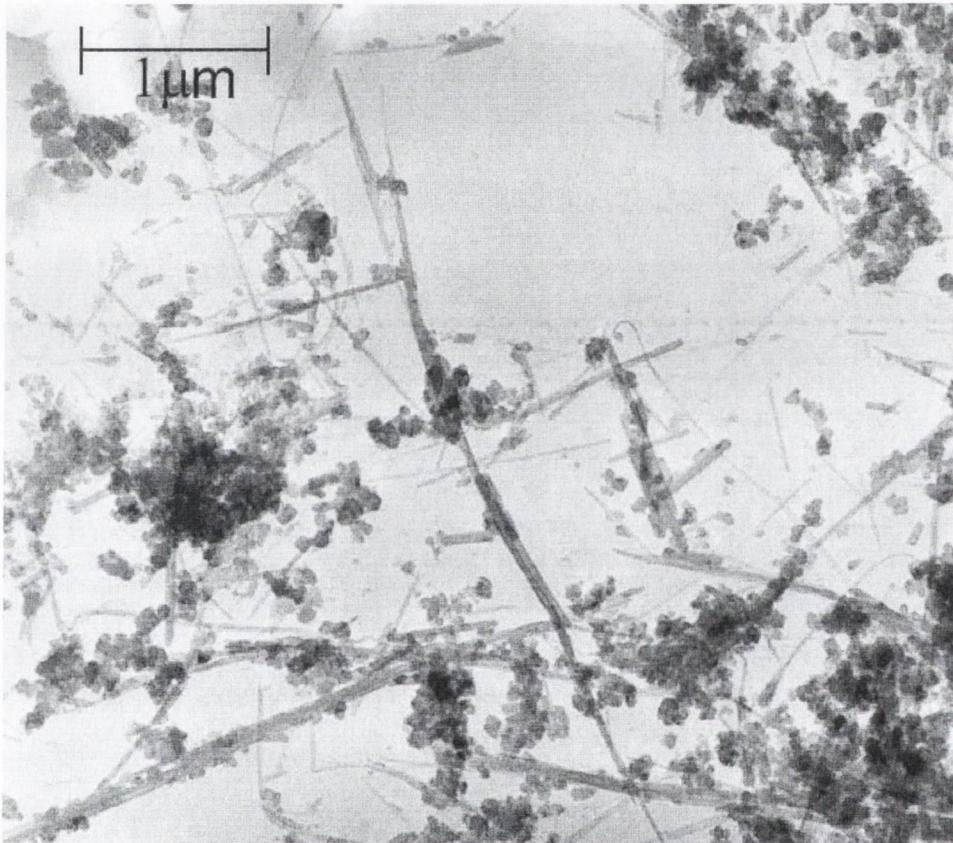
Figure 5.1 TEM of nanotube soot from the Krätschmer generator.

It can be clearly seen that there is an abundance of nanotubes, but also much graphitic particles. There are many nanotubes lying isolated on the TEM grid, which is typical of these samples, but unusual in the other nanotube samples. This makes it much easier for composites of high mass fraction (typically up to 80%[1]) to form than for example SWNT, where the tendency for SWNTs to aggregate means that much lower mass fraction of nanotubes can be solubilised. A. Dalton *et al* has shown[2], as

reviewed in Chapter 4, that above a mass fraction of 1.5% the SWNT do aggregate substantially, and mass fractions above this do tend to precipitate.

It must be noted however, that extremely high mass fraction CDA MWNT composites (up to 400%) can be formed. TEM studies shown here suggest that this is most likely due to the large number of defect sites that nucleate the PmPV coating. A TEM image of CDA MWNT is shown in Figure 5.2 (magnification x100k) is shown for comparison. It can be seen that these have much less shells than the ADM MWNT, and so are much more flexible, forming large intertwined networks of nanotubes. Isolated nanotubes are never seen in these samples, due to the production mechanism, and breaking these networks substantially is difficult.
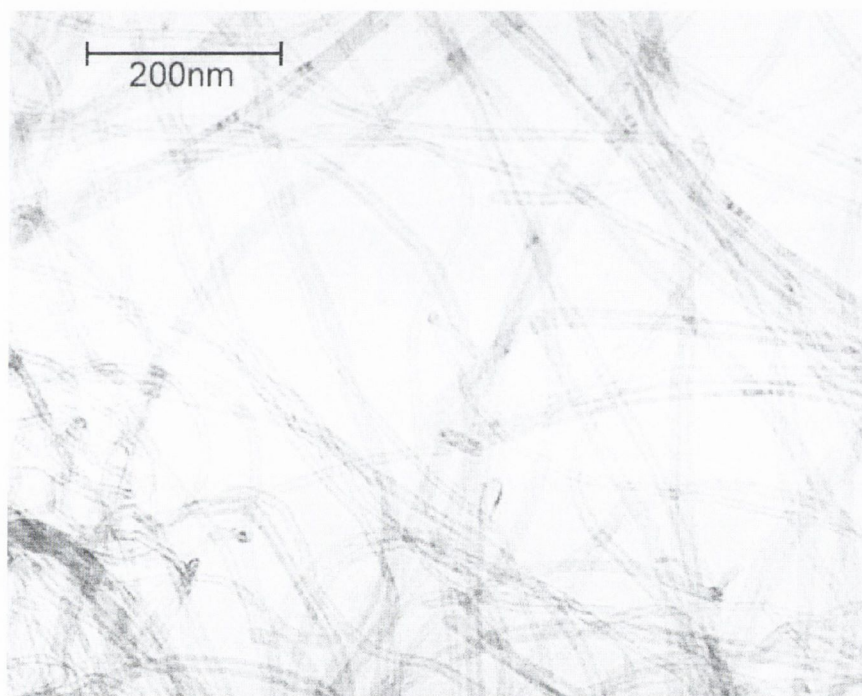
Figure 5.2 TEM image of catalytically grown nanotubes.

The rigidity of the ADM MWNT is due to the large number of shells, typically having 50-100 shells, as compared to CDA MWNT, which usually have less than 10. They are also much better graphitised than CDA MWNT are. CDA MWNT also tend to be

much more consistent in length and diameter than ADM MWNT, as the production conditions are much more stable than those of an arc discharge plasma.

ADM MWNT also predominantly consist of graphitic particles. However, by the production method in Trinity, the nanotube content is much higher than most other nanotube samples produced by the Arc Discharge technique. The nanotube content of the ADM MWNT samples used here has been quantified as 34%[3].

The CDA MWNT samples are nearly 100% nanotubes, with the only other significant component being the catalytic particles left over from production. However, these nanotubes do not tend to be as well graphitised as the ADM MWNT samples, with a large number of defects, and catalytic particles embedded in the nanotubes.
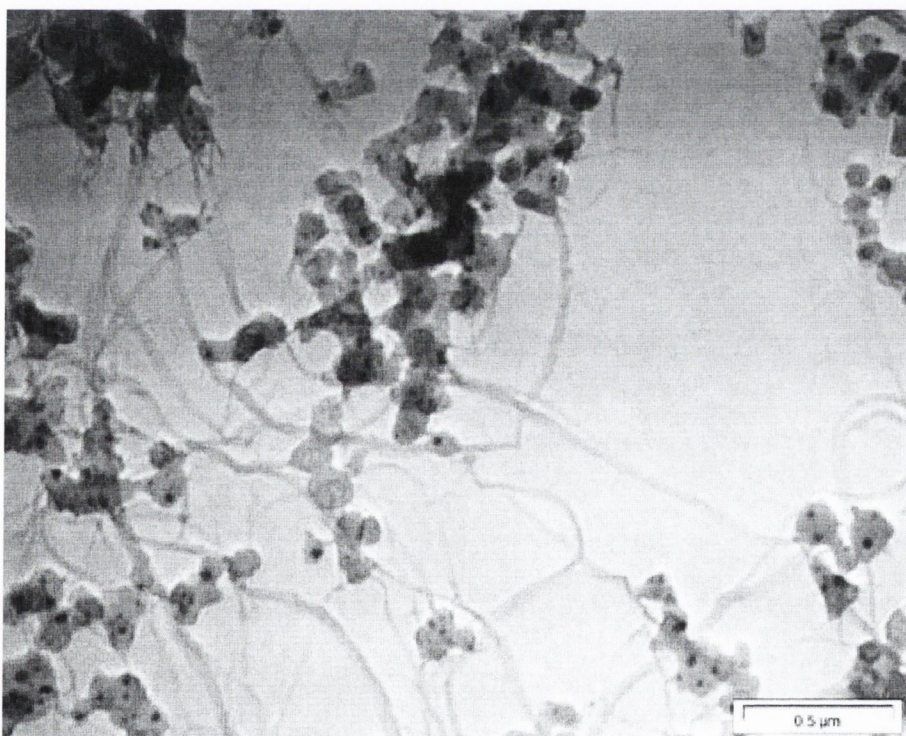
Figure 5.3 TEM of a SWNT sample.

A TEM image of a SWNT sample is shown in Figure 5.3. These samples are similar in appearance to CDA MWNT as their flexibility causes them to aggregate easily.

Typical diameters of these strands are up to 25nm, showing that these are large ropes of SWNT, and not individual nanotubes. The purity of these samples supplied by the Montpellier group has been claimed to be as high as 70%[4], although TEM examination shows a large amount of impurities, suggesting that it is substantially lower for these particular samples.

5.3 Characterisation of Multi-walled Composites
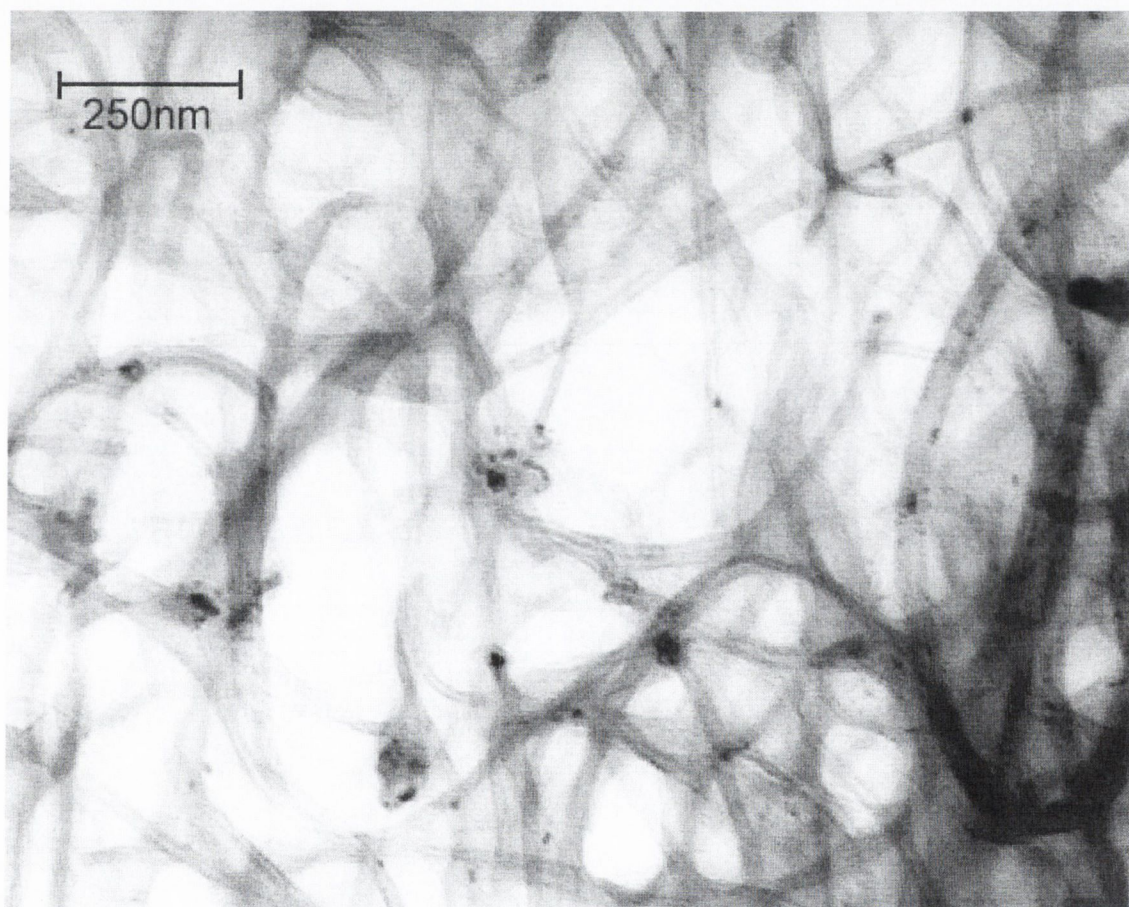
Figure 5.4 TEM of a CDA MWNT composite

To give an indication of the structure of the MWNT composites, TEM images of CDA MWNT (60k) and ADM MWNT (40k) film cross-sections are shown in Figure 5.4 and Figure 5.5 respectively. It can be seen by comparison with Figure 5.2 that the CDA MWNT are relatively unchanged in the composite, with the same large

networks of aggregated nanotubes. These networks are smaller however, due to the sonication partially breaking them up. The catalytic particles are visible as some of the larger black dots in the picture.

Figure 5.5 demonstrates the effect of composite formation on the ADM MWNT samples. Virtually all nanotubes are separated from each other, and although there still is a small amount of graphitic particles, it is significantly less than in the raw powder. The small amount that is observed is probably due to the sample being agitated prior to film formation, rather than being in stable suspension in the composite. Thus, some of the precipitated material is reintroduced into the composite films that are formed.
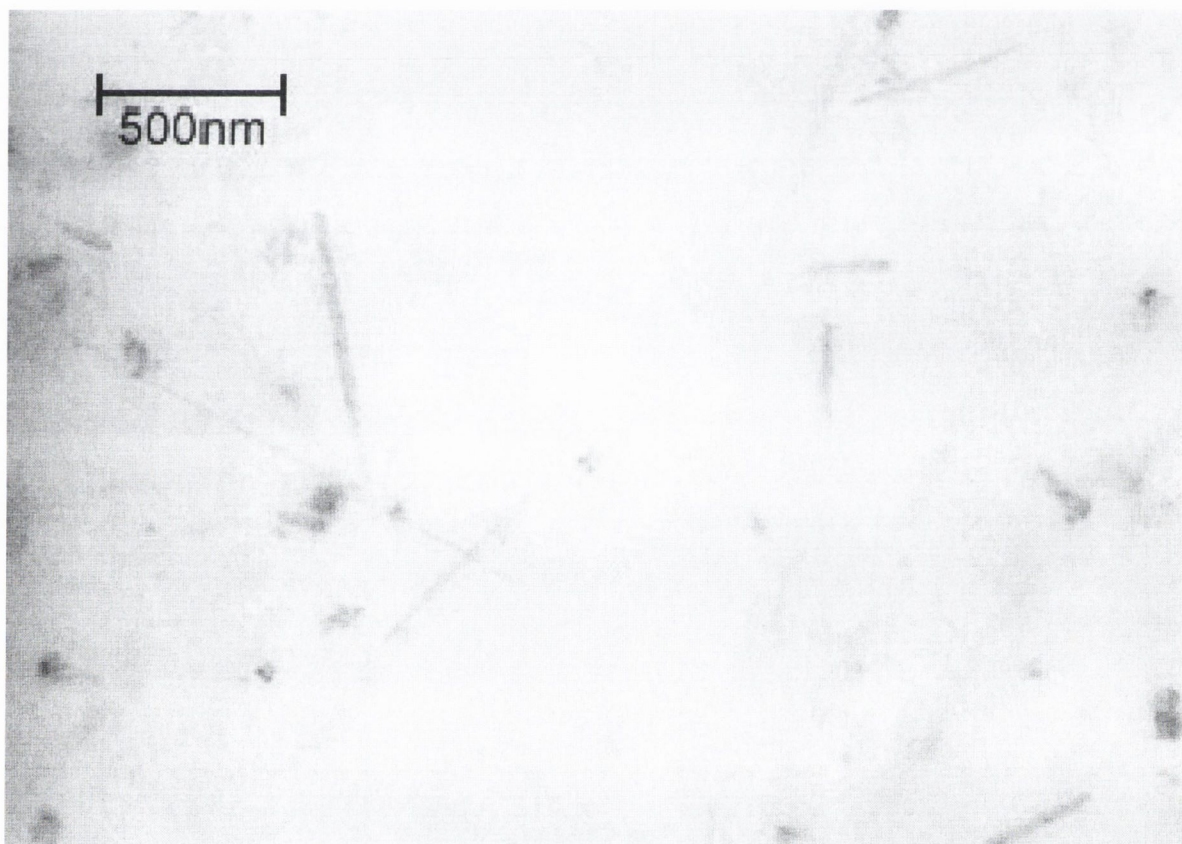
Figure 5.5 TEM of an ADM MWNT composite.

Dendritic Growth[5]
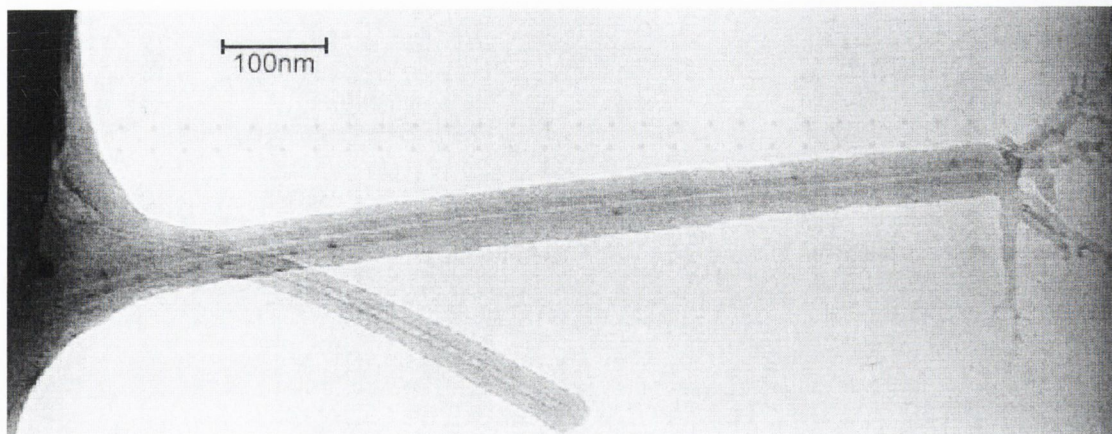
Figure 5.6 TEM of ADM MWNT protruding from the edge of the PmPV film.

Shown in Figure 5.6 are two ADM MWNT protruding from the edge of the PmPV composite film. To give an indication of dimension, the longer nanotube's total diameter including the PmPV is 50nm. Note that the polymer layer coating the nanotubes is very thick, almost twice that of the nanotube's diameter. This indicates that the coating consists of many ropes of polymer, not single strands. Also, the thickness of the coating suggests a strong binding between the nanotube and the PmPV.

Examining the tip, at least five tree-like crystalline polymer structures can be seen growing from it. A magnified view of this is shown in Figure 5.7 b). Figure 5.7 a) shows a further example, but of a CDA MWNT, with numerous growths.

A further example of these dendritic polymer growths (Figure 5.8) helps in understanding the nature of this occurrence. It can be seen that there are approximately twenty growths from the nanotube body (diameter of coated nanotube is approximately 25nm).
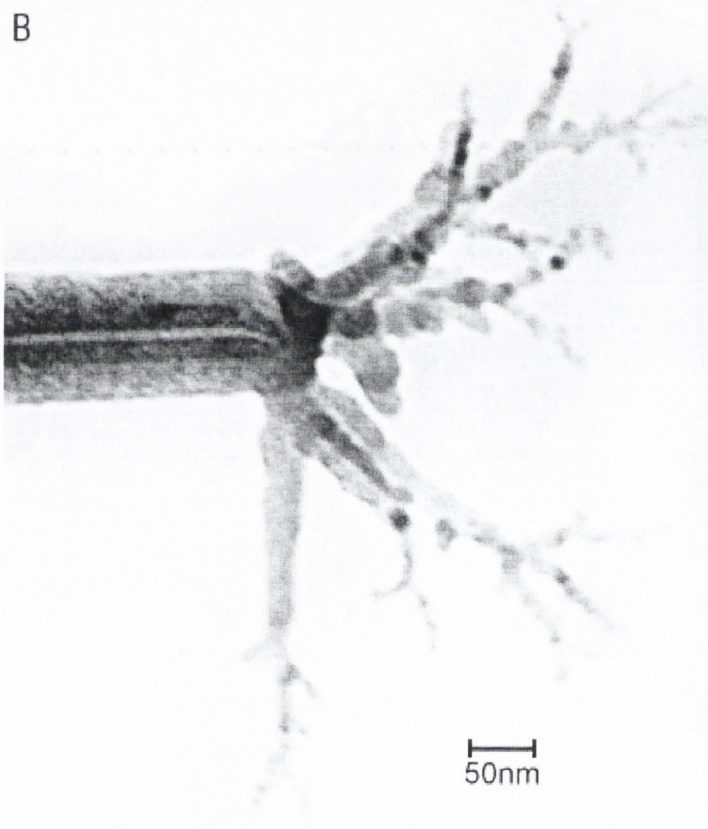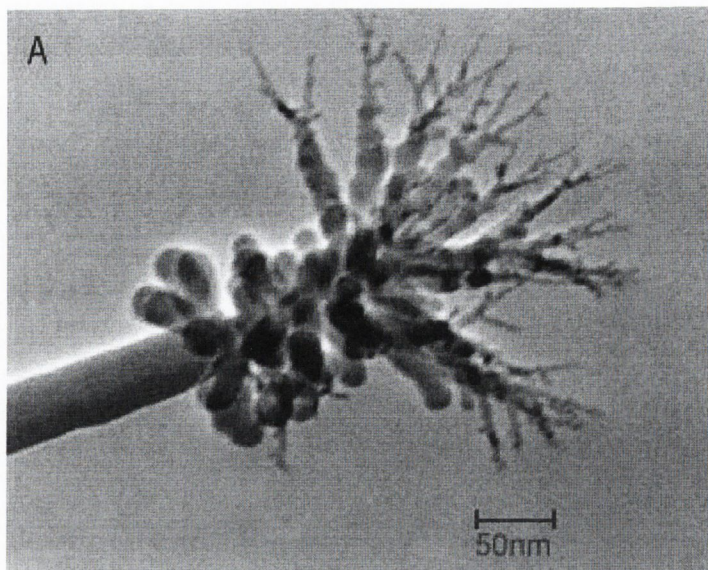
Figure 5.7 Two nanotube tips with polymer growths.
A –CDA MWNT (Body diameter 25nm)
B- ADM MWNT (as in Figure 5.6) (body diameter 50nm)

The nanotubes in this composite are produced by CDA, which as explained previously, have a large number of defects. Some defects, such as pentagons in the nanotube lattice, can introduce kinks and bends into the normally straight nanotube, as seen in this example.

111
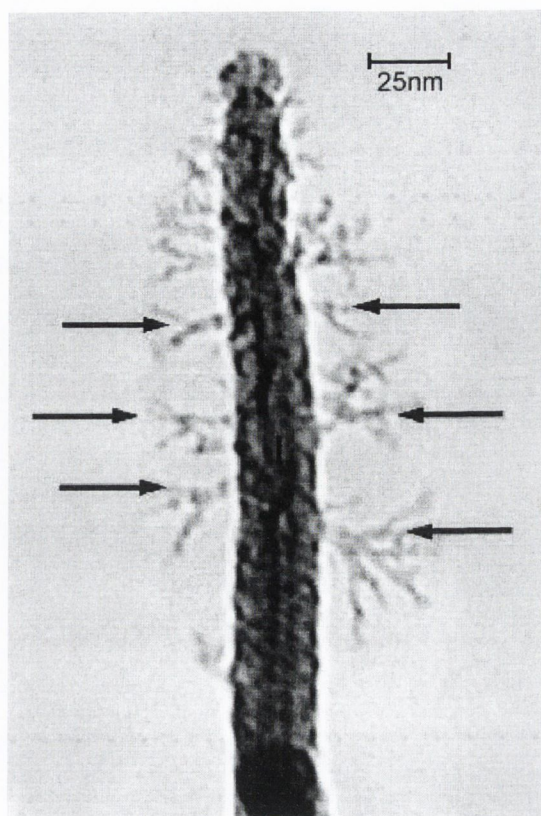
Figure 5.8 A CDA MWNT with polymer growths.

For some of the growths, a strong correspondence between their position and these bend-inducing defects in the nanotube is obvious. These obvious defects are denoted by arrows. Towards the tip of the nanotube, the growths grow more numerous, and it is suggestive that the nanotube tapers gradually as this happens, again requiring defects in the nanotube lattice. It has been observed in TEM studies on vapour grown nanotubes such as these, that frequent bending of the growth axis is observed towards the tip[6]. This has been suggested as due to the introduction of heptagonal defects at these bend locations. These defects are observed here in Figure 5.7 b), suggesting that this is the case in these CDA MWNT samples. Defects in the nanotube tip of the previous example are not as obvious, but as explained in Chapter 3, they are necessary for closure of the nanotube. The tip is irregular, and it is suggestive that the growths in Figure 5.7 a) coincide with the regions of sharpest curvature in the tip.

From the above examples, and several more not presented here, it can be demonstrated that nanotube defects nucleate the crystalline growth of PmPV dendrites. These growths are reasonably common, although they are only observed in a minority of cases. This is understandable, as a suitable defect site for the PmPV to bind to is a necessary but not sufficient condition for these growths to form. As will be explained, these growths can only form in regions of the film where the solvent is evaporating slowly, and therefore the PmPV will precipitate slowly from solution.

As these polymer growths are localised to obvious defect sites, i.e. either at the cap or at bends along the nanotube's body, these defect sites therefore must have a relatively strong attraction with PmPV. This makes it likely that the initial nucleation involves a form of interaction between polymer strand and nanotube defect. It is impossible to ascertain the nature of this interaction, however it must be strong enough to support a substantial mass of polymer. Depending on defect type, the surrounding region tends to have either an excess or deficit of electrons. Similarly, the polymer has a complex dipolar structure, and consequently an uneven electron distribution. There are several possible sites on the polymer that could bind to the nanotube as described. Pentagonal defects in the lattice cause charge localisation in the lattice structure[7]. The polymer's alkoxy groups are electron rich, due to the lone pair on the oxygen atom. The most likely possibility is binding between an alkoxy phenylene segment on the polymer chain and a pentagonal defect on the nanotube. Alternative binding sites are the polymer end groups. Polymer chains are terminated either by a phosphonate group, or by an aldehyde group. These are both electron poor. Either of these can provide a complementary charge to an electron rich defect site on a nanotube.

Due to the crystalline nature of the polymer[8], it is likely that, given a suitable nucleation site, it will aggregate as it precipitates from solution. This dendritic crystal growth has been observed in other systems previously[9,10]. As this nucleation occurs, the polymer, once bound to the nanotube, initiates the formation of lamellae. These are closely packed arrangements of polymer ropes, a precursor to small crystalline spherulites. Here, the formation of chain folded lamellae would be expected. Polymer sites bound to a nanotube provide an ideal nucleation site for this. Furthermore, if the initial anchoring site was an alkoxy phenylene group, which are distributed evenly along the polymer's length, it is likely that small chain folded lamellae would form.

As solvent evaporates, the polymer concentration increases, thus encouraging the slow precipitation of polymer from the solution. As can be seen from all images, polymer is not solely deposited as crystalline dendrites on nanotube defects, but also as a uniform coating on the nanotube's surface. The substantial bulk of the polymer precipitates as a semi-crystalline mass. It seems that there are certain localised regions where it can be favourable to form dendritic structures, rather than to solidify into an amorphous bulk.

Filling and Wrapping

Figure 5.9 shows a TEM of an ADM MWNT nanotube, again found protruding from the composite film. Similar dendritic structures are noticeable again, corresponding with the angular tip, although they are not as pronounced as in previous examples. What is particularly noticeable however is that the nanotube is filled with a large amorphous bulk of polymer.
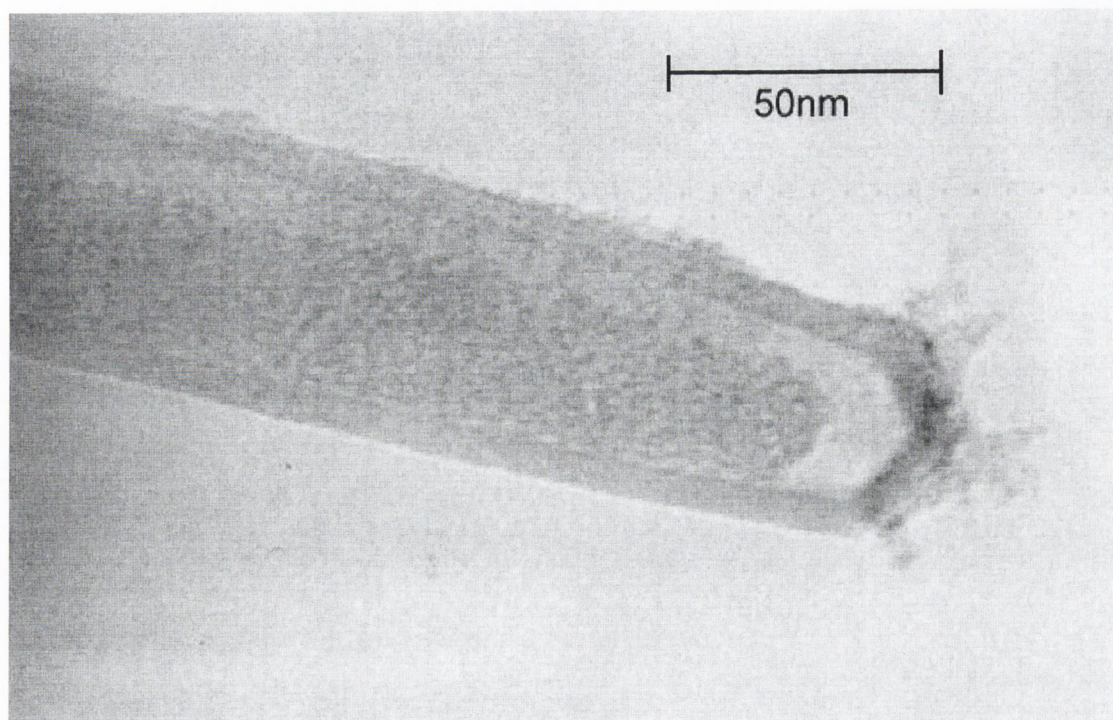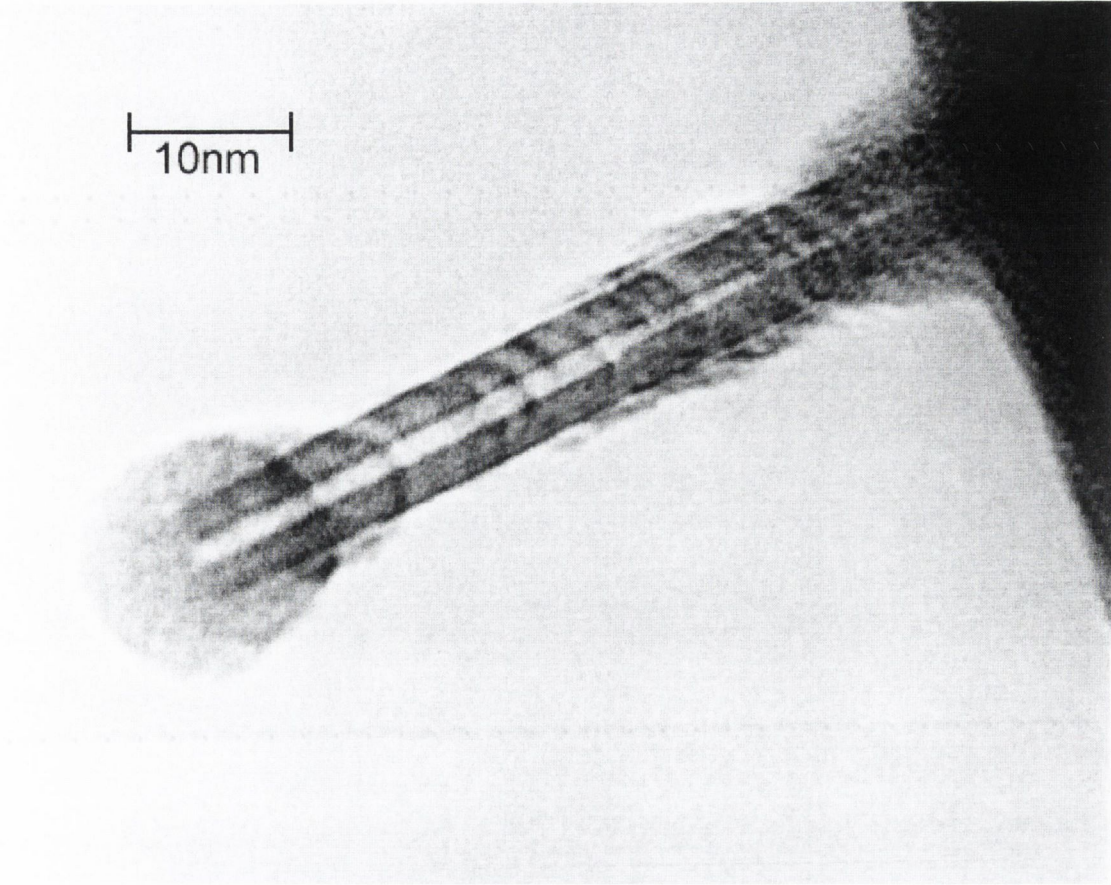
Figure 5.9 TEM of an ADM MWNT nanotube.

The bulk has a similar shape to that of the nanotube, with the end having the same angular shape that the tip has, although it is observably not as well defined as the nanotube. It seems that the PmPV has filled the nanotube, probably from the open end embedded in the film, although this is not examinable. As the film dries, and solvent evaporates, the bulk diminishes in size, although retaining the shape of the nanotube mould. It suggests that the interaction between PmPV and nanotubes is strong enough for the PmPV to be drawn up fully into the nanotube, and remain there. Similar effects have been observed for other materials[11, 12], notably metals, in nanotubes, but this has not been previously observed for organic materials such as this.

Of further interest are the nanotubes shown in Figure 5.10 and Figure 5.11, demonstrating further examples of the interaction between PmPV and nanotubes.

Figure 5.10 CDA MWNT wrapped in PmPV.

Shown in Figure 5.10 is an open, catalytically grown, tube protruding from the polymer film. This tube is open as in the previous example, but due to the thick coating, it is difficult to ascertain whether PmPV is inside this nanotube. The polymer coating the nanotube can be clearly seen. In this instance, wrapping by the polymer occurs in a well-ordered fashion. This can be observed as the periodic loops of PmPV film around the nanotube. A further example is shown in Figure 5.11, where the order in the coating can be clearly seen. This implies a correlation between the arrangement of aromatic hexagons in the nanotube's lattice structure and the surrounding polymer coating.
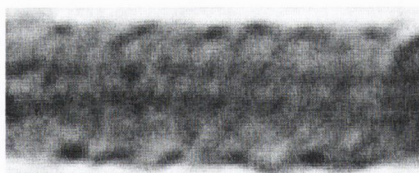
Figure 5.11 Magnified view of nanotube body shown in Figure 5.8.

This suggests a Van der Waals interaction, analogous to J-aggregate stacking of aromatic π-systems[13], between the benzene rings of the polymer and the hexagonal lattice structure of the nanotubes. Recent spectroscopic studies support this hypothesis[14]. Considering the regular spacing of the spiral structure, and the helix dimensions, it suggests that polymer strands are coiling around each other to form ropes, which in turn surround the nanotubes in a regular, structured way. This will be further examined for the case of SWNT composites in the next section, and in Chapter 6, where it will be examined by STM.

5.4 Characterisation of Single-Walled Nanotube Composites

SWNT tend to be much more difficult to characterise by TEM for a number of reasons. The diameter of SWNT puts them near the limit of the TEM's magnification and resolution. The low concentrations achievable with SWNT composites mean that the bulk of the sample is a PmPV film. The diameter also means that there is little contrast between them and the surrounding film, so they can only be imaged when they are extending from the composite film. However, because of their high flexibility, and tendency to form aggregated networks, they do not protrude, but only form networks buried within the PmPV film.
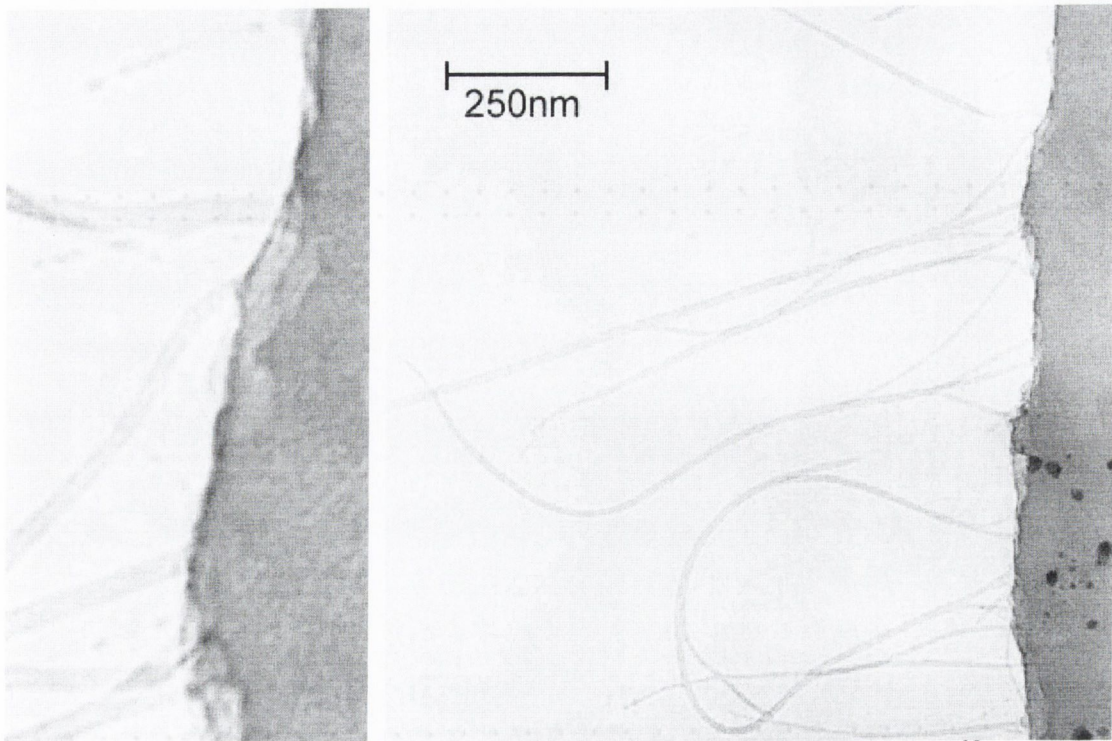
Figure 5.12 TEM of SWNT composites (Magnified view on left).[15]

This can be overcome to some extent by using low PmPV concentration samples, minimising the amount of free polymer, but also SWNT. It is also useful to find tears in the film, where the SWNT can be easily found. Such an example is shown in Figure 5.12 (magnification 60K). A large number of thick ropes can be seen extending from the film edge. A magnified view of the film edge is shown on the right. Observe that, amongst the much larger ropes, there are several faint lines, with a 'beaded' appearance. These are individual SWNT, and the beading is PmPV on the surface of the nanotube. This 'beaded' appearance further demonstrates the good wetting of the nanotube lattice by the PmPV polymer.

Figure 5.13 shows a TEM of a SWNT network coated in PmPV. This sample is one of the more recent SWNT samples made, and the concentration of SWNT is much higher than in earlier samples, of the order of 0.5%, although this cannot be accurately determined. What is seen here is a SWNT aggregate, not unlike those seen in the raw powder (Figure 5.3), but due to the better wetting, much higher concentrations of

118

SWNT can be solubilised by the PmPV. Note that, unlike in the previous example, there is very little free polymer seen in this sample, virtually all of which is bound onto the SWNT ropes and aggregates. The morphology of the samples, however, can be seen to be relatively unchanged, with large aggregates, and associated impurities in these aggregates. As J. Coleman *et al* have shown[3], these impurities alone cannot be solubilised by PmPV, so it is the SWNT that are solubilised, and the impurities that are bound to the SWNT remain in solution. The diameter of these large fibres that can be seen is in the range 70-120nm, so these fibres presumably consist of large ropes with a sufficiently thick PmPV coating to account for the bulk of the PmPV fibre.
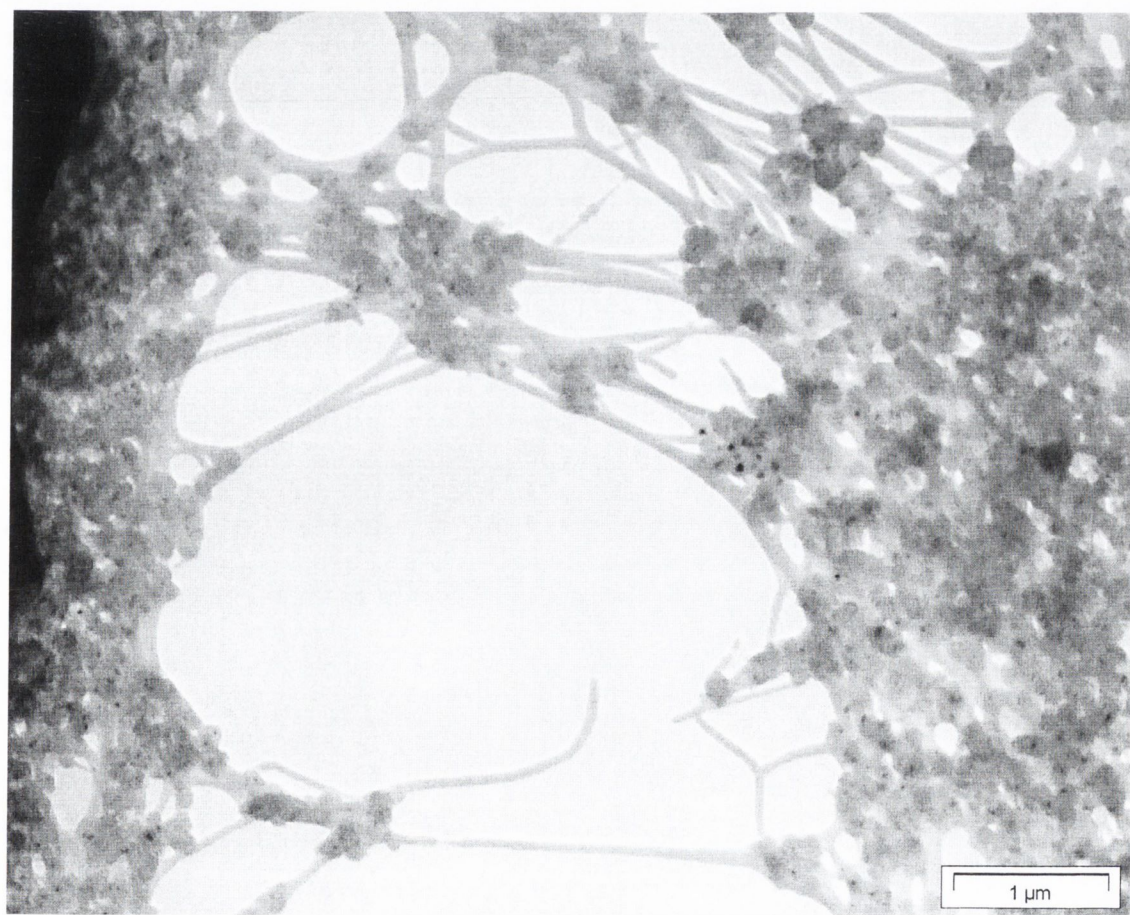
Figure 5.13 TEM of SWNT Composite network.

Figure 5.14 shows a magnified view of the upper right section of Figure 5.13[16]. There are a number of interesting features in this image. Several of the fibres shown can be seen to have hollow cores, the dimensions of which demonstrate that there are ropes of SWNT inside these fibres. SWNT, due to their hollow nature, do have some contrast with the denser PmPV, and this is what is observed here.

The diameters of the observable hollow cores are in the range 6-12nm, while the total diameters of the fibres are typically in the range 100-120nm. This implies that the hollow cores are in fact large ropes, as the diameter of an individual SWNT is of the order of nanometres. It can be observed that the diameter of these fibres changes at the junctions where the fibres join into one. For example, in the middle right of the image, two fibres of approx 112nm join to form a larger diameter fibre of diameter 132nm. This is consistent with the premise that within these are two smaller SWNT ropes joining to form a larger one, although the SWNT ropes within cannot be observed in these particular examples.

Another feature of this image worth noting is the cylindrically symmetrical coating of the nanotube on the bottom right. It appears similar to the beaded structures observed earlier in Figure 5.12, but with a much higher order of symmetry. Also of interest are the variations in diameter over the wrapping, from 106nm at its widest point tapering to 40nm at its narrowest. The wrapping also is at a slight angle to the cylindrical axis, measured at approximately 7°, varying by 2-3° over the length of the structure.
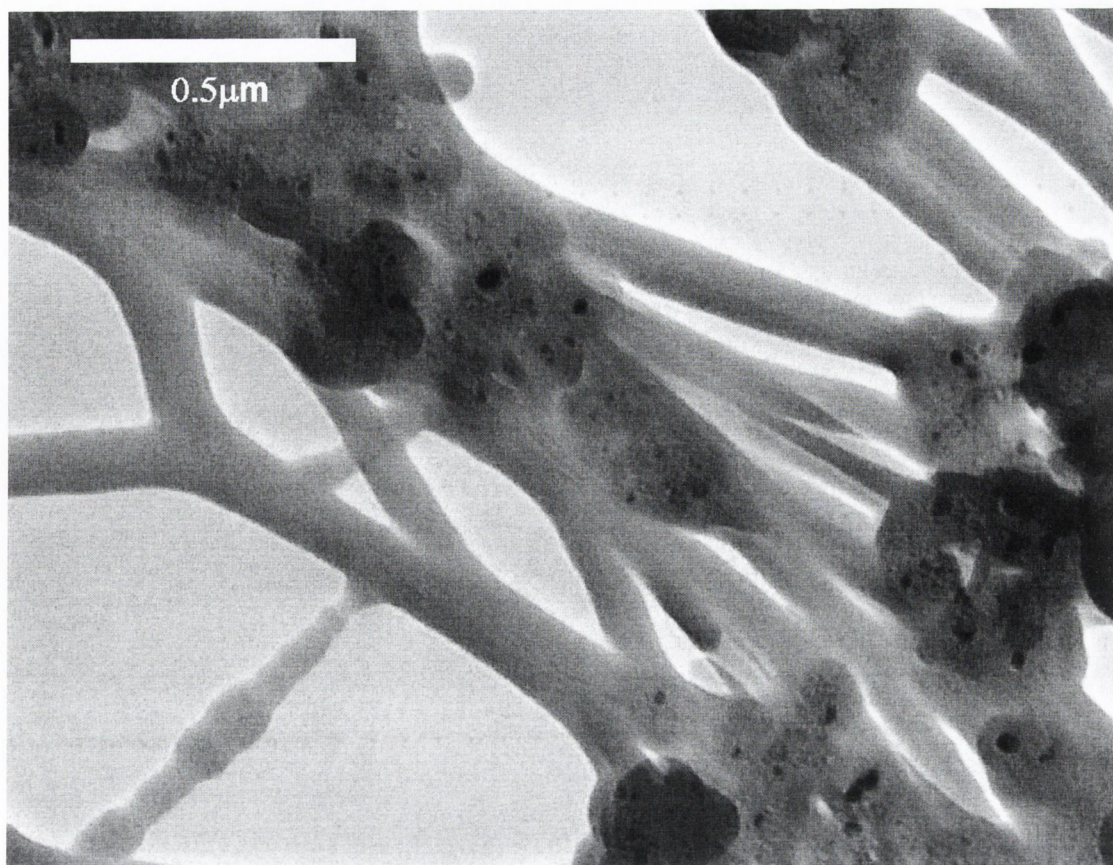
Figure 5.14 Magnified view of upper right section of Figure 5.13.

Compared to the other fibres, which are relatively unstructured and uniform, this particular fibre shows remarkable order and structure. The angular orientation to the cylindrical axis suggests that there is some underlying symmetry within this fibre, which the PmPV is organising onto. This suggests that, unlike the uniform fibres where ropes can clearly be seen, within this fibre there is an individual SWNT. It seems there must exist some correlation between the nanotube lattice structure and the PmPV coating. This explains the angular orientation of the coating, which could be determined by the nanotube's chiral angle, and the marked difference between this example and the uniform fibres seen elsewhere in this image. Higher magnification TEM is unable to resolve any hollow core within this structure. However, given the TEM's resolution, and the thickness of the coating, this is to be expected. As will be

seen in Chapter 7, where this is investigated further using the much higher resolution capabilities of the scanning tunneling microscope, this hypothesis is well supported.

Due to the aggregated nature of these samples, examples of individual PmPV-coated SWNT are rare, although this example is by no means unique. Further studies on the larger fibres have been carried out, and such an example is shown in Figure 5.15. These following TEM images were carried out on holey carbon grids, which are more suited to these composites, as the smaller pore size ensures wider dispersion of the composite over the grids.

1 µm
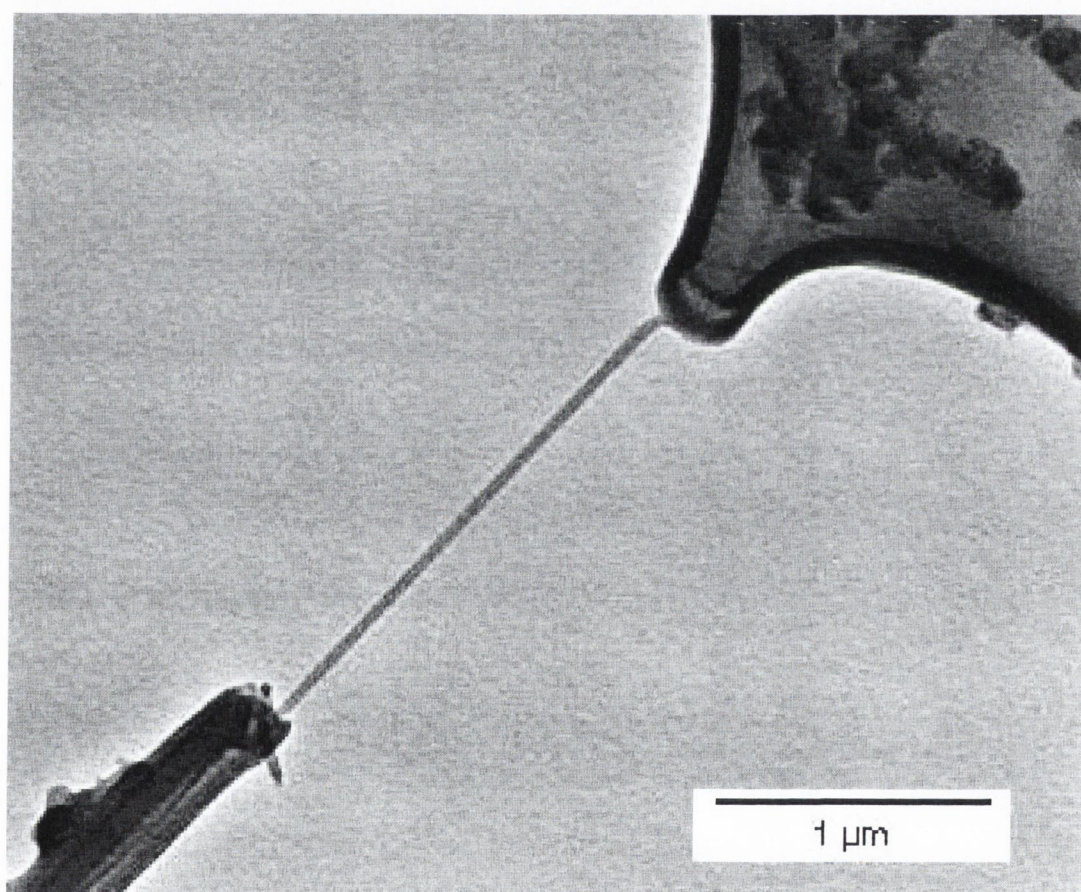
Figure 5.15 TEM of a SWNT rope straddling a tear in the grid.

Figure 5.15 shows a break in the holey carbon, where the two large objects in the upper right and lower left were previously connected, comprising part of the holey carbon film, with two holes on either side. This has broken and receded, possibly due

to the grid being bent while handling. Straddling this break, and preventing the holey carbon receding further, can be seen a fibre, similar to those seen previously.

A magnified view of the lower section of this rope is shown in Figure 5.16, where the hollow core can again be seen clearly at the base of the fibre. The diameter of this rope at the centre is 15nm. It can further be seen that the fibre continues past the edge of the holey carbon, demonstrating that this fibre is lying on top of the substrate.

0.1 μm
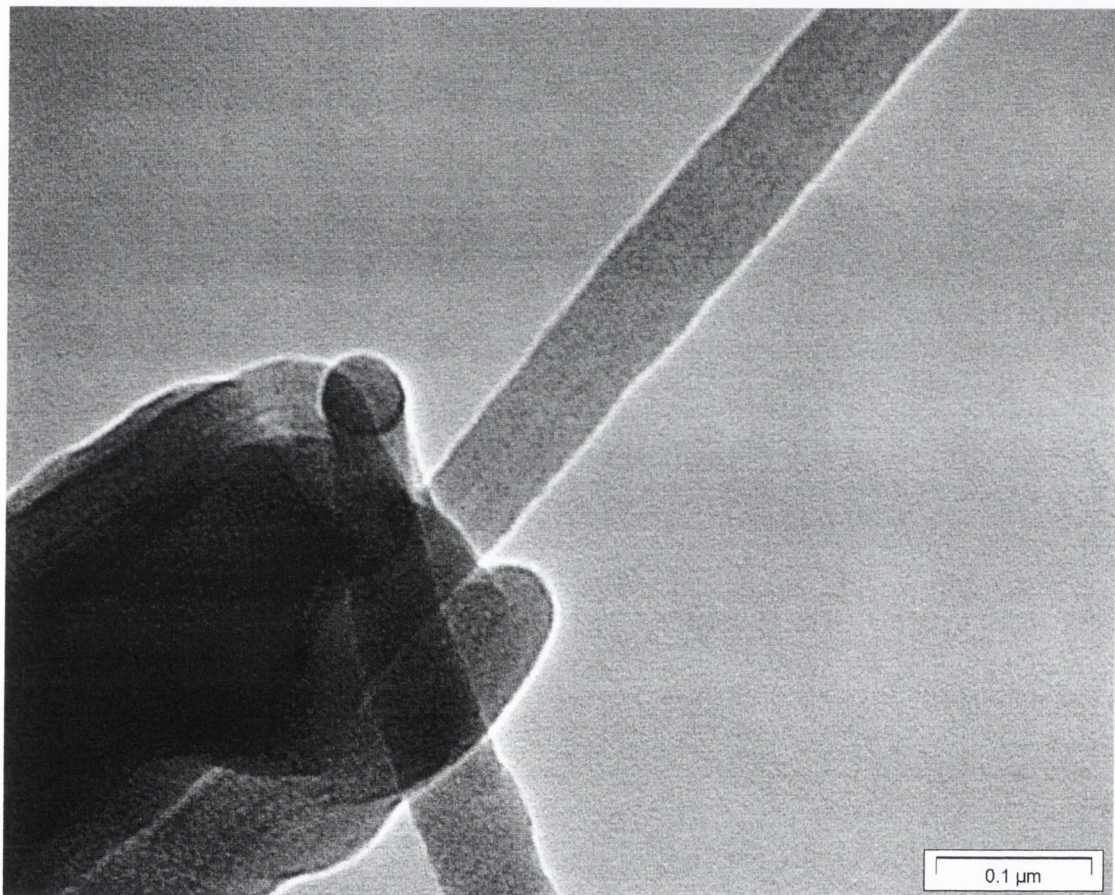
Figure 5.16 Magnified view of the fibre shown in Figure 5.15.

What is of note in this fibre is that high magnification images, at 600k magnification, shows long thin parallel structures within this fibre (Figure 5.17). These can be measured at approximately 1.7nm in diameter, although the resolution of the image is poor, so this cannot be exact. Journet *et al.* have measured the intertubule distance of SWNT ropes as 1.7nm[17], suggesting that these ropes are unaffected by composite

formation, with no PmPV intercalating between them. This agrees well with previous characterisation, showing that SWNT composites above 0.5% consist of predominantly ropes of SWNT[18]. This is interesting, as it confirms the previous hypothesis that these uniform coatings are the result of PmPV wrapping SWNT ropes.
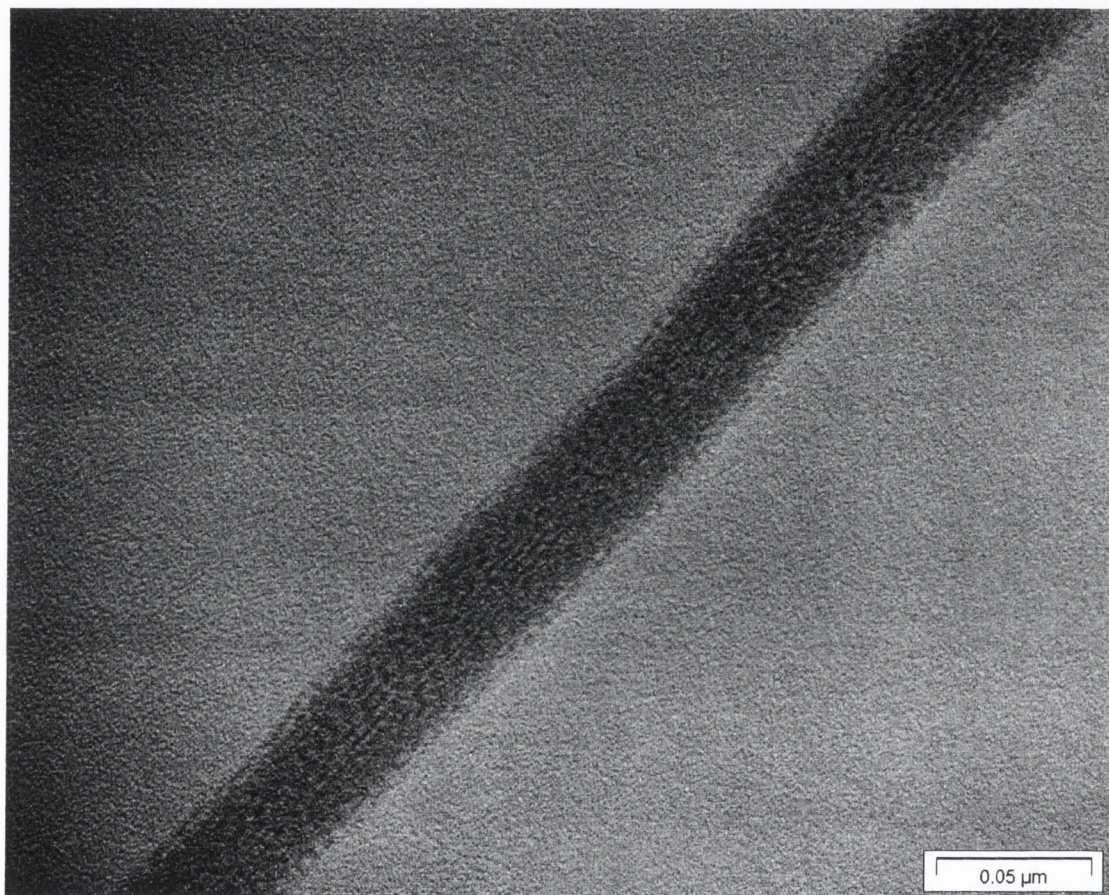
Figure 5.17 High magnification (x600k) image of rope seen in Figure 5.16.

Furthermore, Figure 5.18 shows another high magnification image of a junction in a system of SWNT ropes. A larger rope, of approximate diameter 19nm, can be splitting into two smaller ropes. The diameter of the rope on the left is approximately 9nm, and that on the right is approximately 12nm. These diameters do agree well, although owing to the limited resolution of the TEM, this cannot be exact.
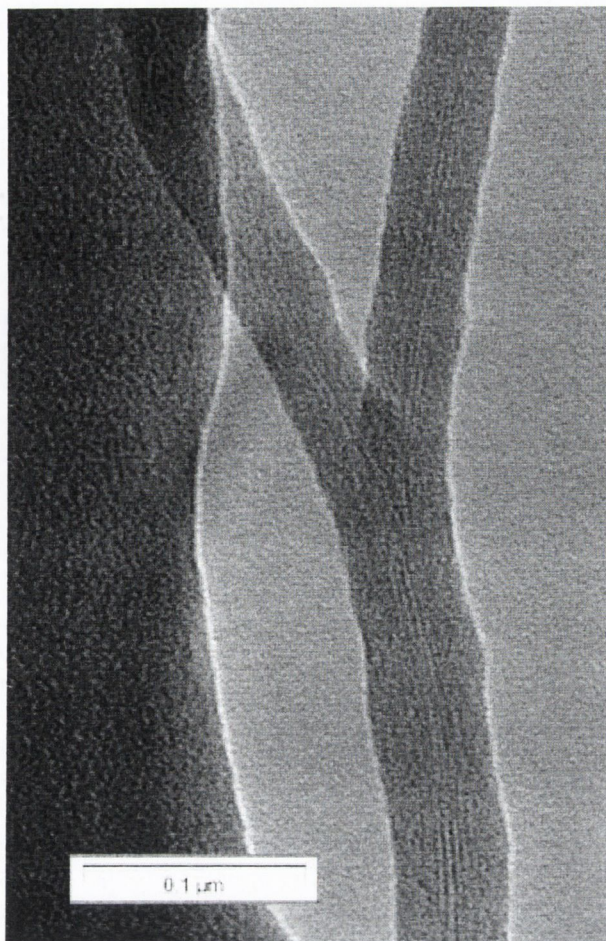
Figure 5.18 TEM of a junction in a system of SWNT ropes.

5.5 Conclusions

Transmission Electron Microscopy has been used to characterise the local structure of composites based on a range of nanotubes. Initially, to demonstrate the microscopic structure of the nanotubes, and to aid understanding of the composite microscopy, TEM images of the three different nanotube samples used here are presented. It can be seen that the nanotube samples differ dramatically from each other.

The purity of multiwalled nanotube samples made by the Arc Discharge Method has been quantified at 34%[19]. For this method, which inevitably produces a large amount of graphitic particles, this is high. However, it can be seen that there are large amounts of graphitic particles present, as both aggregates and attached to the bodies

125

of the nanotubes. As can be seen by how straight the nanotubes are, these nanotubes do have the advantages of being relatively defect-free. They can be imaged at much lower magnifications than the other samples. This is due to the much larger dimensions, being much longer, more rigid and consisting of a much larger number of shells than the other MWNT sample.

The MWNT produced by Catalytic Decomposition of Acetylene are the purest samples used here. Bar the catalytic particles used to nucleate nanotube growth, there are virtually no other impurities. They do however have the disadvantage of being less well graphitised than the ADM MWNT. In sample structure, they appear to be more similar to the SWNT samples than the ADM MWNT samples. They form large intertwined networks, and are never found isolated. This is because they have a much lower number of shells, estimated at being less than ten, and are therefore more flexible, and can interact with each other much more readily. They do also tend to be less well graphitised, with a much higher frequency of defects.

Similarly, SWNT samples do tend to form networks of nanotubes. More problematically, they virtually always form large ropes, which are difficult to break up. They also appear to qualitatively have the largest amount of impurities, but this has not been quantified for these particular samples.

TEM investigations of MWNT composites yield several unexpected results. Low magnification images of the CDA MWNT Composites appear little different from the raw samples. The PmPV coats the networks uniformly, which have not been broken up by the process of composite formation. The networks are smaller, probably due to the sonication. ADM MWNT composites are significantly different. There is very

little graphitic impurities in the sample, agreeing with previous EPR and Raman characterisations. The nanotubes are also well separated from each other.

Examining the nanotubes further, dendritic growth of PmPV can be observed. This is only observed from the tips of ADM MWNT, but from the bodies and tips of CDA MWNT. Closer inspection of these dendritic growths shows that they originate from places of obvious defects in the nanotubes, regions of sharp curvature in the tips, and kinks and bends on the nanotube bodies. This demonstrates that these defects are nucleating the dendritic growth, suggesting that the binding of PmPV to nanotube is much different at these locations. This also qualitatively indicates the imperfect structure of CDA MWNT. Note that the formation of these dendrites is rare, as it also requires certain conditions in the sample preparation, namely a slow evaporation of solvent and consequent slow precipitation of PmPV.

Further examination of the bodies shows an ordered coating, indicating that there is some structured interaction between PmPV and nanotubes. This is clearer in the case of the SWNT characterised by TEM and STM. In addition, demonstrating the strength of the interaction is the filling of a nanotube by capillary action. This is a singular observation, as it requires a partially opened tube, which is extremely rare.

Examination of the SWNT composites shows that in general, the SWNT ropes are not broken up as the composite forms. Commonly observed are large fibres, consisting of large ropes of SWNT heavily coated in nanotubes. Further examination of these reveals that these ropes can be observed, and features such as junctions within these fibres can be seen. The intertubule spacing of the PmPV coated SWNT is unaffected by the composite formation, showing the ropes are unaffected, with no PmPV intercalating between nanotubes.

Of much interest are the uncommon observations of cylindrically symmetric structures observed in the coating of SWNT. Surprising, the axial symmetry of the coating is not parallel to the nanotube axis, but rather at a slight angle of 7°. It is suggested that this angle is due to the chiral angle of nanotube, and that there is an ordered mapping in the interaction from PmPV to nanotube lattice. This is explored further in Chapter 7, where PmPV and SWNT composites are examined by STM.

References

[1] J.N Coleman, private communication.

[2] A.B. Dalton, C. Stephan, J. N. Coleman, B. McCarthy, P. M. Ajayan, S. Lefrant, P. Bernier, W.J. Blau, H.J. Byrne, *J. Chem. Phys. B*, **104**, 10012 (2000).

[3] J. N. Coleman, D.F. O'Brien, A.B. Dalton, B. Mc Carthy, B. Lahr, A. Drury, R.C. Barklie, W.J. Blau, *Chem. Comm..*, 2001 (2000).

[4] C. Journet, W.K. Maser, P. Bernier, A. Loiseau, M. Lamy de la Chapelle, S. Lefrant, P. Deniard, R. Lee, J.E. Fischer, *Nature,* **388**, 756 (1997).

[5] B. Mc Carthy, J.N. Coleman, S.A. Curran, A.B. Dalton, A.P. Davey, Z. Konya, A.Fonseca, J. B.Nagy, W.J. Blau, *J. Mat. Sci. Lett.,* to be published.

[6] M. Endo, K. Takeuchi, S. Igarashi, K. Kobori, M. Shirasishi, H.W. Kroto, *J. Phys. Chem. Solids*, **54**, 277 (1993).

[7] P. Lambin, A. Fonseca, J.P. Vigneron, J. B.Nagy, A.A. Lucas, Chem. *Phys. Lett.*, **245**, 85 (1995).

[8] R. Resel, B. Tertinek, S. Tasch, A.P. Davey, W. Blau, H. Horhold, H. Rost, G. Leising, *Synth. Met.*, **101**, 96 (1999).

[9] T.A. Witten, L.M. Sander, *Phys. Rev. Lett.*, **47**, 1400. (1981).

[10] I. Vicsek, *Phys. Rev. Lett*, **53**, 2281 (1984).

[11] J. Cook, J.Sloan, M.L.H. Green, *Fullerene Sci. and Tech.,* **5**, 695 (1997).

[12] D. Ugarte, T. Stockli, J.M. Bonard, A. Chatelain, W.A. de Heer, *Appl. Phys. A*, **67**, 101 (1998).

[13] I. Tinoco, *J. Biol. Chem.*, **82**, 4787. (1963).

[14] A.B. Dalton, H.J Byrne, J.N. Coleman, S. Curran, A.P. Davey, B. McCarthy W.J. Blau, *Synth. Met.*, **102,** 1176 (1999).

[15] A. B. Dalton, C. Stephan, J. N. Coleman, B. McCarthy, P. M. Ajayan, S. Lefrant, P. Bernier, W. J. Blau, H. J. Byrne, *J. Phys. Chem. B*, **104**, 10014 (2000).

[16] B. Mc Carthy, J.N. Coleman, R.C. Czerw, A.B. Dalton, D.L. Carroll, W.J. Blau, Proceedings of the International Conference on the Science and Technology of Synthetic Metals, Austria, 2000, to be published in *Synthetic Metals.*

[17] C. Journet, W.K. Maser, P. Bernier, A. Loiseau, M. Lamy de la Chapelle, S. Lefrant, P. Deniard, R. Lee, J.E. Fischer, *Nature,* **388**, 756 (1997).

[18] A.B. Dalton, Ph.D. Thesis, Trinity College Dublin, (1999).

[19] J. N. Coleman, D.F. O'Brien, A.B. Dalton, B. Mc Carthy, B. Lahr, A. Drury, R.C. Barklie, W.J. Blau, *Chem. Comm.*, 2001 (2000).

Chapter 6

Spectroscopy of PmPV/Nanotube Composites

6.1 Introduction

In this chapter, some of the interesting properties of SWNT composites will be investigated and characterised. Previously, in Chapter 5, the nanoscale structure of these composites were investigated, showing many surprising effects, such as strong binding, nucleated growth, and ordered mapping of PmPV onto SWNT. Here, optical and vibrational spectroscopy will be used to characterise these interactions, and gain a greater understanding of these phenomena for the case of SWNT-based composites.

To ensure that the effect of the nanotubes was pronounced, the samples were prepared with as high as concentration of nanotubes as possible. To achieve this is very much a matter of trial and error, as the maximum amount of SWNT suspended is heavily dependent on concentration of PmPV solution. At very low concentrations of PmPV, e.g. 10^{-6}M, the saturation limit is dramatically higher. However, these low concentrations make spectroscopy in solution difficult, and spectroscopy in the solid

state impossible. Thus, there must be a compromise between the two aims of maximising the ratio of nanotubes to PmPV, and having sufficiently high concentrations of PmPV to make spectroscopic characterisation feasible. The typical PmPV concentration used was 0.5 g/L (10^{-4}M). The exact proportion of nanotubes cannot be determined, as samples were made with an above saturation limit amount of SWNT. These are heavily sonicated, allowed to stand, and decanted to remove excess unsolubilised SWNT. The amount left in solution is estimated as of the order of a few percent; however, this has not been quantified exactly. When measurements are made in the solid state, films are prepared by repeatedly spin-coating layers to achieve sufficient thickness.

It should also be noted that all spectroscopic measurements in solution were carried out using toluene as a solvent. The solvent does affect the phenomena observed, but will be the subject of further investigations.

6.2 Optical Spectroscopy

6.2.1 Absorption Measurements

Shown in Figure 6.1 are the absorption spectra of the composite, with reference spectra of the pure PmPV, and SWNT for comparison. The SWNT composite and PmPV are prepared from identical samples, with concentrations of 1 g/L. These spectra are of films spin-coated onto Spectrosil B disks, which is transparent to 200nm, and thus allows the higher energy region of these samples to be examined. Spectra are taken over the range 1.38-6.16eV (200-900nm), and are plotted in eV for ease of interpretation. Due to the absorption of the SWNT, the measured spectrum of the composite differs to that of the pure PmPV, and so both are normalised to the lowest energy peak at ~3eV.

The SWNT film was prepared by dropcasting a suspension in chloroform onto Spectrosil B. In this region, the absorption of SWNT is relatively featureless, exhibiting broad scattering and absorption throughout the spectrum, with a maximum at approximately 5eV, as observed elsewhere[1]. It is included here to demonstrate that features in the composite spectrum are not due to a simple superposition of components, but due to modification of the PmPV spectrum by the introduction of nanotubes.
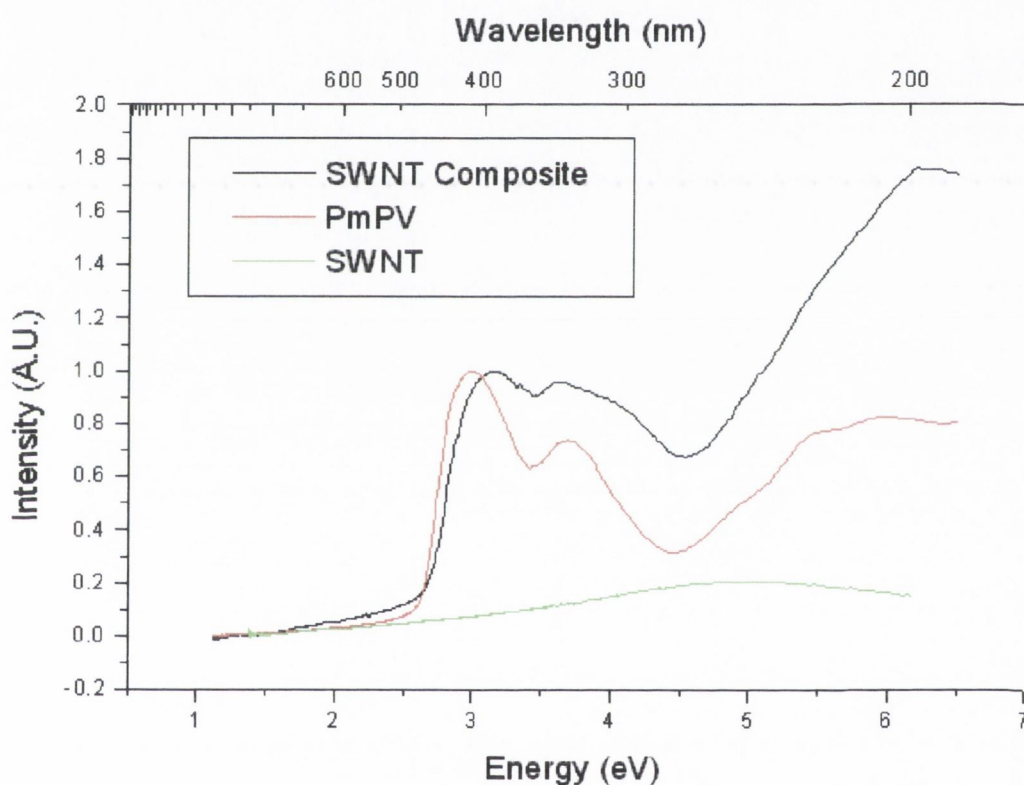
Figure 6.1 UV-Visible Absorption of Composite, PmPV, and SWNT. Composite and PmPV concentrations are 1 g/L

Examining the spectrum of PmPV, there is a sharp onset of absorption at 2.6eV. The width of the observed absorption peaks is associated with the presence of unresolved vibronic structure. The onset is markedly blueshifted compared to standard PPV, demonstrating that the *meta*-linkage is effective as an interruption of main chain

133

conjugation resulting in increased electron localization, and therefore blueshifting the PmPV spectrum.

Another point of note is that the spectra here are solid-state measurements, necessarily so in order to examine the higher energy regions. Due to the close proximity of the strands, there are significant effects due to the increased interchain interactions. This is most noticeable in the redshifted low energy peak at ~3eV, which appears at 3.2eV in low concentration solution measurements[2]. As will be explained later, this peak is markedly affected by interchain interactions, and this is reflected in the substantial redshift from solution to solid-state.

The low energy spectrum is dominated by two well-defined peaks at 2.98eV and at 3.69eV. The low energy peak at 2.98eV is due to transitions between states delocalised along the PmPV backbone[3]. The state at 3.7eV has been assigned to the effects of broken charge conjugation symmetry in substituted PPV derivatives[4]. There are three poorly resolved features in the higher order (>4.5eV) region, at 6eV, 5.45eV and 4.98eV. These are due to localised excitations of the electrons on the phenyl ring[5].

When comparing the absorption of the SWNT/PmPV composite to the pure polymer, it is immediately noticeable that there are many dramatic differences. The low energy peak has blueshifted from 3eV in the polymer to 3.15eV in the composite. This suggests a substantial reduction in electron delocalisation along the backbone, consistent with the observations that there is curvature imposed on the backbone, as it wraps on the cylindrical substrate provided by the nanotube. This has been previously suggested by Ago et al.[6]. There is also the further effect of reducing the interchain interactions, and thus the aggregated morphology of the PmPV in solid state. The

3.7eV PmPV peak, upon introduction of the SWNT, splits into two features, 3.64eV and 4.0eV. It is also noticeably stronger in the composite, its absorption being nearly as strong as the 3eV peak, unlike the PmPV, where it is substantially less than the intensity of the 3eV peak. As this is due to broken charge conjugation symmetry in the PmPV, it suggests that the symmetry is further broken due to the resultant curvature imposed on the PmPV conformation by the presence of the SWNT. A similar effect is also seen in extremely low concentration solutions[7]. This correlation is possibly due to the reduction in possible conformations of the polymer, in one case bound onto the SWNT, in the other relatively isolated and not subject to interchain effects. Further evidence for this suggestion is offered by the vibrational spectroscopy later in this chapter. There is also less noticeable structure in the high-energy region, but significantly higher absorption. This suggests that the dominant absorption in the composite shifts to the phenyl ring of the PmPV. Possibly this is due to the reduced influence of π-π stacking on the phenyl rings.

6.2.2 Luminescence Measurements

Shown in Figure 6.2 is the fluorescence spectrum of the composite in solution upon excitation at 340nm. The luminescence of the PmPV can be seen to be dominated by a peak at 480nm (2.57eV), with a broad shoulder at 460nm (2.69eV). The introduction of the SWNT dramatically changes the PmPV's emission. The dominant peak changes from the lower energy peak to the higher energy peak. These peaks also blueshift, from 480nm to 475nm, and from 460nm to 450nm. In the PmPV, the higher energy peak appears as a shoulder to the main peak, whereas in the composite, both peaks are well resolved. These changes are similar to the effect of a reduction in concentration, and a corresponding reduction in aggregation effects[2]. The spectrum of PmPV redshifts due to increased interchain interactions, which have a lower energy

than intrachain interactions.
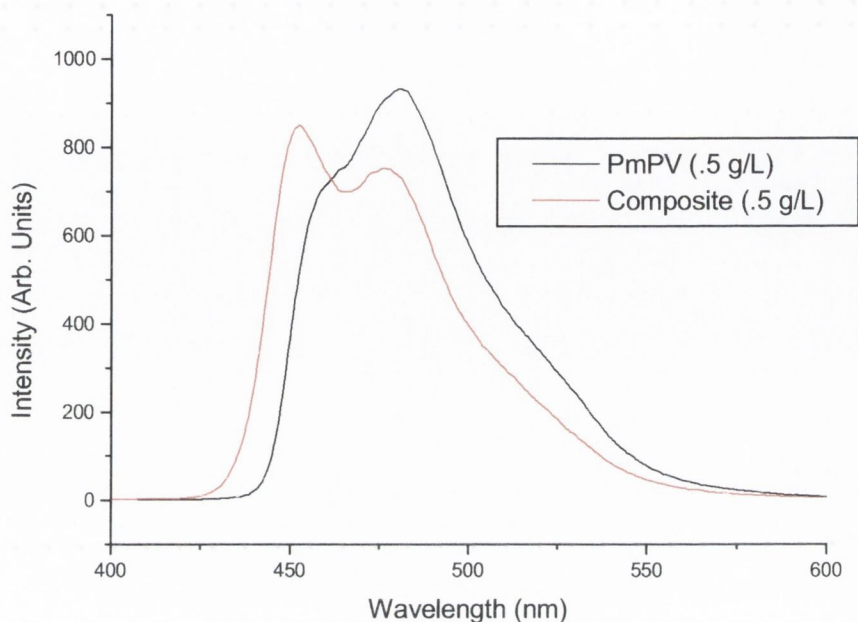
Figure 6.2 Photoluminescence spectrum of PmPV and SWNT Composite.

This suggests that the introduction of SWNT inhibits the formation of aggregates that usually manifest themselves as a redshifted spectrum, with weaker higher energy features. This is due to the binding interaction between the PmPV and nanotube. Thus, the curvature of the nanotube will be reflected in the PmPV conformation, as it arranges itself on the nanotube. As seen by molecular modelling in section 4.2.1, PmPV has a relatively flat backbone, with sidegroups lying in plane with it. This allows the PmPV to aggregate readily, manifesting as a redshifted spectrum dominated by interchain interaction. This curved conformation, however, would seem to hinder interchain species, as the PmPV strands can no longer stack in as close proximity, or over the length of the backbone. In addition, the curved conformation should further reduce the electron delocalisation, further blueshifting the emission spectrum.

6.2.3 Temperature Dependence of Luminescence
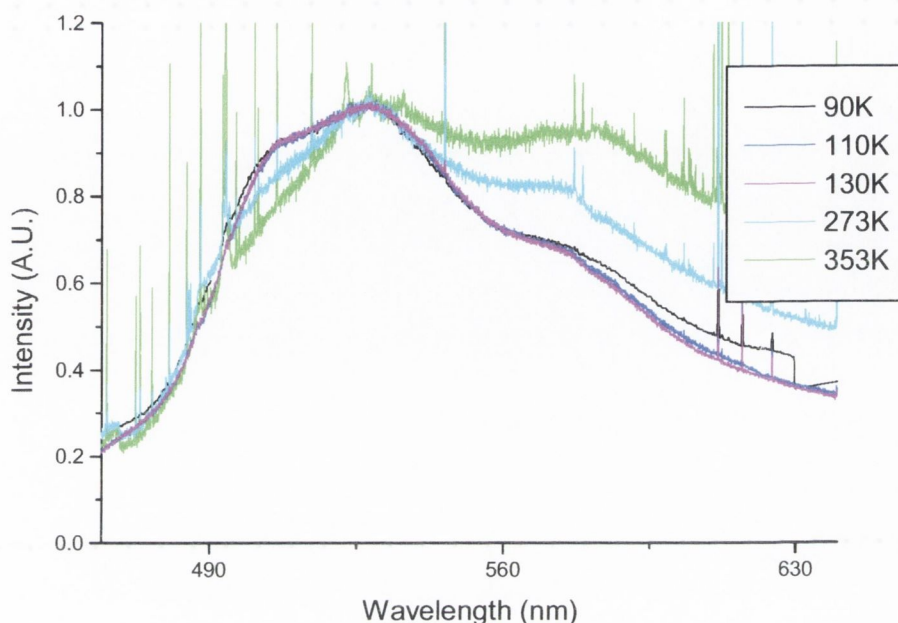
Figure 6.3 Luminescence of SWNT composite from –193°C to 80°C.

Figure 6.3 shows the luminescence of the SWNT composite at temperatures ranging from 90K to 353K. Immediately noticeable about this spectrum is the difference in the wavelength range between this and Figure 6.2. This is due to a different excitation wavelength to that of the room temperature luminescence, being 457nm in this case. The shape at low temperature has a much stronger lower energy peak than the room temperature spectrum. It also has a slight shoulder, which disappears as the temperature increases. Of interest is the change in the relative peak heights; at higher temperatures, the lower energy peak increases in amplitude, suggesting that the effect of the SWNT diminishes as the temperature increases. Further work is needed to investigate this, but it suggests that this technique will be useful in determining the activation energies of the PmPV-SWNT interaction.

6.3 Vibrational Spectroscopy
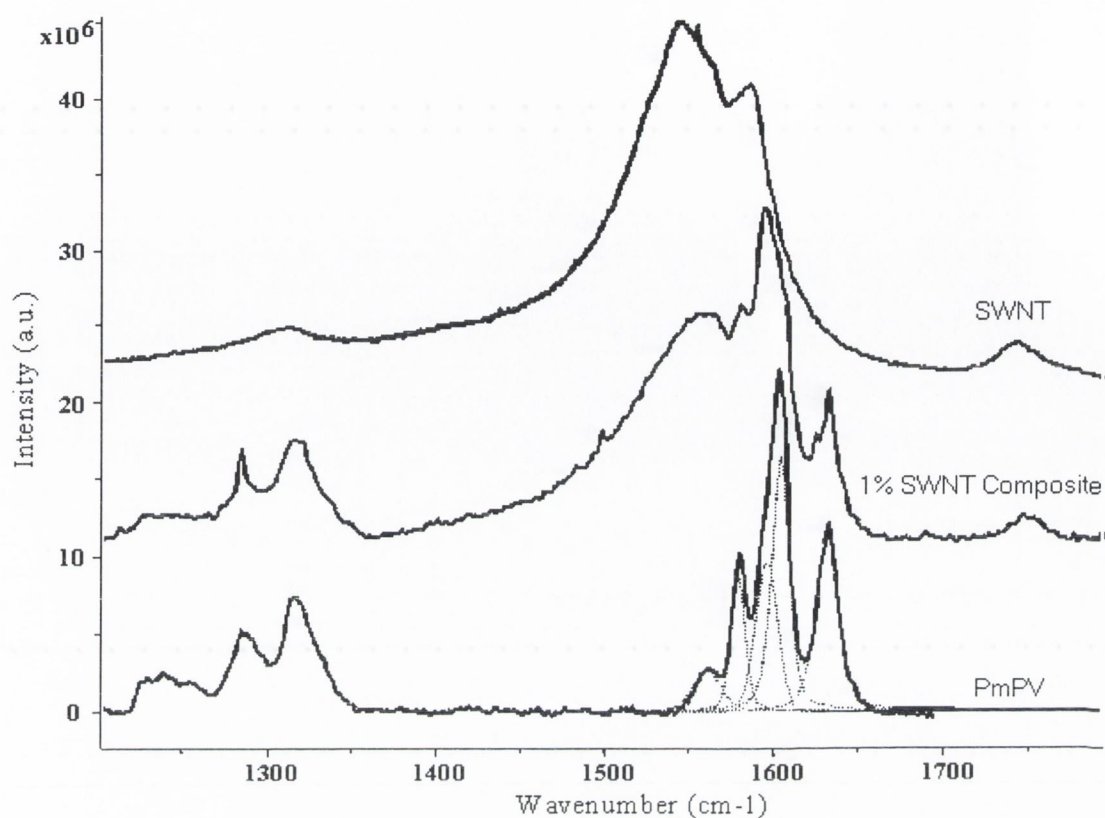
Figure 6.4 Raman spectra of SWNT, Composite, and PmPV.

Raman scattering is a powerful technique to probe the structure-property relationship

in organic systems such as carbon nanotubes and conjugated polymers. Figure 6.4

shows the high frequency region of the SWNT composite, with the pure PmPV and

SWNT shown for comparison. The excitation wavelength used was 676nm. In this

region, the so-called G-line feature at 1580cm^{-1} dominates the nanotube spectrum[8].

This group of modes correspond to the splitting of the E_{2g} mode in graphite into

longitudinal and transverse components at higher and lower energies respectively[9].

The apparent broadening on the low frequency side has been attributed to both

metallic and semiconducting SWNT being resonant at this excitation wavelength[1].

The spectrum of the PmPV is dominated by a multiplet of modes around 1600cm^{-1}.

The band at 1627cm^{-1} is attributed to the vinyl group A_g mode, i.e. the stretching of

the C=C bond. The other bands are attributed mainly to the phenyl group A_g mode, the stretching of the C-C bond[10]. There are also a group of features centred around 1300cm^{-1}. The main band at 1330cm^{-1} has been associated with out of plane vibrations of the vinyl bond[10].

Comparing these to the SWNT composite, it can be seen that there are a number of differences in the features. The broad high-energy peak (1627cm^{-1}) resolves into two sharp features. This is probably due to the restricted nature of the PmPV's vibrational modes due to the interaction with the SWNT. There are also modifications of the relative intensities of the 1610cm^{-1} and 1590cm^{-1} peaks, with the 1590cm^{-1} line becoming dominant. For PPV[11], this mode appears as one, at 1590cm^{-1}. However, for PmPV it splits into two, implying that these two peaks correspond to the *para* and *meta* linkages of the PmPV backbone. The relative change in these peak intensities demonstrate that one of these linkages interacts with the SWNT better. This is probably the linear *para* linkage. The line at approximately 1280cm^{-1}, also becomes much more resolved, agreeing with the suggestion previously that there is a reduction in the possible conformations of the PmPV.

6.4 Conclusions

Optical and vibrational spectroscopies have been used to further understand the effects of composite formation upon the PmPV. Several interesting effects are noted, which can be explained with reference to the microscopy presented elsewhere in this study, TEM observations in Chapter 5, and STM observations in Chapter 7. In addition, previous work on the concentration dependence of PmPV is referenced, as this gives insight into the changes in the optical spectrum upon introduction of nanotubes.

Absorption spectroscopy shows a change in the dominant absorption region from the low energy region to the high energy region. The low energy peak at ~3eV shifts by 0.15eV. The peak at 3.69eV splits into two, one slightly redshifted at 3.64eV, and one markedly blueshifted at 4.0eV.

The photoluminescence spectrum of PmPV also shows dramatic changes upon introduction of SWNT. The pure PmPV has two peaks, a main one at 480nm (2.57eV), the other appearing as a shoulder to the main peak at 460nm (2.69eV). The effect of the SWNT is to blueshift both these peaks, by 5nm and 10nm respectively, and furthermore, these peaks are much better resolved.

The temperature dependence of the spectroscopy of these samples shows that the effect of the SWNT diminishes as temperature increases, suggesting a possible way of determining the activation energies associated with the PmPV-SWNT interaction. However, much more investigation is required to establish this, and they are presented here to show the potential of this technique.

There are also significant changes in the Raman spectra of these samples. The $1627cm^{-1}$ line resolves into two peaks. The $1280cm^{-1}$ line is much more sharply resolved. The relative intensities of the $1610cm^{-1}$ and $1590cm^{-1}$ peaks changes, with the $1590cm^{-1}$ line becoming dominant.

These effects can be attributed to several influences that the SWNT have on the PmPV conformation. By wrapping of the PmPV onto the SWNT, this reduces electron delocalisation along the PmPV backbone, notable in the blueshifted peak at ~3eV in the absorption spectrum. It also hinders interchain interactions, suggested as the spectrum has similar features to an extremely dilute PmPV solution, where

interchain interactions would be minimal. This manifests itself in several ways; the blueshift in the luminescence, the change in the dominant peak of the luminescence, and the reduced intensity of the 3eV peak in the absorption.

There are changes in the Raman and optical spectra that mirror each other. These are the resolution of the 3.64eV peak in the absorption spectrum into two, the splitting of the $1627cm^{-1}$ line, the change in relative intensities of the $1610\ cm^{-1}$ and $1590\ cm^{-1}$ lines, and the much more sharply defined $1280cm^{-1}$ line in the Raman spectrum. The change in the absorption spectrum is similar to that in low concentration solution measurements. It is possible that these can be attributed to a restriction in possible PmPV conformations due to the ordering in the structure it forms on the SWNT lattice.

References

[1] H. Kataura, Y. Kumazawa, Y. Maniwa, I. Umezu, S. Suzuki, Y. Ohtsuka, Y. Achiba, *Synth. Met.*, **103**, 2555 (1999).

[2] A.B. Dalton, PhD. Thesis, Trinity College Dublin, (1999).

[3] H. Mellor, A. Bleyer, D.D.C. Bradley, P.A. Lane, S. J. Martin, F. Rohlfing, A. Tajbakhsh, *SPIE*, **3145**, 382.

[4] Y.N. Gartstein, M.J. Rice, E.M. Conwell, *Phys. Rev. B*, **51**, 5546 (1995).

[5] D. Beljonne, Z. Shuai, J. Cornil, D.A. dos Santos, J.L. Bredas, *J. Chem. Phys.*, **111**, 2829 (1999).

[6] H. Ago, M.S.P. Schaffer, D.S. Ginger, A.H. Windle, R.H. Friend, *Phys. Rev. B*, **61**, 2286, (2000).

[7] A.B. Dalton, J.N. Coleman, M. in het Panhuis, B. McCarthy, A. Drury, W.J. Blau, B. Paci, J. -M. Nunzi, H.J. Byrne, *J. Photochemistry& Photophysics*, accepted.

[8] A. M. Rao, E. Richter, S. Bandow, B. Chase, P. C. Eklund, K. W. Williams, M. Menon, K.R. Subbaswamy, A. Thess, R. E. Smalley, G. Dresselhaus, M. S. Dresselhaus, *Science,* **275**, 187 (1997).

[9] M. S. Dresselhaus, G. Dresselhaus, P. C. Eklund, *Science of Fullerenes and Carbon Nanotubes*. Academic Press, New York, (1996).

[10] S. Lefrant, E. Perrin, J.P. Buisson, H. Eckhardt, C.C. Han, *Synth. Met.*, **29**, E91 (1989).

[11] A. Sakamoto, Y. Furukawa, M. Tasumi, *J. Phys. Chem.*, **96**, 1490 (1992).

Chapter 7

Scanning Tunneling Microscopy of PmPV/Nanotube Composites

7.1 Introduction

This chapter comprises a detailed study of the pure polymer, PmPV, and the PmPV/Nanotube composite by Scanning Tunneling Microscopy (STM). Section 7.2 examines the structure of PmPV dropcast onto Highly Ordered Pyrolytic Graphite substrates. In Section 7.3, SWNT composites, similar to those examined by TEM in Chapter 5, are examined. This examination gives further understanding of the phenomena observed previously by TEM, and by spectroscopy.

7.2 STM of PmPV

The samples used in STM of PmPV were prepared by dropping a small amount of the polymer in toluene solution. This was allowed to dry in air, and then put in the antechamber of the STM for a few minutes to ensure that all the solvent had been driven off. These were then examined by STM.

It should be noted that there are problems with using HOPG as a substrate. Artefacts of cleaved HOPG include long graphite strands, which can be confused with biological and organic molecules[1, 2]. In addition, the graphene planes can in some cases, give rise to large periodic Moiré patterns, either due to multiple tips imaging the substrate, or due to perturbations from other layers in the HOPG[3]. Moiré patterns have been imaged on this substrate, and are significantly different, both in scale and geometry of the patterns they form. However, care must be taken in interpretation of these images. This possibility has been considered, but discounted for a number of reasons, which will be explored in this section.
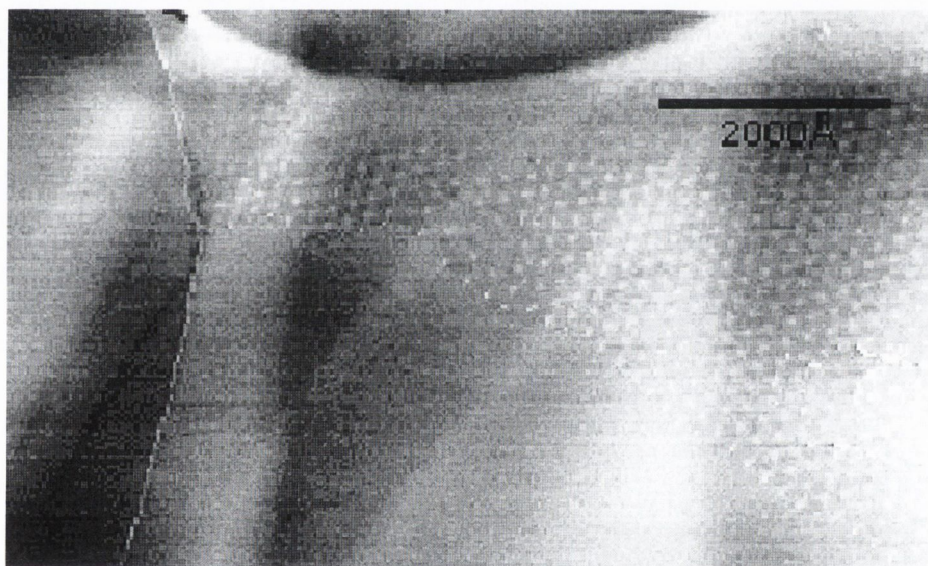
Figure 7.1 Large scale view of PmPV film.

Figure 7.1 shows an image of a PmPV film lying on the HOPG substrate taken at a tunneling current of 140 pico amps and a bias voltage of –500 mV. A magnified view of this is shown in Figure 7.2, where an imperfect, but remarkably regular hexagonal lattice can be seen. This image is taken at a tunneling current of 60 pico amps and a bias voltage of –100 mV. These ordered films are commonly observed extending to dimensions of the order of microns. The sides of these hexagons are approximately 2.6nm, and the average diameter is 6nm. The lattice is well ordered, but observed to

become distorted towards the upper left of the image. In addition, more notably, there is an abrupt transition from the ordered lattice of the upper right to a smooth and unordered region in the lower left.
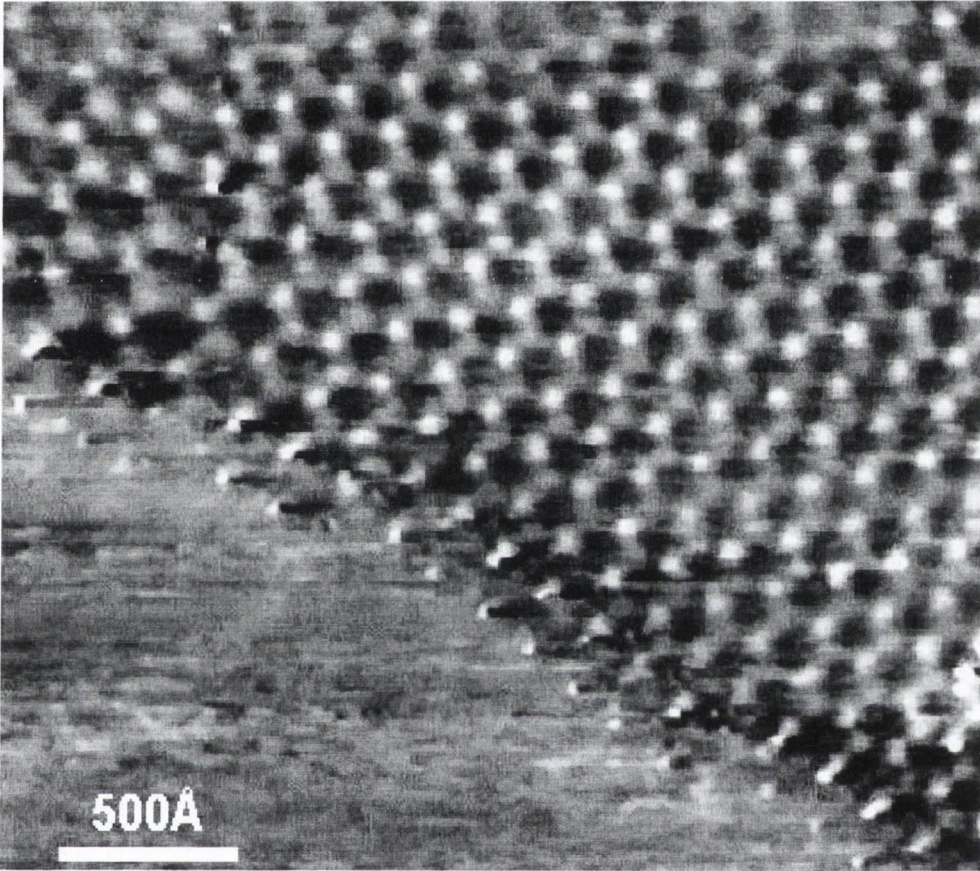
Figure 7.2 Magnified image, showing ordered PmPV film

Comparing the topography of these two regions, given in Figure 7.3, it can be seen that although the topography modulates throughout the ordered region, and is more or less constant over the unordered region, the average height does not change at the transition. There are two possible reasons for this.

One is that PmPV is coating the entire substrate, and the difference between these two regions is due to the PmPV being in two phases, amorphous and crystalline. The other is that this modulation is due to the electronic structure, and the topographical modulation is due to variance in the electronic structure in the PmPV, e.g. between

the PmPV backbone and endgroups. This cannot be definitively determined, however, given the well-defined structure of the film, it seems that the latter is more likely.

It should be noted that within the film, the brighter regions are due to higher currents at these points. Regions have higher tunneling due to either topography (Figure 7.3), the tip-sample separation being less, or local electronic structure, there being a greater LDOS and therefore tunnelling current at these points. The STM cannot distinguish between these, so it is debatable whether these brighter regions are topographical or not in nature. It seems probable, however, that both effects, topographical and electronic contribute, as would be expected for well-ordered PmPV on a substrate.

Figure 7.3 Cross-section of ordered film.

This is because the brighter regions must correspond to some part of the polymer structure, e.g. sidegroups or endgroups, which differs significantly from the darker regions of the polymer. If this is the case, the polymer will differ in both local
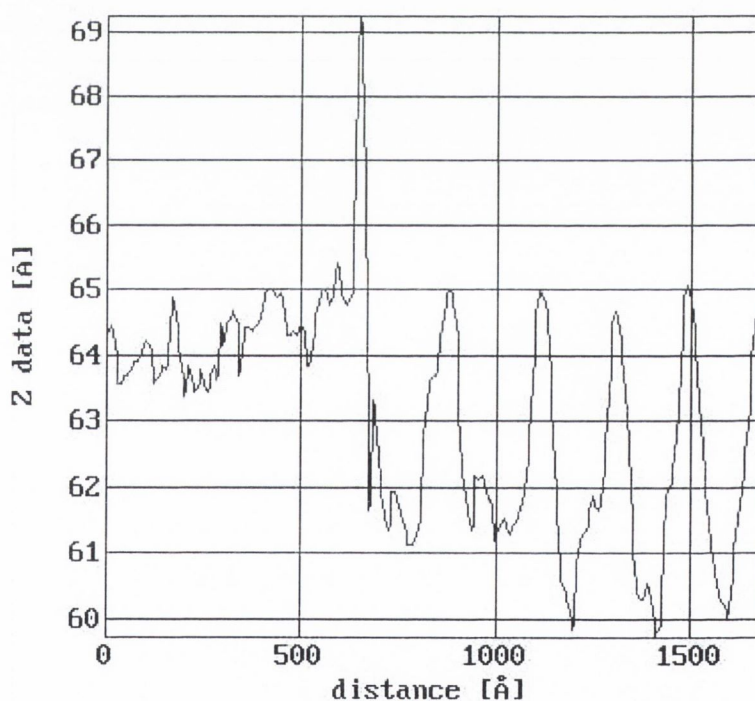
morphology and electronic structure at these regions, and both these will affect the tunneling current, resulting in the enhancement observed.

This polymer does have a tendency to aggregate and to form crystalline regions[4], and it is likely that this is what is observed here, possibly in some way templated by the HOPG lattice structure. This is suggested by the observation in Figure 7.1 that the periodicity of the film is slightly interrupted by one of the underlying flaws in the HOPG (visible as the light lines going diagonally across the image), and is broken completely at the HOPG step to the left of the image.

Figure 7.2 shows a clearer view of the lattice structure, where the disruption in periodicity, possibly induced by a flaw in the underlying HOPG substrate, can be clearly seen in the upper right. The hexagonal lattice structure of the film is striking, with, in most areas, the structure shows remarkable periodicity, although this lessens towards the edges of the film. Also notable is the enhanced brightness of three vertices of the hexagons, corroborating the suggestion that these correspond to a polymer feature of enhanced tunneling.

This enhancement can be seen more clearly in Figure 7.4, which shows a region to the upper left of the film. Parameters used here were a tunneling current of 70 pico amps and a bias voltage of –300 mV. The brighter vertices are well defined and relatively localised, whereas the other vertices are delocalised over a much larger area, and are much less well defined. This further refutes the possibility of this being a HOPG artefact. Also important to note is on examination of the film edge, the ordered film terminates abruptly only at these vertices, and these terminating vertices are much brighter. There are a few possible reasons for this. It could be that these further enhanced features are due to the endgroups of the polymer. PmPV chains are

terminated either by a phosphonate group, or by an aldehyde group. These are both

electron poor, which could give an increased density of states, and therefore increased

tunneling, at these points. Alternatively, it could be that these enhanced edge features

do not differ from those seen throughout the film, but that the difference in interchain

interactions at the locations affects the electronic structure of the terminating

monomer.

Figure 7.4 An edge dislocation in the PmPV film.

Of further interest in Figure 7.4, and offering further evidence that this is indeed a

PmPV film is the feature denoted by an arrow. This is an edge dislocation, an

imperfection in a crystal lattice caused by the premature termination of a row in the

lattice structure. Although due to imaging conditions it cannot be seen in this image,

examination of Figure 7.2 suggests that a flaw in the underlying HOPG induces this

dislocation. To clarify the observation of this defect, a schematic is provided in

Figure 7.5. Note that one row of the lattice terminates abruptly, resulting in the two

adjacent rows continuing the lattice, but at a more widely spaced interval. The end of

the row appears similarly bright as the film edge, supporting the hypothesis that these

mark the end of the polymer chain. The continuance of the lattice beyond this point at

a wider spacing also demonstrates that the PmPV chains must lie parallel to these

rows.
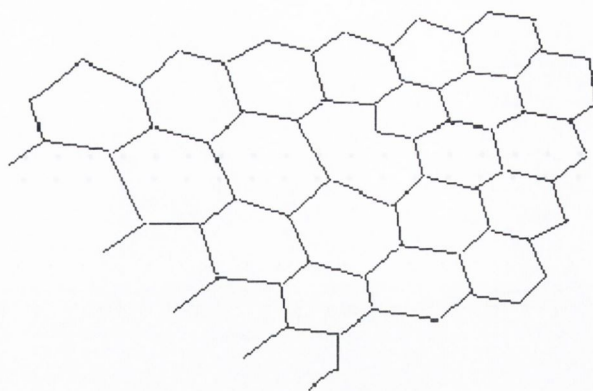
Figure 7.5 Schematic of the edge dislocation.

This is reasonable, as many polymers[5], including PPV[6,7], are known to form aligned films on oriented substrates. This has been characterised by X-Ray diffraction on various substrates such as PTFE, MoS_2, and HOPG. Previous observations however, have relied on Langmuir-Blodgett techniques, and *in situ* polymerisation. This order has not been observed previously for films formed from polymer solutions. From the above observation of the edge defect, the orientation of the PmPV strands is known as being parallel to each other, and aligned from the top right to lower left of the image. From this, and the change in the vertical spacing of the rows, it is clear that there are no chemical bonds connecting vertical rows of the lattice. Note that although there is a significant change in the vertical spacing of the rows, the dimensions of the zigzag line are unchanged, further suggesting that this is due to chemical bonds. Although it is only a tentative suggestion, it is possible that this oriented film is mapping onto the graphitic lattice of the substrate, similarly to how it maps onto carbon nanotubes, as observed previously in Chapter 5, and later in this chapter in section 7.3. The orientation of the HOPG lattice cannot be determined, so this cannot be determined.

Figure 7.6 shows the scanning tunneling spectroscopy of the PmPV film, with a HOPG reference. The HOPG LDOS can be seen as a smooth parabolic shape as is

expected. The PmPV can be seen to follow this shape approximately, but with slight features at 0.8eV, 1.1eV. The bandgap edge of PmPV is approximately 2.7eV, and the edge of this can be seen on the positive side. What is observed here is substantially similar to HOPG, with polymeric states within the bandgap modifying it somewhat. These states are polaronic in nature, and have been observed elsewhere[8].
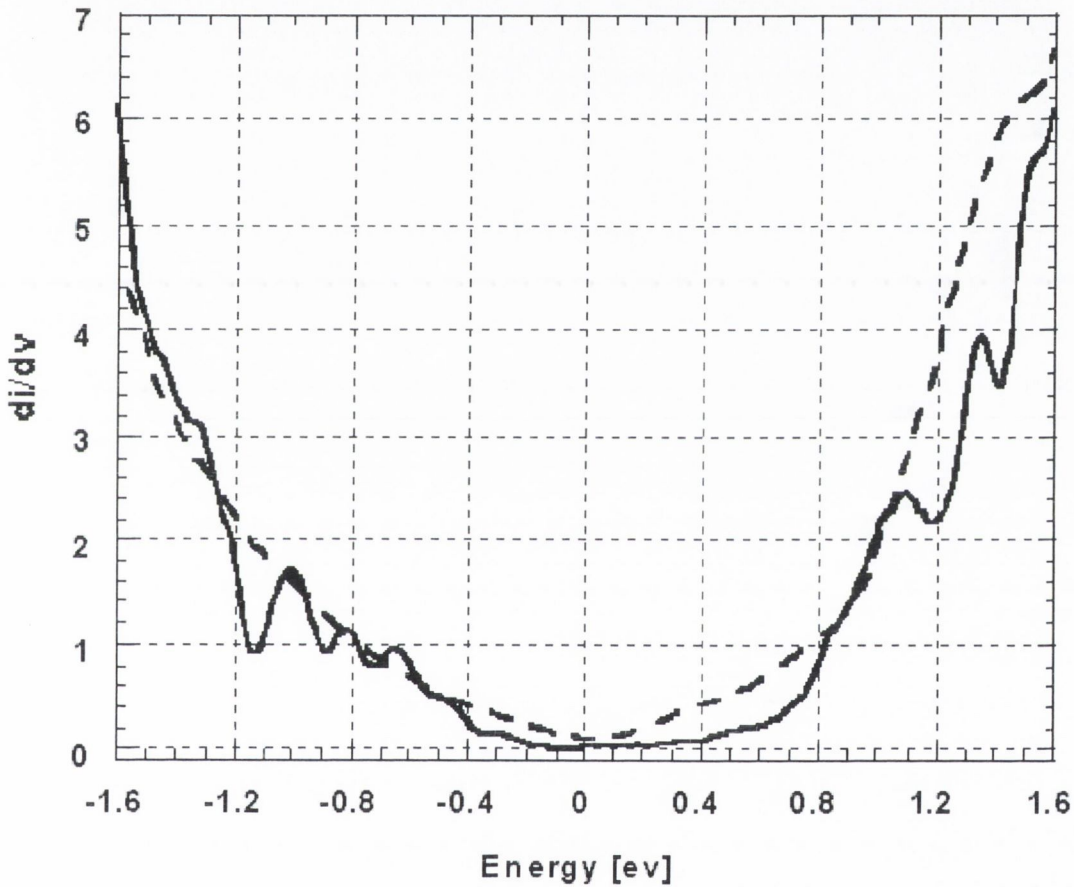
Figure 7.6 STS of PmPV film, with HOPG reference.
PmPV-solid line, HOPG –dashed line.

7.3 STM of PmPV composites

To study SWNT composites, samples were prepared similarly to those of pure PmPV samples, by dropcasting a small amount of dilute composite solution onto a freshly

cleaved HOPG substrate. This was allowed to dry in air, before being introduced into the vacuum chamber of the STM. These samples were then examined.

Due to the low amount of sample on the substrates, finding SWNT can sometimes be a lengthy process, with large areas of the substrate having to be examined to locate them. The much larger number of HOPG steps and fibres further compounds this, as HOPG fibres do appear similar to nanotubes[1,2]. These have been observed, and originally mistaken for SWNT, but are not presented here. STS is used to conclusively distinguish between these, as the electronic structure of SWNT and HOPG artefacts are drastically different.
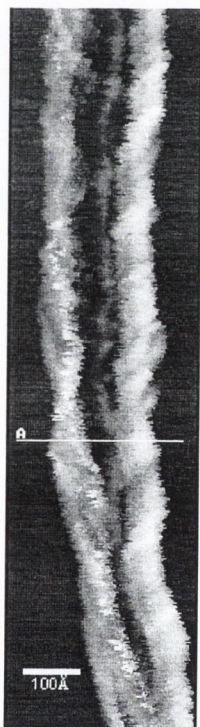
Figure 7.7 Image of two PmPV coated SWNT lying on HOPG.
Nanotube on left-SWNT #1, nanotube on right – SWNT #2.
Line shows the location of cross-section in Figure 7.8

Figure 7.7 shows the bodies of two PmPV-coated SWNTs lying on the HOPG substrate. For convenience, the SWNT on the left and right will be referred to as SWNT #1, and SWNT #2 respectively. SWNT #1 is observed to have a pronounced

helicity towards the lower part of the image. SWNT#2 does not have this helicity although there is a noticeable order in the PmPV coating, apparent as a constant angle between this coating and the nanotube axis throughout the length. Note the similarity between this oriented wrapping and that observed by TEM (Figure 5.14 on page 121).
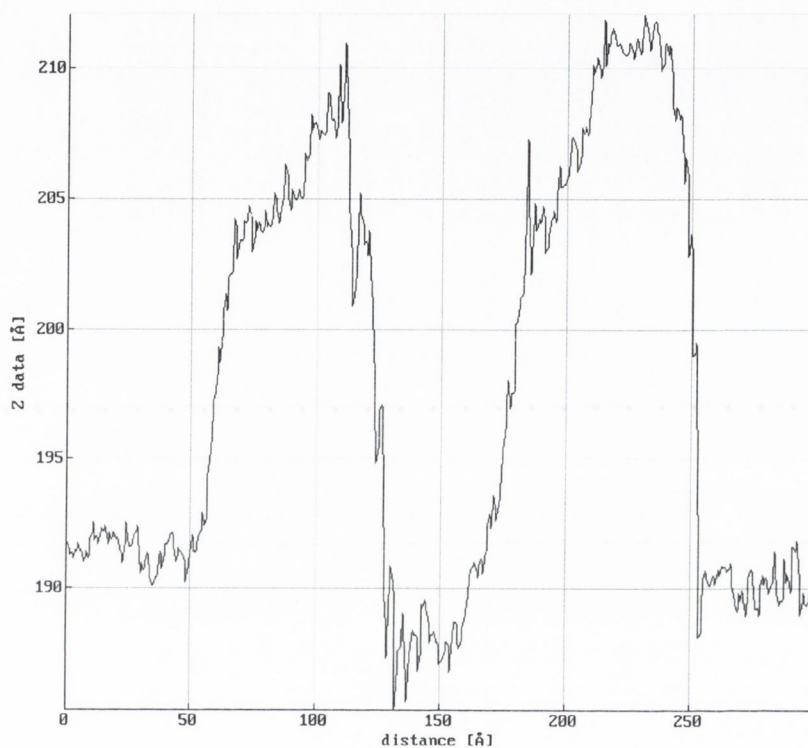
Figure 7.8 Cross-section of Figure 7.7.
Taken at line A in Figure 7.7.

Figure 7.8 shows a cross-section of these nanotubes, taken at the line denoted A in Figure 7.7. SWNT #1 has a height of approx 15Å, although its profile is irregular. SWNT #2 is much more uniform, and is slightly higher, at 20Å. It should be observed that the substrate appears depressed between these nanotubes. This is probably an artefact of the feedback mechanism. A similar oligomer with these sidegroups has been calculated to stack with an interlayer distance of 3.5Å[9]. Computer simulations of PmPV show that it is approximately similar to this, estimated as 0.3-0.4nm[10]. From this, it demonstrates that these measured heights agree with expectations of a SWNT coated with 1-2 layers of PmPV. Note that, as

will been seen, the surrounding substrate is also coated with PmPV. There is, therefore, some uncertainty in these heights, as they are measured relative to this film. Both the thickness of the film, and how the nanotubes sit in relation to this, cannot be determined, and so this introduces uncertainty into the topography. However, given the measured dimensions, this uncertainty is unlikely to be that significant.
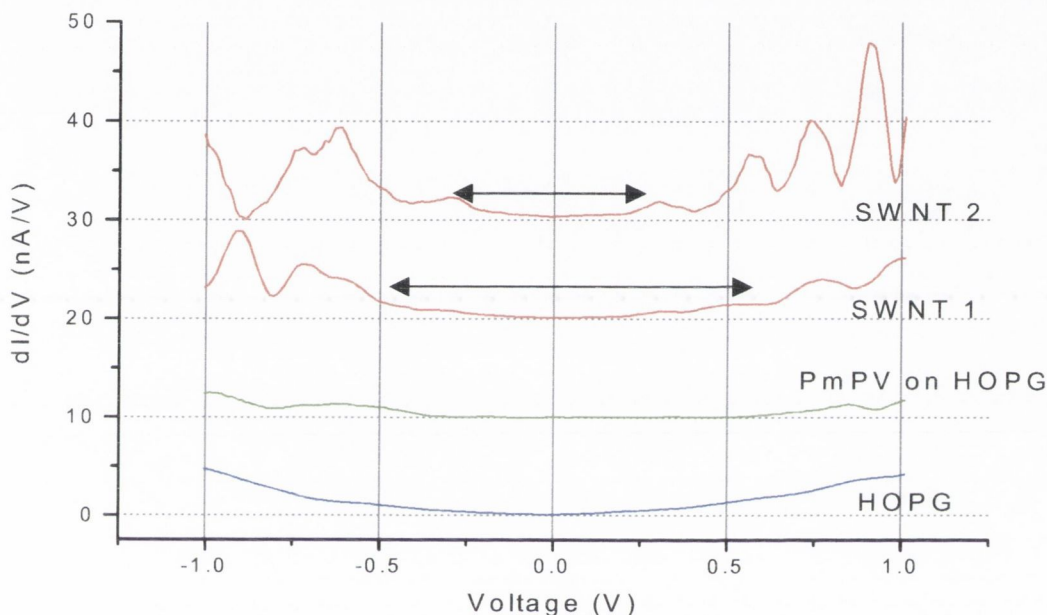
Figure 7.9 LDOS of these nanotubes, with a HOPG and PmPV reference.
Note that curves are offset for clarity.

Figure 7.9 shows the low energy local density of states (LDOS) of these two nanotube structures in the -1.0eV to 1.0 eV energy range, as measured by scanning tunneling spectroscopy. In addition, for comparison, the LDOS of HOPG, and the LDOS of PmPV covered HOPG (taken in the same region as these SWNT, but away from them) are shown. The LDOS of HOPG is a smooth parabola, as expected. As seen previously, the PmPV coated HOPG exhibits a relatively featureless LDOS in this energy range[11], with slight variations due to polaronic states[8]. This is because the

153

band-gap of this polymer is approximately 3.1 eV and electrons tunnel across the polymer region into the HOPG substrate below with little scattering. The LDOS of the wrapped nanotubes, however, are quite different showing sharp, regularly spaced features. These features appear to be the van Hove singularities of the underlying SWNT as reported for clean SWNT by several groups [12,13].

Examining these structures further, it can be seen that SWNT #2 has a bandgap of 0.6eV. The diameter can also be assumed to be less than 2nm. The angle of wrapping has been measured over the length of the body, and is constant at approximately $19\pm2°$. From Equation 2.5, the measured bandgap in eV can be easily related to the diameter of the nanotube in nanometres as follows:

d= 0.7668/$E_{bandgap}$ *Equation 7.1*

This gives a much more accurate measurement of diameter than topographic measurements. Note that the bandgap in this case refers to the distance between the first van Hove singularities, and does not necessarily indicate that the nanotube is semiconducting. Its measured gap of 0.6eV implies a diameter of 1.28nm, demonstrating that the PmPV coating is no more than one or two layers.

Given the order in the coating, and the relatively thin nature of the coating, this SWNT is coated with no more than 1-2 layers of PmPV. Furthermore, for such a thinly coated SWNT, which shows such regularity in wrapping, it is reasonable to expect that the wrapping would be reflective of the underlying SWNT symmetries, and so the angle of wrapping ($19°$) should correspond to the SWNT's chiral angle. This hypothesis is strengthened by the observation by TEM (Figure 5.14) of a similar coating, but at a much different angle of $7°$, demonstrating that this orientation does

vary due to the underlying nanotube. Thus, it is not just phenomenon of PmPV structure, but must be templated by the underlying lattice structure of the nanotube.

From this information on chiral angle and the measured bandgap, it is possible to deduce which chiral vectors ((n, m) values) could account for the SWNT within this wrapping. The (n, m) combinations, which define the chiral vector, directly relate to the diameter and chiral angle by the following equations:

$$d = 0.0783 \, (m^2 + mn + n^2)^{1/2}$$
<div align="right">*Equation 7.2*</div>

$$Tan\theta = \sqrt{3} \, m/(2n + m)$$
<div align="right">*Equation 7.3*</div>

Examining all possible (n, m) values, and allowing a degree of tolerance in these measured values, two types of SWNT could plausibly account for these measurements. One is a (13,6) nanotube (d=1.31nm, $E_{bandgap}$=0.58eV, θ=18.0°); the other is a (12,7) nanotube (d=1.30nm, $E_{bandgap}$=0.59eV, θ=21.4°). The (13,6) SWNT is in slightly better agreement with the measurements compared to the (12,7) SWNT.

From these observations, it can be said that the chiral angle of the underlying SWNT determines the wrapping of the polymer. It should be emphasised that this has been observed independently by STM and TEM. Sample preparation for both these techniques are similar, with solution being dropped onto substrate or grid, and allowed to dry slowly in air. It is probable that this slow evaporation of solvent, and consequent slow precipitation of PmPV from solution, is necessary for this ordered structure to form. The large range of diameter observed in these structures (40-100nm for TEM, 2nm for STM) demonstrates that the ordered binding of PmPV to SWNT is propagated through subsequently deposited layers, and reflected in these layers.

While a similar effect has been observed in the self-ordering of proteins onto carbon nanotubes[14], these are the first observations of a similar effect in non-biological organic systems.

By the same method, the bandgap of SWNT #1 is measured as 1.4eV, yielding a diameter of 0.55nm, which is significantly less than the measured height of this structure. This, and the lack of order in the coating implies that SWNT 1 is not a single coated SWNT but a rope of a few smaller diameter SWNT coated with PmPV. Again, this agrees with previous TEM observations, and can also be noted upon close inspection of Figure 7.7. There is a strong helicity in this structure, which appears to be two, or possibly more, intertwined SWNT. This is confirmed by observing the lower part of the figure, where the rope breaks into two parts, and substrate can be observed between these.

In addition, by inspecting the tips, shown in Figure 7.10, it can be seen that one SWNT ends before the other (denoted by an arrow). The last 30nm of the bundle is much narrower, and displays none of the helicity noticeable along the rest of the rope. This demonstrates conclusively that SWNT #1 is a rope of several SWNT, and therefore that individual SWNT only have this order in the coating. Also, note that the LDOS of this nanotube is much less well defined, with the van Hove singularities being weaker and broader than in SWNT #2. This can be explained by the fact that the tunneling current has less electrical contact to the substrate, having to pass through two or possibly more SWNT. This will lessen the tunneling current, and possibly affect it in other ways, depending on the local intertubule interaction, and the electronic structure of the other nanotube.

Figure 7.10 Image of the two SWNT tips.
Arrow marks the tip of one SWNT in the rope.

7.4 Conclusions

Scanning Tunneling Microscopy has been employed to examine samples of pure PmPV, and SWNT/PmPV Composites. STM of the pure PmPV yields the surprising result that the PmPV can organise into structured films as it precipitates from solution. The possibility that this is an artefact of the HOPG substrate has to be considered, but can be discounted for a number of reasons. These include the observation of edge defects in the crystalline lattice, and scanning tunneling spectroscopy. Literature[6,7] and experimental results reveals that similar effects have been seen in similar polymers, but not arising spontaneously as this does, and has never previously been microscopically observed.

157

Topographic examination shows that there is a small modulation of amplitude 4Å over the surface of the film. This could be due to solely topographic or electronic effects, but is most likely a combination of these two contributions.

The observation of edge defects within this film discounts the possibility of these observations being HOPG artefacts. It also allows the orientation of the PmPV strands to be determined.

Scanning tunneling spectroscopy on these films further proves that these films are polymeric in origin, yielding an LDOS very much as expected; the smooth parabola of HOPG, with slight modifications due to polaronic states of the PmPV.

STM of SWNT composites demonstrate many interesting phenomena. Similar structure to that observed by TEM, are seen. These are cylindrically symmetric ordered structures bound onto an individual SWNT. In this case, the angle with the SWNT axis is measured at 19°, significantly different from the 7° angle observed in TEM. This further proves that this variety of angles must correspond to some underlying property of the SWNT, the chiral angle. The difference in scale is also dramatic. The ordered TEM structure has a diameter ranging from 70-100nm; here it is approximately 2nm. This proves that the coating the SWNT observed here cannot be more than one or two layers deep, whereas in the other example, it must be several hundred layers deep. Therefore, the order in the coating must propagate through subsequently deposited layers, and these subsequent layers are deposited in the same ordered way.

Corresponding with TEM observations, SWNT with unordered coatings are also observed. The example observed by STM can be seen to have a helical structure, suggesting that this is a coated SWNT rope of no more than 2-3 SWNT. Examination of the tip of this rope confirms this, as one SWNT can be seen clearly to terminate before the other. Unfortunately, the resolution of the region after this is too low to determine structure.

Scanning tunneling spectroscopy is used to examine these further. For both structures, the LDOS show the sharp van Hove singularities characteristic of nanotubes. The gap between these singularities is purely diameter dependent, and this is used to calculate the diameters of the two structures. For the individual SWNT, the diameter is 1.28nm., consistent with the theory that this is an individual SWNT coated with no more than 1-2 layers of PmPV. For the rope, the diameter is 0.55nm., agreeing with the observations that this is a rope of only a few SWNT.

Using the information on diameter from STS, and the measured angle of the wrapping, the chiral vector of the individual SWNT is determined, with some margin or error, as there are one or two SWNT that can plausibly account for these measured values of bandgap, chiral angle, and diameter.

For the case of the SWNT rope, the LDOS is less well defined. This can be ascribed to the more complicated electronic structure of a SWNT rope, and the poorer electrical contact to the substrate because of the multiple SWNT.

It is also hypothesised that the ordered binding observed for SWNT is similar to that ordered mapping observed for HOPG, as they are similar, in that they are both

examples of PmPV forming an ordered coating on a graphene sheet. However, this cannot be definitively determined.

References

[1] C.R. Clemmer, T.P. Beebe, *Science,* **251**, 640 (1991).

[2] H. Chiang, A.J. Bard, *Langmuir*, **7**, 1143 (1991).

[3] J. Osing, I.V. Shvets, *Surf. Sci.,* **417**, 145 (1998).

[4] R. Resel, B. Tertinek, S. Tasch, A.P. Davey, W. Blau, H. Horhold, H. Rost, G. Leising, *Synth. Met.*, **101**, 96 (1999).

[5] J.C. Wittmann, P. Smith, *Nature,* **352**, 414 (1991).

[6] K. Pichler, R.H. Friend, P.L. Burn, A.B. Holmes, *Synth. Met.,***55**, 454 (1993).

[7] A. Rajagopul, M. Keil, H. Sotobayashi, A.M. Bradshaw, M.-A. Kakimoto, Y. Imai, *Langmuir*, **13**, 5914 (1997).

[8] P.A. Lane, X. Wei, Z.V. Vardeny, *Phys. Rev. Lett.,* **77**, 1544 (1996).

[9] P.F. van Hutten, H.J. Brouwer, V.V. Krasnikov, L. Ouali, U. Stalmach, G Hadziioannou, *Synth. Met.*, **102**, 1443 (1999).

[10] M. in het Panhuis, R.W. Munn, W.J. Blau, *Proceedings of the International Conference on the Science and Technology of Synthetic Metals*, Austria, 2000, to be published in *Synthetic Metals.*

[11] B. McCarthy, R. Czerw, A. Strevens, A. P. Davey, D. L. Carroll, W. J. Blau, *MRS Proceedings*, Boston, Fall 1999.

[12] J.W.G. Wildöer, L.C. Venema, A.G. Rinzler, R.E. Smalley, C. Dekker, *Nature* **391**, 59 (1998).

[13] T.W. Odom, J. Huang, P. Kim, C.M. Lieber, *Nature* **391**, 62 (1998).

[14] F. Balavoine, P. Schultz, C. Richard, V. Mallouh, T.W. Ebbesen, C. Mioskowski, *Angew. Chem. Int. Ed.* **38,** 1919 (2000).

Chapter 8

Conclusions

8.1 Summary

Composites of PmPV and carbon nanotubes have been developed which demonstrate many interesting properties. Sufficient interaction between the two components is achieved to keep the nanotubes in solution, which is not observed in composites developed elsewhere. Research within the group has shown has this can be used to purify and quantify nanotube powder. Potential applications that are currently being examined include light emitting diodes and field effect transistors.

Transmission Electron Microscopy on these samples yields several interesting results. Agreeing with other research within the group, it can be seen that there is a drastic reduction in the quantities of graphitic impurities in composites based on MWNTs produced by the arc discharge method. The local structure of other nanotubes used, both MWNT produced by catalytic decomposition of acetylene and single walled nanotubes, is relatively unchanged. This is because these raw nanotubes tend to form large interconnected networks, which are not broken up by composite formation.

PmPV is observed to form dendritic growths from specific sites on the nanotubes, noticeably at the nanotube's tips, and along the body in the case of CDA MWNT. Examination of these sites determines that these are nucleated from defect sites in the nanotube lattice. These growths coincide with kinks along the body of CDA MWNT and regions of sharp curvature in the tips of ADM MWNT. They are also numerous growths from the tips and ends of CDA MWNT. These are all places in the nanotube where it can be determined that defects arise.

In certain singular cases, where the nanotubes are open at one end, the PmPV can be seen to fill the nanotube by capillary action. Similar effects to this have been observed previously for metals, and other materials, but never for organic materials. This gives further indication of the strong interaction between the PmPV and nanotubes.

Order is also observed in the coating of several of the MWNT tubes, noticeable as a periodicity in the coating. This gives the first suggestion that there is some mapping between the PmPV and nanotube lattice, which is further explored in the case of SWNT composites by microscopy.

Examples of wrapped individual SWNT are found, but are uncommon. This is because, as stated above, the bulk of the SWNT ropes are unaffected by composite formation. The examples that are found show remarkable cylindrical symmetry. Of further interest is that the symmetry of the coating does not coincide with the cylindrical axis of the nanotube, but rather is inclined at an angle of 7° to the nanotube axis.

Also of note is the thickness of this ordered coating, ranging from 70-100nm. This shows that the initial ordering as the PmPV binds to the SWNT propagates through subsequently deposited layers. Furthermore, on closer examination, those fibres that do not show substantial ordering are revealed to be ropes of SWNT. The intertubule spacing within these ropes are found to be unchanged from those reported elsewhere for pure SWNT samples, proving that no PmPV intercalates between the ropes, and that the SWNT samples are unchanged by composite formation.

Optical spectroscopic characterisation agrees with the microscopic observations. Electron delocalisation along the backbone is substantially reduced, consistent with the curvature imposed on the PmPV strands as they are bound onto the cylindrical nanotube. The luminescence and absorption spectra also do not exhibit the effects of aggregation and interchain interaction that an identical concentration of PmPV does. Rather, the optical spectrum of the composite has similarities with a PmPV solution of much lower concentration. They both have blueshifts in the features that are most sensitive to aggregation and interchain effects. It is suggested that these are substantially reduced by the introduction of SWNT, and the resultant changes in conformation. Features in both the optical and vibrational spectra also have much higher resolution upon introduction of SWNT. This is again similar to extremely dilute solutions. It suggests that this reduction in broadening is due to a reduction in possible PmPV conformations, due to the way it arranges itself on the nanotube lattice.

Scanning tunneling microscopy is employed to examine both the pure PmPV, and SWNT/PmPV composites. PmPV can be seen to form remarkably ordered films on the graphitic lattice of the HOPG substrate. This has been suggested elsewhere by X-

Ray diffraction studies of PPV on oriented substrates, but has not been observed by microscopy. These examples also differ significantly, as these ordered films arise spontaneously as the PmPV precipitates from solution. Previous observations have examined films formed by either mechanical alignment, or *in situ* polymerisation. It seems likely, although unsubstantiated, that this ordered mapping onto a HOPG lattice is a similar mechanism to the ordered mapping onto the nanotube lattice observed in this study.

STM of SWNT composites yields further insights and offers corroboration to TEM observations. Examples of SWNT both with and without ordered coatings are observed. For the case of the order coating, the angle between the symmetry of the coating and the nanotube axis is 19°, as compared to the example observed by TEM, where it is 7°. This gives further credence to the suggestion that it is the lattice structure of the nanotube that gives order to the coating, and not just some inherent order of the PmPV coating. By examining the local density of states and topography of these SWNT, much can be determined. The heights, as measured topographically, are 15Å for the unordered example, 20Å for the ordered. The distance between the van Hove singularities can be measured accurately by scanning tunneling spectroscopy. From these, the nanotube diameters can be determined. Comparing this to the topographically measured heights of the fibres, it can be seen that for the ordered example, it is a SWNT coated with no more than 1-2 layers of PmPV. For the unordered example, it is found to be a rope of SWNT, further confirmed by close examination of the STM images. Given the diameter, and the chiral angle deduced from the wrapping, this is then extended to determine within a small margin of error the chiral vector of this nanotube.

8.2 Conclusions

Results presented in this study show that it is possible to assemble individual polymer strands onto single walled carbon nanotubes using mechanical agitation. This can be used to solubilise and process carbon nanotubes. Furthermore, it has been demonstrated that for individual SWNT, the polymer wraps in an ordered manner, mapping onto the chiral hexagonal lattice of a SWNT and constitutes the first visual confirmation of such assembly. However, for ropes of SWNT, which will not have a symmetric, periodic surface for the polymer to bind to, there is no such mapping. This demonstrates an ordered, predictable interaction between individual SWNT and the polymer. Further, we suggest that such interaction results in the alteration of the polymer's electronic and physical structure, as evidenced in the modified optical and vibrational spectra of the bound polymer. This represents a previously unconsidered route for nanotube applications in molecular scale electronics; for example, the design of specific polymer architectures, hence selecting desired chiral angles and the associated electronic properties.

Appendix

Publication List

Observation Of Site Selective Binding In A Polymer Nanotube Composite

B. Mc Carthy, J.N. Coleman, S.A. Curran, A.B. Dalton, A.P. Davey, Z. Konya, A. Fonseca, J. B.Nagy, W.J. Blau

Journal of Material Science Letters, accepted.

Chiral Mapping of a Conjugated Polymer onto Single Walled Carbon Nanotubes

Brendan Mc Carthy, Jonathan N. Coleman, Richard Czerw, Alan B. Dalton, Marc in het Panhuis, Hugh J. Byrne, David L. Carroll, and Werner J. Blau

Submitted to Physical Review Letters

Microscopic Study of Nanotube Conjugated Polymer Interactions

B McCarthy, JN Coleman, R Czerw, AB Dalton, DL Carroll, and WJ Blau.

Proceedings of the International Conference on the Science and Technology of Synthetic Metals, Austria, 2000, to be published in Synthetic Metals.

Substrate Mediated Ordering In PmPV Thin Films

B. McCarthy, R. Czerw, A. Strevens, A. P. Davey, D. L. Carroll, and W. J. Blau

Proceedings of the Materials Research Society, Boston, Autumn 1999.

Spectroscopic Investigation of Conjugated Polymer/Single Walled Carbon Nanotube Interactions

B. Mc Carthy, A.B. Dalton, J.N. Coleman, H.J. Byrne, W.J. Blau

to be submitted to Chemical Physics Letters

Controlling The Optical Properties Of A Conjugated Co-Polymer Through Variation Of Backbone Isomerism And The Introduction Of Carbon Nanotubes

A.B. Dalton, J.N. Coleman, M. in het Panhuis, B. McCarthy, A. Drury, W.J. Blau, B. Paci, J. -M. Nunzi, H.J. Byrne

Journal of Photochemistry and Photophysics, accepted.

Selective Interaction of a Semi-Conjugated Organic Polymer with Single Wall Nanotubes

A.B. Dalton, C. Stephan, J.N Coleman, B. McCarthy, P.M. Ajayan, S. Lefrant, P. Bernier, W.J. Blau, H.J. Byrne

J. Chem. Phys. B, 104, 10012 (2000).

Phase Separation of Carbon Nanotubes and Turbostratic Graphite using a Functional Organic Polymer

J. N. Coleman, A. B. Dalton, S. Curran, A. Rubio, A. P. Davey, A. Drury, B.Mc Carthy, B. Lahr, S. Roth, R. C. Barklie, W. J. Blau

Advanced Materials 12, 3 (2000) 213-217

Physical Doping of a Conjugated Polymer with Carbon Nanotubes

J. N. Coleman, S. Curran, A. B. Dalton, A. P. Davey, B. Mc Carthy,
W. Blau, R. C. Barklie

Optical Absorption and Fluorescence of a Multi-walled Nanotube-Polymer Composite

A.B. Dalton, H.J Byrne, J.N. Coleman, S Curran, A.P Davey, B. McCarthy, W. Blau

Evolution and Evaluation of the Polymer Nanotube Composite

S. Curran, A.P. Davey, J.N. Coleman, A.B. Dalton, B. McCarthy, S. Maier, A. Drury,
D. Gray, M. Brennan, K. Ryder, M.L. de la Chapelle, C. Journet, P. Bernier,
H.J. Byrne, D.L. Carroll, P.M. Ajayan, S. Lefrant, W.J. Blau

A Composite from Poly(m-phenylenevinylene-co-2,5 dioctoxy-p-phenylenevinylene)
and Carbon Nanotubes: A Novel Material for Molecular Optoelectronics.

S.A. Curran, P.M. Ajayan, W.J. Blau, D.L. Carroll, J.N. Coleman, A.B. Dalton,
A.P. Davey, A. Drury, B. McCarthy, S. Maier, A. Strevens

Percolation Dominated Conductivity in a Conjugated Polymer-Carbon Nanotube
Composite

J. N. Coleman, S. Curran, A. B. Dalton, A. P. Davey, B. Mc Carthy, W. Blau,
R. C. Barklie